Mixtures of colloidal rods and spheres in bulk and in confinement

Dissertation
zur Erlangung des Grades
"Doktor
der Naturwissenschaften"
am Fachbereich Physik
der Johannes Gutenberg-Universität
in Mainz

Swetlana Jungblut
geb. in Karaganda

Mainz, den 5. Mai 2008

Tag der mündlichen Prüfung: 9. Juli 2008

Parts of this thesis have already been published in

- Schilling, T., Jungblut, S., and Miller, M. (2007).
  Depletion-induced percolation in networks of nanorods.
  Phys. Rev. Lett., **98**, 108303.

- Jungblut, S., Tuinier, R., Binder, K., and Schilling, T. (2007).
  Depletion induced isotropic-isotropic phase separation in suspensions of rod-like colloids.
  J. Chem. Phys., **127**, 244909.

- Jungblut, S., Binder, K., and Schilling, T. (2008).
  Isotropic-isotropic phase separation in mixtures of rods and spheres: Some aspects of Monte Carlo simulation in the grand canonical ensemble.
  Computer Physics Communications, doi:10.1016/j.cpc.2008.01.003, in press (CCP2007 proceedings).

- Jungblut, S., Binder, K., and Schilling, T. (2008).
  Suspensions of rod-like colloids and a depleting agent under confinement.
  J. Phys.: Condens. Matter, accepted (CODEF II proceedings).

Zusammenfassung

Wenn man nicht adsorbierende Polymere zu einer Suspension von harten Kolloiden beimischt, entsteht eine effektive Anziehungskraft zwischen den Teilchen, die "Depletion-Wechselwirkung". Monte-Carlo-Simulationen wurden verwendet um ein Phasendiagramm der anisotropen Kolloide, bei denen die Depletion-Wechselwirkung von der Orientierung der Teilchen abhängt, zu untersuchen. Die kolloidalen Stäbchen waren als harte Sphärozylinder modelliert, während die Polymere als Kugeln des gleichen Durchmessers wie die Sphärozylinder angenommen wurden. Stäbchen und Kugeln dürfen einander nicht durchdringen, Überschneidungen zwischen Kugeln sind erlaubt.

Der Schwerpunkt dieser Arbeit sind die Einflüsse der Depletion-Wechselwirkung auf die ungeordnete Phase von anisotropen Kolloiden. Obwohl die meisten Untersuchungen zu diesem System im Bereich des isotrop-nematischen Übergangs liegen, ist die rein isotrope Phase nicht weniger interessant.

Zuerst wurde das Perkolationproblem einer Mischung bestehend aus harten Stäbchen und idealen Kugeln untersucht. Dabei wurde die Menge der Kugeln begrenzt, so dass keine Entmischung stattfinden konnte. In den früheren Experimenten wurde das Herabsenken der Perkolationsschwelle beobachtet. Unsere Simulationen bestätigen, dass dieser Effekt auf die Depletion-Weckselwirkung zurückzuführen ist. Die lokalen strukturellen Änderungen, die in den Simulationen gemessen wurden, deuten an, dass die Depletion-Kräfte lokale Anordnung und Clustering der harten Stäbchen bewirken.

Danach haben wir das Phasendiagramm des Entmischungsübergangs für kurze Stäbchen in großkanonischen Simulationen unter Verwendung der "Successive-Umbrella-Sampling"-Methode bestimmt. "Finite-Size-Scaling"-Analyse wurde verwendet, um die Position des kritischen Punktes zu bestimmen. Die Grenzflächenspannung, sowie ihr Verhalten in der Nähe des kritischen Punktes wurden analysiert. Das Phasendiagramm aus den Simulationen wurde mit den Vorhersagen der "Free-Volume"-Theorie verglichen.

Zum Schluss haben wir noch die Eigenschaften einer Suspension, die zwischen harten Wänden eingeschlossen sind, untersucht. Der kritische Punkt der Gas-Flüssigkeit-Entmischung verschiebt sich zu höheren Konzentrationen von Stäbchen und geringeren Konzentrationen von Kugeln, da geordnete Oberflächenphasen an den Wänden gebildet werden. Wenn der Abstand zwischen den Wänden klein genug wird, verschiebt sich der kritische Punkt zurück in Richtung des freien $2d$ Systems, da dann die Entmischung in den Oberflächenschichten stattfindet. Eine Methode zur Berechnung des Kontaktwinkels der Gas-Flüssigkeit-Grenzfläche mit der Wand ist eingeführt und das Benetzungverhalten bei der Annäherung an den kritischen Punkt beschrieben worden.

Abstract

When non-adsorbing polymers are added to an isotropic suspension of rod-like colloids, the colloids effectively attract each other via depletion forces. Monte Carlo simulations were performed to study the phase diagram of such rod-polymer mixtures. The colloidal rods were modelled as hard spherocylinders; the polymers were described as spheres of the same diameter as the rods. The polymers may overlap with no energy cost, while overlap of polymers and rods is forbidden.

In this thesis the emphasis was on the depletion effects caused by the addition of spheres on the isotropic phase of rod-like particles. Although most of the present experimental studies consider systems close to or beyond the isotropic-nematic transition, the isotropic phase with depletion interactions turns out to be a not less interesting topic.

First, the percolation problem was studied in canonical simulations of a system of hard rods and soft spheres, where the amount of depletant was kept low to prevent phase separation of the mixture. The lowering of the percolation threshold seen in experiment is confirmed to be due to the depletion interactions. The local changes in the structure of the fluid of rods, which were measured in the simulations, indicated that the depletion forces enhance local alignment and aggregation of the rods.

Then, the phase diagram of isotropic-isotropic demixing of short spherocylinders was calculated using grand canonical ensemble simulations with successive umbrella sampling. Finite size scaling analysis allowed to estimate the location of the critical point. Also, estimates for the interfacial tension between the coexisting isotropic phases and analyses of its power-law behaviour on approach of the critical point are presented. The obtained phase diagram was compared to the predictions of the free volume theory.

After an analysis of the bulk, the phase behaviour in confinement was studied. The critical point of gas-liquid demixing is shifted to higher concentrations of rods and smaller concentrations of spheres due to the formation of an orientationally ordered surface film. If the separation between the walls becomes very small, the critical point is shifted back to smaller concentrations of rods because the surface film breaks up. A method to calculate the contact angle of the liquid-gas interface with the wall is introduced and the wetting behaviour on the approach to the critical point is analysed.

Contents

List of Figures

Abbreviations

Constants

d	Distance between two walls
k_B	Boltzmann constant
z_r	Fugacity of rods
z_s	Fugacity of spheres
A	Connectedness criterion
D	Diameter of a spherocylinder
L	Length of a spherocylinder
L_x, L_y, L_z	Dimensions of a simulation box
N_r	Number of rods
N_s	Number of spheres
T	Temperature
V	Volume of the simulation box
μ_r	Chemical potential of rods
μ_s	Chemical potential of spheres

Definitions

$\mathbf{u}$	Orientation unity vector of a spherocylinder
n_s	Number of spheres in a cluster move
d_s	Shortest axis-axis distance
$v_r = \frac{\pi D^3(2+3L/D)}{12}$	Volume of a spherocylinder
$v_s = \frac{\pi D^3}{6}$	Volume of a sphere
$\mathbf{Q} = \frac{1}{2N_r}\sum_{i=0}^{N_r}(3\mathbf{u}^i\mathbf{u}^i - \mathbf{I})$	Orientation tensor
E	Energy of a state
F	Free energy
$P(N_r)$	Probability to find N_r rods
S	Nematic order parameter
$V_{\mathrm{dz}} = \frac{\pi(2D)^3(3L/(2D)+2)}{12}$	Volume of depletion zone and spherocylinder
$W(N_r)$	Weight function

$\beta = \frac{1}{k_B T}$	Inverse temperature
$\eta_r = \frac{v_r N_r}{V}$	Rod volume fraction
$\eta_s = \frac{v_s N_s}{V}$	Sphere volume fraction
$\eta_s^R = z_s v_s$	Sphere reservoir volume fraction
ξ	Biaxiality order parameter
Π	Percolation probability
Φ	Percolating fraction
Ω	Grand potential

Chapter 1

Introduction

Colloidal suspensions consist of relatively large particles in a size range from about hundred nanometres up to a few micrometers, which are, as indicated by the term, suspended in solution. The size of the particles allows them to be seen by the usual optical microscopes, unlike the solvent molecules. There is a wide variety of colloidal suspensions, in which solute substance as well as the solvent itself can be varied over a wide range in the phase diagram. If the solution is in a gaseous state, one finds aerosols, like fog, smoke and sprays, in which the colloids are liquid or solid particles. Foams and solid foams, e.g. whipped cream or styrofoam, represent the opposite limit, in which the colloids are gases immersed in liquid or solid solution. Liquid particles in liquid and solid solutions form emulsions and gels, like milk, mayonnaise and butter, while solid particles dispersed in liquids and solids produce paints, ink, pearls and opals. Biological colloids are represented by blood, bones, muscles, cell membranes, etc.

The interactions between the colloidal particles resembles closely those of smaller molecules. Hence, colloidal suspensions are often used as a model system to study phase transitions. In this thesis colloidal rod-like particles are considered as a model of liquid crystals.

Different from the usual liquid-to-crystal transition in suspensions of spherical particles, the shape anisotropy of particles forming liquid crystals causes additional states, like nematic or smectic. On increasing the density or interaction range and strength, the liquid, where the orientations and positions are completely disordered, changes its structure. A suspension of

elongated particles is called nematic when the positions of the centres of mass are disordered but the particle axes are aligned. In the smectic phase the particles also have almost the same orientation and the positions of the particles are partly ordered – they form layers, inside which there is still no ordering. The onset of the positional order inside the slices indicates the formation of a crystal. The phases in which some, but not all parameters are ordered are described as liquid crystals.

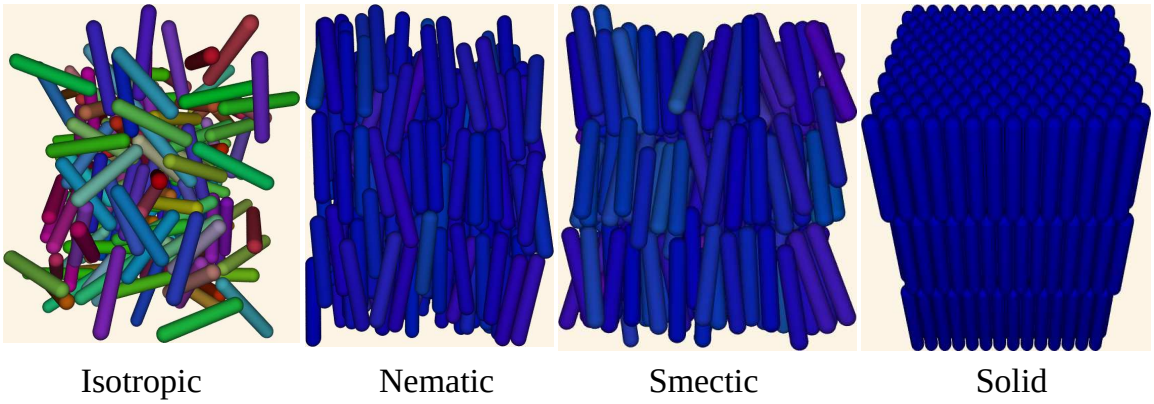

Figure 1.1: Snapshots of liquid crystal phases. The colour of a rod is a function of its orientation.

The first mentioning of an experiment on liquid crystals dates not much more then a century back [Reinitzer (1888); Sonin (1991)]. Nevertheless, now liquid crystal technologies are widely spread because of their use in optical devices. One fascinating point of the phase behaviour of a suspension of anisotropic particles is that it can be of the purely entropic origin. Colloidal suspensions are characterised by their stability, which is guaranteed by electrostatic or steric repulsion between particles [Verwey (1940); Derjaguin (1940)]. Thus, the suspended particles are repulsive. Onsager showed that the phase transition from the isotropic to nematic liquid occurs in such a system and is due to gain in entropy only [Onsager (1949)]. Later, Cotter introduced a model description of a nematic liquid crystal [Cotter (1977); Cotter and Wacker (1978)], which can be used to localise the isotropic-nematic transition for particles of finite length.

Examples of systems consisting of anisotropic particles and showing liquid-crystal behaviour can be found everywhere. There are viruses like tobacco mosaic virus and fd-virus in biology, or carbon nanotubes, which were syn-

thesised recently, and boehmite particles in material science. Their phase behaviour can be explained by means of a simple model of hard rod-like particles like spherocylinders or ellipsoids.

The liquid crystals in partly ordered phases and transitions between them were studied in the last century theoretically [Oseen (1933); Onsager (1949); Frank (1958); de Gennes (1971); Odijk (1986); Vroege and Lekkerkerker (1992)], in experiment [van Iterson, Jr. (1933); Tang and Fraden (1995)] and in simulations [Frenkel (1987); Bolhuis and Frenkel (1997)]. Computer simulations on hard spherocylinders were performed to describe the dependence of the phase behaviour on the length-to-diameter ratio of the rods and on their density [Frenkel (1988); McGrother *et al.* (1996); Bolhuis and Frenkel (1997)]. Analytically, the phase diagram of hard spherocylinders was calculated within density functional theory [Poniewierski and Sluckin (1991)].

And even the behaviour of a completely disordered fluid of anisotropic particles becomes interesting considering the ways it can be influenced by some external forces.

The phase behaviour and other physical properties of the liquid crystals depend on their interactions. Addition of non-interacting polymers to a colloidal suspension changes the effective forces between the colloidal particles.

The Asakura-Oosawa-Vrij model [Oosawa and Asakura (1954); Vrij (1976)] was developed as a useful model for mixtures of polymers and spherical colloids. In this model the polymers are assumed to be freely interpenetrable with respect to each other, while there is a hard-core repulsion between the colloids as well as between the colloids and the polymers. As the interaction energy is then either zero or infinite, the phase behaviour is purely of entropic origin.

It was found that the colloidal particles attract each other via depletion forces, which are indeed entropically induced. Suppose two of such hard particles are in a suspension of non-interacting polymers. These polymers are described as spheres, which may overlap each other, but not the colloids. There is a zone around the colloids, where the centres of masses of spheres

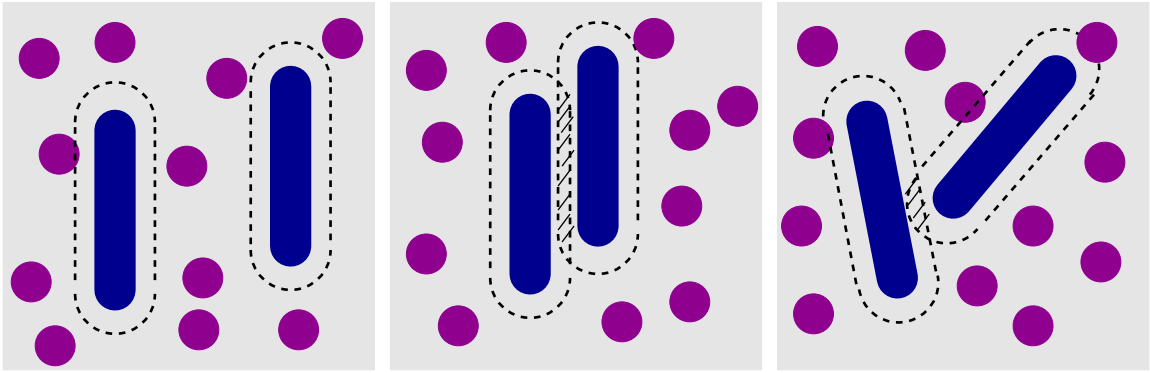

Figure 1.2: Depletion zones.

have no access to, called "depletion zone", which is indicated by broken lines in Figure 1.2. If the particles come close to each other, such that these zones can overlap (shaded areas in the middle and right frames of Figure 1.2), the volume accessible to the spheres becomes larger, thus, increasing their translational entropy. On the other hand, the colloidal particles loose their translational entropy coming close to each other. Hence, the strength of the interactions is determined by the concentration and the size ratio. Assuming the case of colloidal rods, which is considered here, the orientational entropy is also important. The overlap of the depletion zones is the larger the more rods are aligned, but, in the same time, the orientational freedom of one rod becomes limited by the presence of the other one. All in one, the depletion forces in the Asakura-Oosawa-Vrij model stem from an interplay between the translational entropies of colloids and polymers, to which the orientational entropy contributes in case of colloidal rods.

Mixtures of rod-like particles with depletion interactions attracted some interest in the last years. Free volume theory calculations [Lekkerkerker *et al.* (1992); Lekkerkerker and Stroobants (1994)] allowed predictions of the phase behaviour for different rod lengths. In experiment the effect of the addition of depletant on the isotropic-nematic phase transitions in mixtures of the tobacco mosaic viruses [Adams *et al.* (2004); Dogic and Fraden (2001); Dogic *et al.* (2004); Dogic and Fraden (2006)], boehmite rods [Buitenhuis *et al.* (1995)] and carbon nanotubes [Wang *et al.* (2004)] was studied. Also Monte Carlo simulations of rods with depletion interactions, modeled as an effective potential between the rods, were performed

to locate phase boundaries via thermodynamic integration [Bolhuis *et al.* (1997); Savenko and Dijkstra (2006)]. The depletion induced interactions between two spherocylinders were calculated in Monte Carlo simulations [Li and Ma (2005)]. The effect of the depletion on the isotropic phase was studied theoretically within the second virial approximation [Matsuyama and Kato (2001)].

In this thesis, Chapter 5 describes the way the phase diagram develops while varying the interaction between the colloids. The effective force between two colloids depends on the amount of depleting agent, here spheres, in the mixture. The phase boundaries of the isotropic-isotropic demixing were obtained in the grand canonical ensemble with the successive umbrella sampling method [Virnau and Müller (2004)].

Chapter 4 picks an area in the phase diagram where the mixture is completely disordered and describes particularly how the percolation threshold, i.e. the system density at which the sample contains an infinite cluster of connected particles, depends on the strength of the attractive forces between the particles. Also the structure of the fluid of spherocylinders and its variations due to depletion interactions are described in this chapter.

One more factor defines the properties of the system – confinement. The effect of the presence of hard walls on a liquid of rods was studied close to the isotropic-nematic transition theoretically with the Zwanzig model of restricted orientations [van Roij *et al.* (2000a,b)] and with Gibbs ensemble Monte Carlo simulations [Dijkstra *et al.* (2001)]. The isotropic-nematic transition in confinement was found to occur at lower rod densities than in the bulk. Apparently, the walls favour the nematic phase, which density is higher than the density of the isotropic phase. On the other hand, in a very dilute system the rods are driven from the wall. Once more this effect is entropical. On the approach of the wall the rods lose orientational entropy but win translational entropy. Depending on the number of rods, they would either align close to the wall, or try to come away from it. For the dilute isotropic fluid of rods with depletion interactions close to one hard wall, there is a theoretical prediction of depletion-induced adsorption of rods onto the wall [Sear (1998)].

Chapter 6 deals with changes which occur when the isotropic mixture is confined into a slit-pore. In a pure rod system and at concentrations considered here, the rods are driven from the wall because of the loss of orientational entropy on the approach to the wall, but the depletion interactions lead to their adsorption. The interplay of these effect is studied here.

Chapter 2 describes the model used in Monte Carlo simulations of colloid-polymer mixtures, while Chapter 3 sketches the methods applied by performing the simulations.

Chapter 2

Model

In this work the colloidal particles are assumed to be hard spherocylinders, i.e. cylinders of length L and diameter D capped at their ends by semi-spheres of diameter D. The non-interacting polymers are approximated as spheres of the same diameter as the spherocylinders, which are hard with respect to the rods and freely interpenetrable among each other.

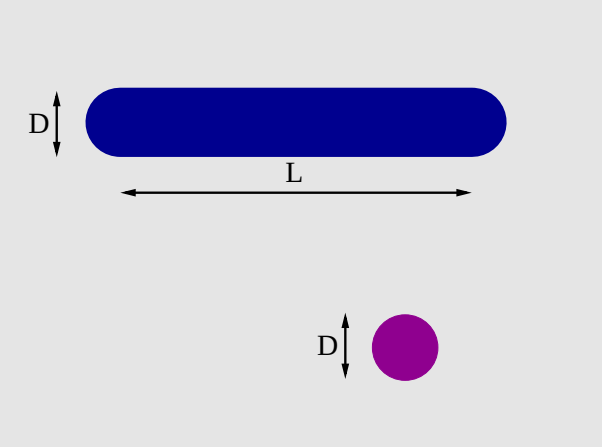

The rod-rod (rr), rod-sphere (rs) and sphere-sphere (ss) interaction potentials are

$$\begin{aligned} U_{rr} &= \begin{cases} \infty, & \text{if particles overlap} \\ 0, & \text{else} \end{cases} \\ U_{rs} &= \begin{cases} \infty, & \text{if particles overlap} \\ 0, & \text{else} \end{cases} \\ U_{ss} &= 0. \end{aligned} \tag{2.1}$$

The overlaps are identified by calculating the smallest distances between two spherocylinder axes in case of the rod-rod interactions, and between the centre of mass of a sphere and, again, the cylinder axis. An overlap occurs if this distance is smaller than the rod diameter or the sum of rod and sphere radii. During a simulation run, the current positional and, for spherocylinders, orientational vectors are stored, which gives the complete information about the state of the system.

The systems considered here are described by a Hamiltonian $\mathcal{H}$, which can be presented as a sum of the kinetic and potential energy of the system. Thus, the partition sum $\mathcal{Z}$ of N particles at positions $\vec{r}_i$ with momenta $\vec{p}_i$, orientations $\vec{\Omega}$ and angular momenta $\vec{w}_i$ at temperature T is given by

$$\mathcal{Z} = \int d\vec{p}^N d\vec{w}^N d\vec{r}^N d\vec{\Omega}^N \exp\left[-\frac{1}{k_B T}\mathcal{H}(\vec{p}^N, \vec{w}^N, \vec{r}^N, \vec{\Omega}^N)\right] \tag{2.2}$$

The partition sum is connected to the free energy F of the system via

$$F = -k_B T \ln \mathcal{Z} \tag{2.3}$$

The integration of the kinetic part of the Hamiltonian yields a multiplicative factor to the partition sum, or an additive constant to the free energy. Since this factor does not diverge by changing the number of particles in the system, the phase transitions, which occur in such a system, are governed by the second part of the Hamiltonian, namely, the potential energy, or the configurational energy, which is described by the current positional and orientational vectors of the simulated particles.

2.1 Simulation box

All particles are confined into a simulation box. The shape and the size of the simulation box are chosen depending on the questions addressed in the simulations. The forces between particles are short-ranged, thus, the natural choice of boundary conditions is the minimal image technique.

Percolation

Cubic simulation box with edges

$$L_z = L_y = L_x = 5L \tag{2.4}$$

in the most cases and minimal image periodic boundary conditions. The size of the simulation box was varied for studying the finite size effects.

Phase coexistence

Simulations were performed in a box with edges

$$L_z \geq L_y = L_x \geq 3L \tag{2.5}$$

and minimal image periodic boundary conditions. In a rectangular box configurations at coexistence form preferably such that the interfaces are parallel to the small faces of the box (see figure 3.5). This simplifies the analysis of the interfacial tension. The finite size effects were examined in a cubic box.

Confinement

In confinement the box dimensions were

$$L_x = L_y \geq 3L \text{ and } L_z = d \tag{2.6}$$

with minimal image periodic boundary conditions in the x- and y-directions and walls at distance d in the z-direction.

The interaction potentials of rods (rw) and spheres (sw) with the walls were defined to be hard

$$\begin{aligned} U_{rw} &= \begin{cases} \infty, & \text{if overlap} \\ 0, & \text{else} \end{cases} \\ U_{sw} &= \begin{cases} \infty, & \text{if overlap} \\ 0, & \text{else} \end{cases} \end{aligned} \tag{2.7}$$

Since the walls are assumed to be in z-direction, the overlap distance between a sphere and a wall is just the z-component of its positional vector – an overlap occurs if it is smaller than the sphere radius. The distance between a wall and a spherocylinder is calculated from the z-coordinates of the ends of the cylinder axis – both of them must be larger than the radius of a rod to prevent an overlap with the wall.

In principle, an additional short range (repulsive or attractive) interaction between walls and rods or spheres can be imagined [De Virgiliis *et al.* (2007)], which experimentally is realisable by suitable coating of the walls. However, such an extension of the model is left to future work.

2.2 Order parameter

Two order parameters are defined in this thesis. The first one, the density of rods, allows to identify gas- and liquid-like phases of spherocylinders. Since both of them are completely disordered, this is the only difference between them. The nematic phase is characterised by the onset of alignment. There is also a density difference between the isotropic and the nematic phase, but this parameter is used to specify differences in the isotropic phase. Thus, another order parameter needs to be defined which describes the alignment of the spherocylinders. It should reflect if there is a preferred direction in the system of rods, or not, which corresponds to the nematic and to the isotropic phase, respectively. The tensor $\mathbf{Q}$ can be defined as

$$\mathbf{Q} = \frac{1}{2N_r} \sum_{i=0}^{N_r} \left(3\mathbf{u}^i\mathbf{u}^i - \mathbf{I}\right), \tag{2.8}$$

where $\mathbf{u}^i$ is a unit vector in the direction of the orientation of the rod i and $\mathbf{I}$ is the identity matrix. N_r is the number of rods for which the order parameter is calculated. Reliable results are obtained for only very large numbers of rods. However, in a simulation, averaging over uncorrelated configurations in a comparably small system gives the same effect as if the number of rods is very large. For very small systems the number of configurations needed to compute an average can soon become very large, like an example in Chapter 6 illustrates.

Eigenvalues of the tensor allow to make a statement about the strength of the alignment of the rods. The nematic order parameter S is the largest **absolute** eigenvalue [Low (2002)]. (Note that many authors use the largest eigenvalue instead of the eigenvalue with the largest absolute value, which leads to different results in the case of uniaxial surface ordering!) S indicates if there is a preferred direction in the system and how strongly the rods are oriented with respect to it. The eigenvector to this eigenvalue is called director. If S is zero, the phase is completely isotropic. If S is unity, all rods are aligned parallel to the director. If S is negative, they lie perpendicular to the director. The biaxiality measure ξ is half of the difference of the other two eigenvalues of the matrix $\mathbf{Q}$. It shows if there is another

preferred direction in the plane perpendicular to the director.

2.2.1 Confinement

Negative values of the order parameter as well as the biaxiality parameter become important in case of a confined fluid, where the walls introduce ordering to the rods.

Next, to study the anchoring effects of the walls, the dependence of the nematic order parameter S and the biaxiality parameter ξ on the distance from the walls need to be defined. To do that $\mathbf{Q}$ is re-defined as

$$\mathbf{Q}(z) = \frac{1}{2\tilde{N}_r} \sum_{i=0}^{\tilde{N}_r} \left(3\mathbf{u}^i\mathbf{u}^i - \mathbf{I}\right). \tag{2.9}$$

The space between the walls is divided into thin slices, so $\tilde{N}_r$ is the number of rods in such a slice at the distance z/D from the middle of the simulation box. In this fashion, the alignment induced by the walls can be studied, since the nematic order parameter and the biaxiality measure depend on the position z with respect to the walls.

Chapter 3

Simulation methods

This work is concerned with the depletion induced interactions between the spherocylinders. The strength of the interactions depends on the amount of spheres present in the system. In the grand canonical representation of the phase diagram of the mixture, the chemical potential plays a role of the inverse temperature. Thus, the demixing transition into gas- and liquid-like phase of spherocylinders, studied in the grand canonical ensemble in this work, happens at rather high chemical potentials of spheres. Since the spheres behave like an ideal gas in the absence of the spherocylinders, in the rod-poor phase the amount of spheres in the system goes exponentially with their chemical potential. The usual grand canonical insertion of a spherocylinder is almost impossible - the acceptance probability of the move is of the order of 10^{-6}. This is due to the overlaps with the spheres which fill the entire simulation box. Fortunately, a solution of the problem was suggested for spherical colloids in the canonical [Biben *et al.* (1996)] and in the grand canonical ensemble [Vink and Horbach (2004)]. Here, this approach is adjusted to the case of spherocylinders. The application of the cluster move allows to modify the acceptance probabilities of insertion/removal moves to be of the order of 10^{-1} in the dense phase which is rich in spheres only. However, in the rod-rich phase the cluster move becomes less successful. Thus, with increasing rod volume fraction the acceptance probabilities eventually reach values of 10^{-6} again.

3.1 Canonical ensemble

In the $NVT-$ensemble the volume V of the system as well as the number of rods N_r and the number of spheres N_s are fixed. The temperature T is formally also fixed, but irrelevant, since in an entropic system it only sets the energy scale. For the sake of generality, the applied methods are described for the general case, where a nontrivial energy scale is present.

Configurational space is explored with translational moves of rods and spheres, rotational moves of spherocylinders and cluster moves, in which one rod is swapped with a cluster of spheres. In a usual translational or rotational move a rod (or sphere) is moved randomly by less than a predefined maximal amount and the energy E_n of new configuration is calculated. With hard particles, of course, the energy is zero, if no overlap occurs, or infinite, if particles overlap, in which case the move is rejected. The maximal displacement and maximal rotation are set at the beginning of a simulation.

Any Monte Carlo move has to fulfil the requirement of balance [Frenkel and Smit (2002)]. In order to simplify the equations, usually even detailed balance is demanded

$$\mathcal{N}(o)\mathcal{G}(o \to n)\mathcal{A}(o \to n) = \mathcal{N}(n)\mathcal{G}(n \to o)\mathcal{A}(n \to o) \tag{3.1}$$

where $\mathcal{N}(o/n)$ is the Boltzmann probability of the old/new state, $\mathcal{G}(o \to n)$ the probability to generate one state from another, and $\mathcal{A}(o \to n)$ the probability to accept the move.

The generation probabilities of the usual translational/rotational moves are equal and cancel on the both sites of the equation 3.1. The same happens in the case of the cluster move, which, in the canonical ensemble, is essentially a combination of grand canonical cluster removal and cluster insertion of a spherocylinder. A detailed description of these moves is given in section 3.2. Expressions for the generation probabilities of moves are also given there, since in the grand canonical simulations they do not cancel, thus, have to be used by calculating the acceptance probability of a grand canonical cluster move.

The Boltzmann probabilities of the old and the new states in the canonical

ensemble are given by

$$\begin{aligned} \mathcal{N}(o) &= Ce^{-\beta E_o} \\ \mathcal{N}(n) &= Ce^{-\beta E_n} \end{aligned} \tag{3.2}$$

with $E_{o/n}$ being the energy of state o/n and C a constant.

The Metropolis probability of accepting a new configuration is also:

$$\mathcal{A}(o \to n) = \min\left[1, e^{-\beta \Delta E}\right] \tag{3.3}$$

with $\Delta E = E_n - E_o$.

In the case of hard interactions the energy calculation consists of a simple check for overlaps, as indicated in equation 2.1. The energy of the starting configuration E_o is zero, since no overlaps are allowed. The energy of the *new* configuration is either zero or infinite. Thus, the probability of accepting the move reduces to one or zero, depending on the presence of overlaps.

3.1.1 Percolation

The percolation problem is defined in terms of connected clusters – if a cluster of connected particles becomes infinite, the system is percolating. However, in a system with hard interactions the probability of finding two particles in touch is vanishingly small. Thus, to detect a connected cluster, a connectedness criterion is defined. Two rods are connected if the distance between them is less then $A = 0.2\ D$. This choice is arbitrary, it affects only the numerical results, but as long as $A < D$, it does not affect the general trends observed. For $A < D$ the percolation threshold stays sensible to the depletion interactions which have the range of the sphere diameter.

The percolation threshold is defined as the rod volume fraction at which the average probability to find a cluster connected to itself via periodic boundaries becomes larger than 50%. This definition is consistent with the definition of an infinite cluster used in this work. A cluster is infinite if a particle, which belongs to a cluster found in a simulation box without boundary conditions, is connected to its own periodic image when the

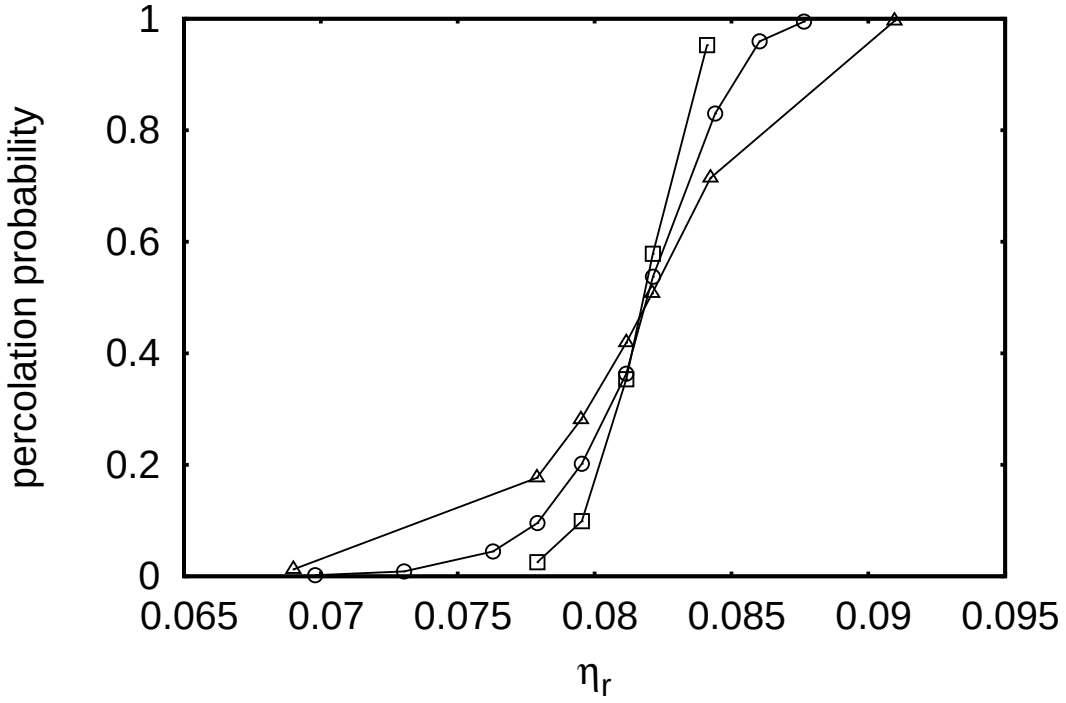

Figure 3.1: Probability to find a percolating cluster as a function of rod volume fraction in a simulation box of edge 70 D (open triangles), 100 D (open circles) and 160 D (open squares). Rod aspect ratio $L/D = 20$. Solid lines are guides to the eyes.

periodic boundary conditions are switched on. This is the way three dimensional percolation was studied in this work. A study of finite size effects is presented in Chapter 4. Here is to be mentioned that in a finite system the probability of finding a percolating cluster is described by a sigmoidal curve, instead of a step function going from zero to one at the percolation threshold. However, the steepness of the curve found in a finite system depends on the system size, unless at the threshold itself. There the probabilities to find a percolating cluster cross in one point, as known generally from percolation theory [Stauffer and Aharony (1994)]. This works also here, as indicated in Figure 3.1, where the percolating probabilities calculated in systems of three different sizes are shown. In the most simulations the percolation probabilities in system of only one size were calculated, the intersection point is assumed to lie at a percolation probability of 0.5. Thus, the percolation threshold is always placed at the rod volume fraction at which the probability equals 0.5.

3.2 Grand canonical ensemble

In the $\mu VT-$ensemble the volume V and the chemical potentials μ_r of the spherocylinders and μ_s of spheres are fixed. The system is equilibrated with insertion/removal moves. These moves have to fulfil (detailed) balance given by equation 3.1. Unlike in the canonical case of translational/rotational moves and of the canonical cluster move, the generating probabilities of insertion/removal moves in the grand canonical ensemble do not cancel and have to be taken into account by calculating the acceptance probabilities.

3.2.1 Insertion moves

The insertion move starts with choosing the random position for the new spherocylinder to be inserted. The probability to select a specific position inside the simulation box is $1/V$. In the following the expressions for the probabilities which correspond to a certain decision are given in square brackets. An orientation is selected from an uniform distribution of the solid angle $[1/(4\pi)]$. At this point the rod would certainly overlap with some spheres, as indicated in Figure 3.2 (left), where the new spherocylinder with its depletion zone is shown by the dashed line. The clue of the cluster move is the removal of these spheres to facilitate the insertion of the spherocylinder, Figure 3.2 (right). Of course, detailed balance must be fulfilled. Thus, in the removal move some spheres need to be inserted into the void, Figure 3.2 (centre), left by the removed spherocylinder. The volume of the void

$$V_{\mathrm{dz}} = \frac{\pi(2D)^3(3L/(2D)+2)}{12} \tag{3.4}$$

is the volume of the spherocylinder and the depletion zone around it. The number of spheres n_s to be inserted is chosen randomly from the interval $[0, m\rangle$, where m is an integer given by

$$m = 1 + \max[1, \mathrm{int}(z_s V_{\mathrm{dz}} + a\sqrt{z_s V_{\mathrm{dz}}})] \tag{3.5}$$

with a a positive constant of the order unity. In this way the maximum number of inserted spheres is approximately adapted to the overall density

of spheres at a given z_s. With $a = 2$ this interval is $[0, 20\rangle$ when spherocylinders with aspect ratio $L/D = 3$ are considered and around $[0, 30\rangle$ when the aspect ratio is $L/D = 5$ at sphere fugacities relevant to the demixing transition ($z_s \sim 1.0$).

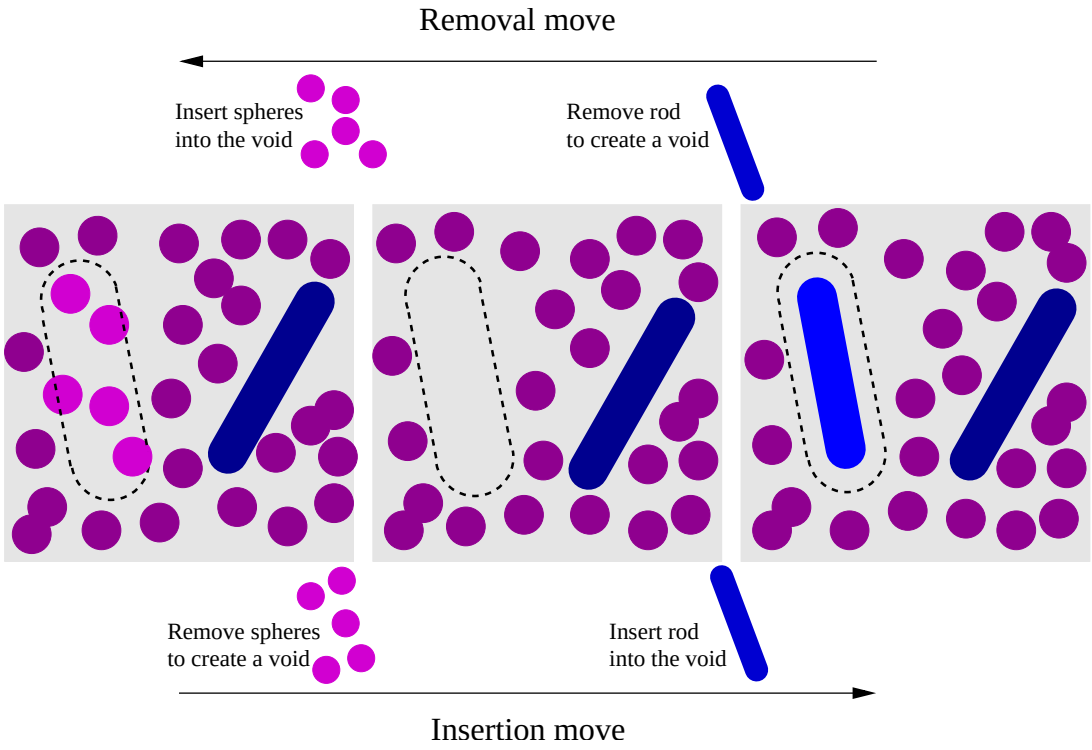

Figure 3.2: Cluster move.

Therefore, to generate the old configuration (with N_r rods and N_s spheres) from the new one (with $N_r + 1$ rods and $N_s - n_s$ spheres), the recently inserted spherocylinder has to be found $[1/(N_r + 1)]$ and the same number of spheres to be inserted which was removed before [$1/m$ is the probability to select n_s from the given interval] at their old positions inside the void created first to insert the spherocylinder [$1/V_{\mathrm{dz}}$ for each sphere]. Thus, the probabilities to generate the new state from the old one and to go back are

$$\begin{aligned} \mathcal{G}(o \to n) &= \frac{1}{4\pi V} \\ \mathcal{G}(n \to o) &= \frac{n_s!}{(N_r + 1) m V_{\mathrm{dz}}^{n_s}} \end{aligned} \tag{3.6}$$

where the factor $n_s!$ accounts for the fact that the spheres are indistinguishable. The Boltzmann probabilities of the old and the new states are

given by

$$\begin{aligned} \mathcal{N}(o) &= C z_r^{N_r+1} z_s^{N_s} e^{-\beta E_o} \\ \mathcal{N}(n) &= C z_r^{N_r} z_s^{N_s-n_s} e^{-\beta E_n} \end{aligned} \tag{3.7}$$

The Metropolis probability of accepting a new configuration is

$$\mathcal{A}(o \to n) = \min\left[1, \frac{z_r n_s! 4\pi V}{(V_{\mathrm{dz}} z_s)^{n_s} m(N_r+1)} e^{-\beta\Delta E}\right], \tag{3.8}$$

if $n_s < m$ and 0 else.

If only one spherocylinder is inserted and no spheres are removed, the acceptance probability is reduced to

$$\mathcal{A}(o \to n) = \min\left[1, \frac{z_r 4\pi V}{N_r+1} e^{-\beta\Delta E}\right] \tag{3.9}$$

For insertion of one sphere the acceptance probability is

$$\mathcal{A}(o \to n) = \min\left[1, \frac{z_s V}{N_s+1} e^{-\beta\Delta E}\right] \tag{3.10}$$

3.2.2 Removal moves

The cluster removal move starts with the selection of the spherocylinder to be removed $[1/N_r]$. Then, the number of spheres is selected to be inserted into the void produced by removal of the spherocylinder $[1/m]$. Then, n_s spheres have to be inserted into the depletion zone of the rod. The probability to find a specific position inside the void is $[1/V_z]$ for each sphere. And a factor $n_s!$ needs to be multiplied to account for all the ways the positions can be chosen. To come back to the old configuration the old position of the spherocylinder inside the simulation box $[1/V]$ as well as its old orientation $[1/(4\pi)]$ have to be found. Thus, the probabilities of switching between two states are

$$\begin{aligned} \mathcal{G}(n \to o) &= \frac{n_s!}{m N_r V_{\mathrm{dz}}^{n_s}} \\ \mathcal{G}(o \to n) &= \frac{1}{4\pi V} \end{aligned} \tag{3.11}$$

The Boltzmann probabilities are

$$\begin{aligned} \mathcal{N}(o) &= C z_r^{N_r} z_s^{N_s} e^{-\beta E_o} \\ \mathcal{N}(n) &= C z_r^{N_r - 1} z_s^{N_s + n_s} e^{-\beta E_n} \end{aligned} \tag{3.12}$$

The Metropolis probability of accepting a new configuration is

$$\mathcal{A}(o \to n) = \min \left[1, \frac{N_r m (z_s V_{\mathrm{dz}})^{n_s}}{4\pi V z_r n_s!} e^{-\beta \Delta E} \right] \tag{3.13}$$

If only one spherocylinder is removed and no spheres are inserted, the acceptance probability is reduced to

$$\mathcal{A}(o \to n) = \min \left[1, \frac{N_r}{4\pi V z_r} e^{-\beta \Delta E} \right] \tag{3.14}$$

The acceptance probability for removal of a single sphere is calculated similarly to give

$$\mathcal{A}(o \to n) = \min \left[1, \frac{N_s}{V z_s} e^{-\beta \Delta E} \right] \tag{3.15}$$

One subtle point in the cluster removal move of the spherocylinder is the insertion of spheres into the void. The new positions have to be selected uniformly from inside the depletion zone of the rod, which has a given orientation. To achieve that, one can start with a cylinder oriented in the z-direction, uniformly select the points inside and take into account those with a distance from the cylinder axis smaller that the radius of the spherocylinder. Then, the positional vectors are rotated such that the initial z-vector points into the direction of the removed spherocylinder. This rotation is described by the rotations of the Euler angles A, B and C with $A = 0$ (rotation around the z-axis can be ignored)

$$\begin{aligned} M &= \mathcal{R}(\mathcal{A})\mathcal{R}(\mathcal{B})\mathcal{R}(\mathcal{C}) \\ &= \begin{pmatrix} \cos(C)\cos(B) & \sin(C) & -\cos(C)\sin(B) \\ -\sin(C)\cos(B) & \cos(C) & \sin(C)\sin(B) \\ \sin(B) & 0 & \cos(B) \end{pmatrix} \end{aligned} \tag{3.16}$$

B and C calculated from the Cartesian coordinates of the initial orientation

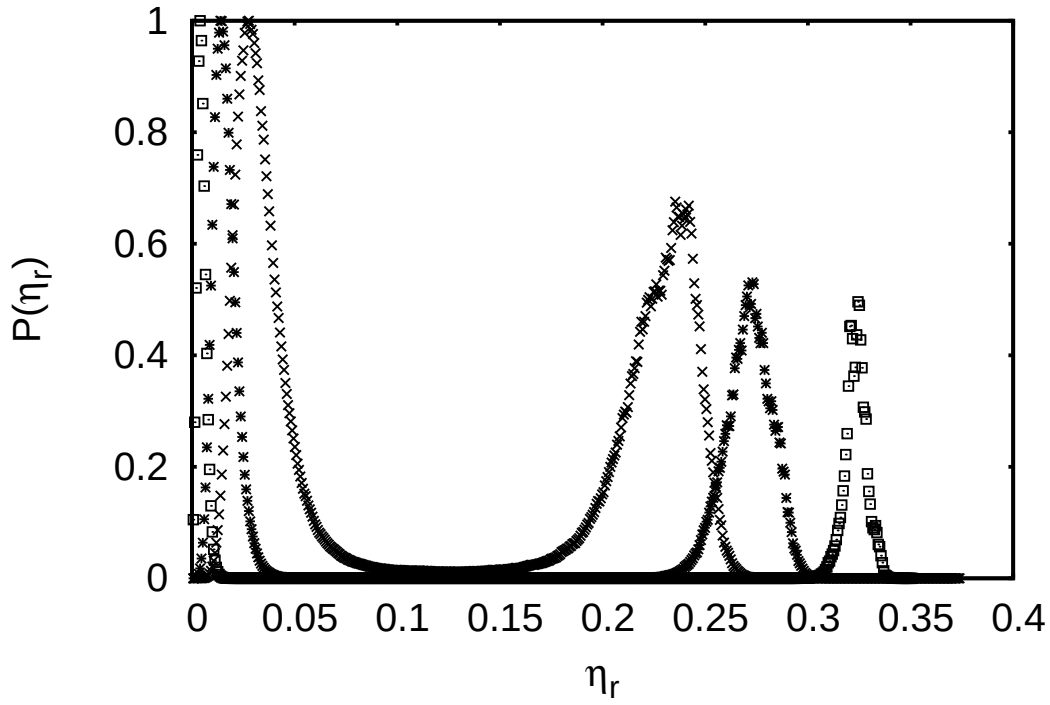

Figure 3.3: Probability (not normalised, but rescaled on the height of the first peak) to find a rod volume fraction $P(\eta_r)$ for spherocylinders of aspect ratio $L/D = 5$ at sphere fugacities $z_s = 1.0125$ (crosses), 1.0625 (stars) and 1.175 (squares).

(m_x, m_y, m_z) via

$$\begin{aligned} \cos(B) &= m_z \\ \sin(B) &= \sqrt{(m_x^2 + m_y^2)} \\ \cos(C) &= \frac{-m_x}{\sqrt{(m_x^2 + m_y^2)}} \\ \sin(C) &= \frac{m_y}{\sqrt{(m_x^2 + m_y^2)}} \end{aligned} \tag{3.17}$$

The sphere coordinates obtained in this way lie uniformly distributed in the depletion zone of the removed rod.

3.2.3 Successive umbrella sampling

The phase boundaries are determined from the probability distribution $P(N_r)$, which is the probability to observe N_r rods in the mixture for given

chemical potentials μ_r and μ_s. For a given value of μ_s (in this work the sphere fugacity z_s is usually used, which is connected to chemical potential via $z_s = \exp(\beta\mu_s)$), the value of μ_r at which the distribution is bimodal, i.e. there are two distinct states equally probable to be observed, is found. However, the simulations need not be performed right at the coexistence chemical potential (which is usually not known beforehand). In fact, the chemical potential (μ_{r0}) can be set to any value – here chosen to be zero — and then renormalised to coexistence (μ_{r1}) via

$$\ln[P_{\mu_{r1}}(N_r)] = \ln[P_{\mu_{r0}}(N_r)] + (\mu_{r1} - \mu_{r0})N_r \tag{3.18}$$

such that the areas under the two peaks in $P(N_r)$ are equal [Landau and Binder (2000)]

$$\int_0^{\langle N_r\rangle} P_{\mu_{r1}}(N_r)dN_r = \int_{\langle N_r\rangle}^{\infty} P_{\mu_{r1}}(N_r)dN_r \tag{3.19}$$

with

$$\langle N_r\rangle = \int_0^{\infty} N_r P_{\mu_{r1}}(N_r)dN_r \tag{3.20}$$

Examples of such probabilities $P(\eta_r)$ renormalised to coexistence are given in Figure 3.3. For spherocylinders of aspect ratio $L/D = 5$ and sphere fugacities $z_s = 1.0125$ (crosses), 1.0625 (stars) and 1.175 (squares) the corresponding values of the rod chemical potentials are $\mu_r = 10.54317$, 11.2067 and 12.6271.

In practise, the application of equation 3.18 requires that the $P(\eta_r)$ at the chemical potential μ_{r0}, at which the simulation is carried out, has sampled the range of η_r near both peaks in Figure 3.3 rather accurately already.

The mean values of the peak positions are the volume fractions of the coexisting states. The successive umbrella sampling method [Virnau and Müller (2004)] is used to determine $P(N_r)$. This technique allows to sample regions between the two bulk phases where $P(N_r)$ is very low. The range of densities to be investigated is divided into small windows and all of them are sampled consecutively, starting from an empty system. The natural size of a sampling window here is one, i.e. in every simulation up to 5×10^7, usually 3×10^7, insertion/removal moves per window are attempted.

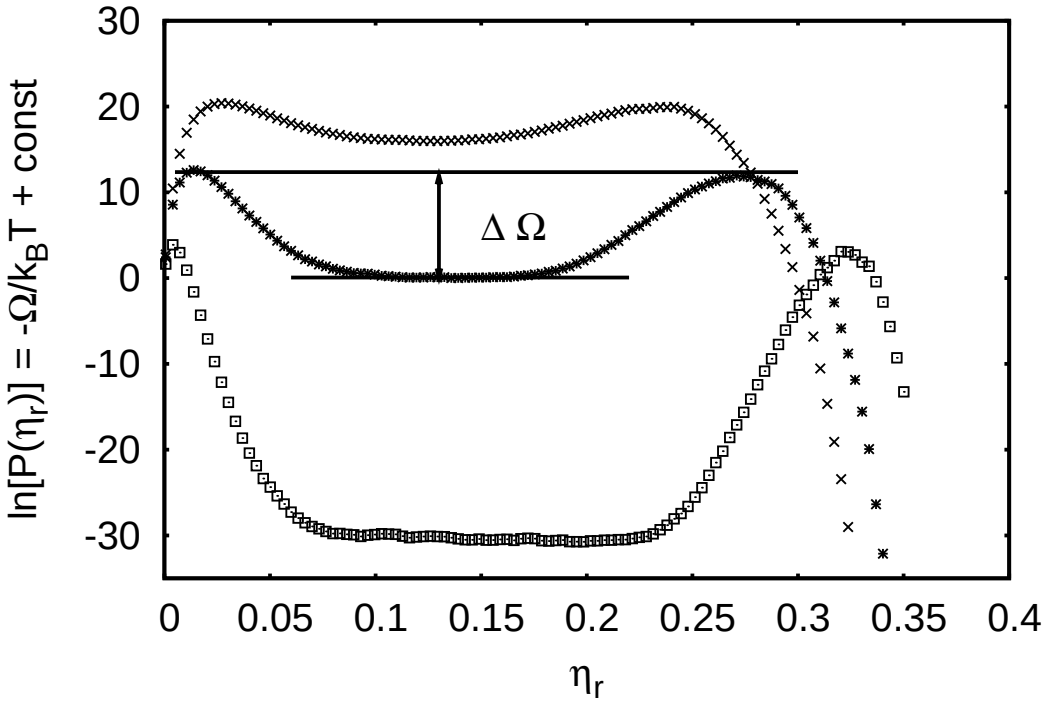

Figure 3.4: Grand potential $\ln[P(\eta_r)]$ for spherocylinders of aspect ratio $L/D = 5$ at sphere fugacities $z_s = 1.0125$ (crosses), 1.0625 (stars) and 1.175 (squares). $\Delta\Omega$ indicates the height of the grand potential barrier between the coexisting phases.

However, the system is not allowed to leave the window and any step, which would lead to that, is rejected straight away and not counted as a valid move. There are only two states per window – N_r and $N_r + 1$ – and the number of times (#) the system is found to be in each state is sampled. Here, the moves which tried to leave the window contribute to the border states, since one assumes that the system which happens to leave the window would sooner or later find back and come to that state from which it was not allowed to move in the first place. The probability to find N_r particles can be estimated recursively

$$\frac{P(N_r)}{P(0)} = \frac{\#(1)}{\#(0)}\frac{\#(2)}{\#(1)} \cdots \frac{\#(N_r)}{\#(N_r - 1)} \tag{3.21}$$

An easy access to the next state is allowed by using weighted simulations. The first window is usually unweighted. After $P(N_r)$ is calculated, the weight function

$$W(N_r) = \ln(P(N_r)) \tag{3.22}$$

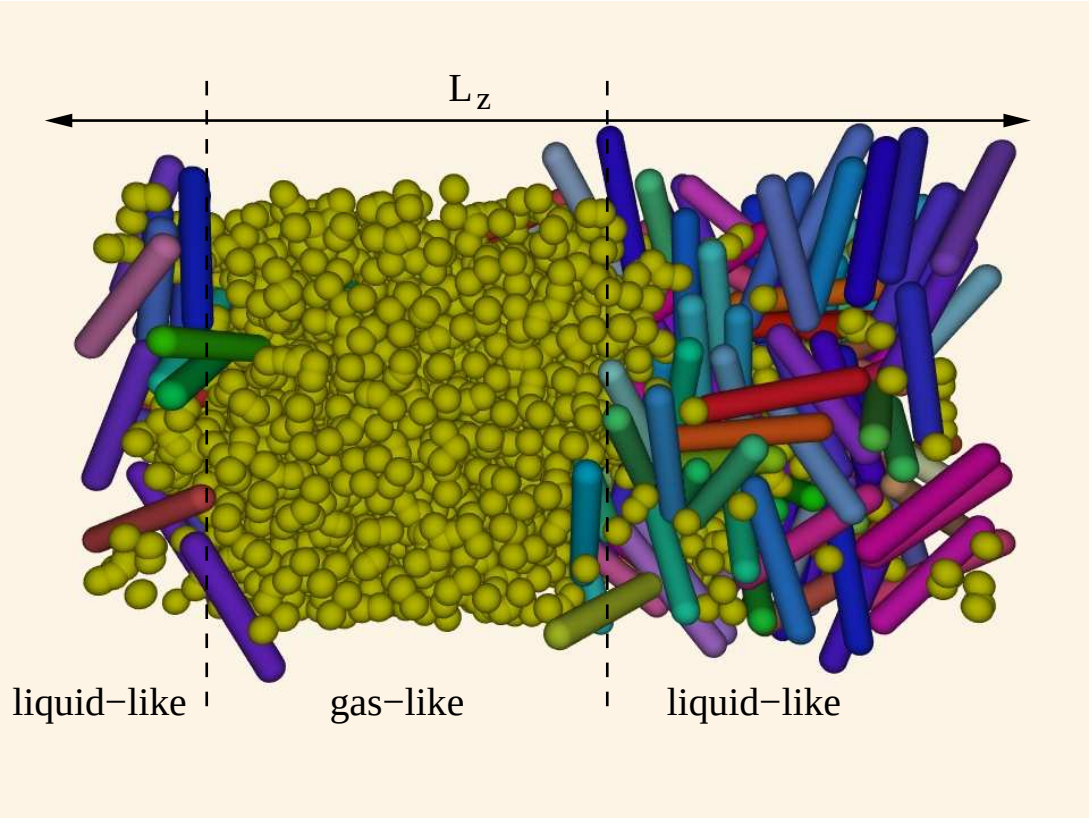

Figure 3.5: Configuration snapshot for $L/D = 5$ at coexistence.

is linearly extrapolated into the next window. To calculate the probability $P(N_r)$ in a weighted simulation, the number of times a state is found in the system, which is used in equation 3.21, has to be normalised by $\exp(W(N_r))$.

Figure 3.4 shows the logarithm of the probability distribution $P(N_r)$, which – up to an additive constant – is equal to the grand potential of the system. The mean values of the peaks in the probability distribution $P(N_r)$ are the bulk volume fractions of rods at coexistence. For a large fugacity z_s (squares), and hence a large concentration of spheres, there are two clearly separated peaks indicating a phase transition which is strongly of first order. With decreasing concentration of spheres (stars and crosses) the effective attraction between the rods becomes weaker. Hence the peaks move closer until eventually the critical point is reached. Finite size effects close to the critical point are analysed in Chapters 5 and 6. Away from the critical point the size of the simulation box influences the width and the

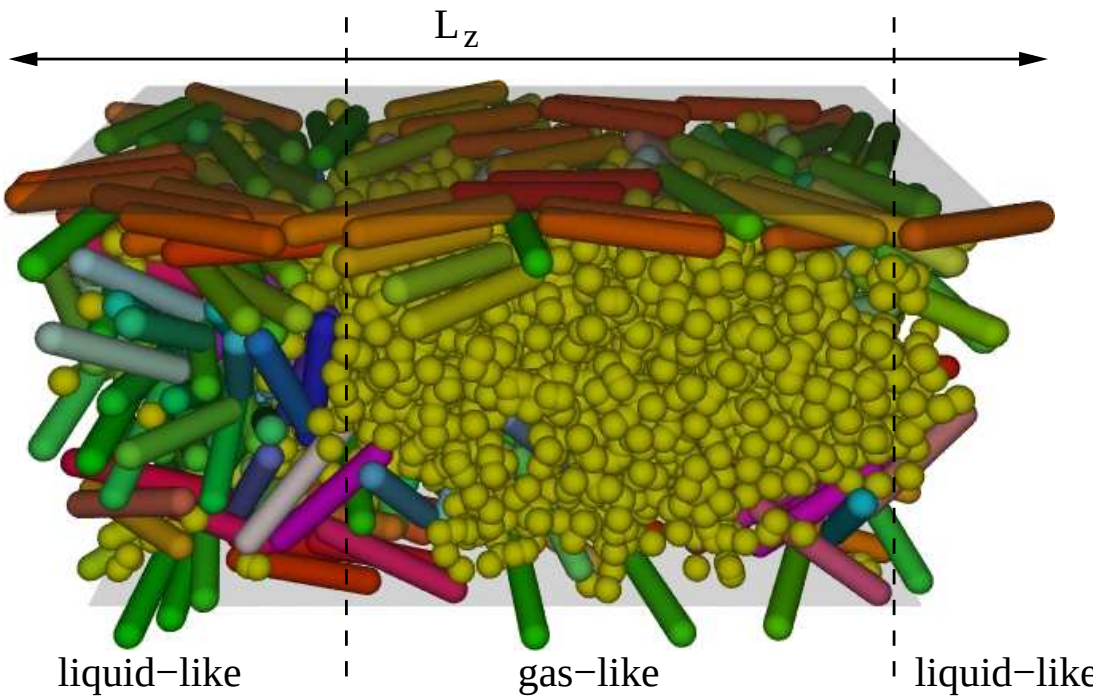

Figure 3.6: Configuration snapshot in confinement for $L/D = 5$ at coexistence. Wall separation $d = 3\ L$.

height of the peaks but not their positions. If the simulation box is chosen large enough, the position of the peaks does not change by changing the simulation box size, given the distance from the critical point is large.

Figure 3.5 shows a typical configuration at coexistence in the region where $\ln[P(\eta_r)]$ is almost horizontal. Because of the periodic boundaries two slabs separated by two interfaces (broken lines) have formed. Due to an elongated box the interfaces are formed perpendicular to the long axis, indicated in Figure 3.5 as L_z. The flat part between the peaks in the logarithm of the probability distribution in Figure 3.4 is formed by moving of these interfaces along the box. Since the free energies of the coexisting states are equal, change of the amount of one phase present in a system, which is associated with movement of interfaces, does not influence the overall free energy of the mixture. The barrier is due to the energy needed to create the interfaces between the phases.

3.3 Confinement

The mixture of hard spherocylinders and soft spheres was also simulated in confinement between two hard walls. The centres of spheres as well as the axis of spherocylinders were not allowed to come to the walls closer than their diameter. The phase boundaries were determined in the grand canonical ensemble in the same way as for the bulk system. The structure of the confined fluid, however, was studied in the canonical ensemble. The number of particles was chosen to match the coexistence values determined in the grand canonical ensemble. Although in principle the finite size effects are different in the canonical and grand canonical ensemble [Landau and Binder (2000)], far enough from the critical point this difference can safely be neglected.

Figure 3.6 shows a typical configuration at coexistence in confinement. The walls are presented as transparent grey planes. In addition to the two interfaces between the gas- and liquid-like phases (broken lines), which are due to the periodic boundary conditions like in the bulk case, two uniaxial layered films of spherocylinders at the walls are formed. Different from the bulk, the interfaces between the separated phases are not flat, but form an angle on the contacts with the walls.

3.4 Cell system

Simulations of systems containing a large number of particles can be very time-consuming. If in every step one has to check on every pair of particles (for interactions) in the simulation box, the running time of the algorithm scales with the squared number of particles. For isotropic particles with short-range interactions, hard spherical particles being a special case of them, the cell system method was established to speed up the simulations [Frenkel and Smit (2002)]. The simulation box is divided into cells of the size of particles and the interactions of a particle only with those other particles are calculated, which are in the cell of the first particle and in the neighbouring cells.

This approach works quite well for short rods. However, for long rods, the cells, whose size is defined by the length of the rods, become very large, destroying the advantages of the cell system method.

Thus, for simulations of anisotropic particles a special cell system [Vink and Schilling (2005)] was suggested for efficient overlap detection. In this approach the simulation box is cut into cubes of side length $\geq D$. Whether a rod intersects a cube or not can be computed very fast. The volume which needs to be checked for overlaps then contains at the most a few particles.

Chapter 4

Percolation

4.1 Introduction

The simple hard rod model can be used as a model of carbon nanotubes, which are actually graphite sheets wrapped into a cylindrical tube [Iijima (1991)]. Carbon nanotubes are often used as conducting fillers in modern composite materials [Baughman *et al.* (2002); Khare and Bose (2005)]. The electrical and thermal conductivities of carbon are remarkably high, which, combined with the rod-like shape of the tubes, allows production of light-weight, conducting composite materials using less amount of carbon in the samples than one would need when using spherical particles. An indicator of the density required to achieve a conducting sample is the so-called percolation threshold of the system. In a suspension of particles connected clusters are built up. At the percolation threshold, the biggest cluster in the system becomes infinite, alternatively, on the macroscopic scale and in the case of the conducting particles, the conductivity becomes non-zero.

Obviously, anisotropic particles with disordered positions and orientations enhance the conductivity in comparison to a network of spheres, since a single particle with large aspect ratio like carbon nanotube provides connectivity over a longer distance than several more spherical particles with the same total volume.

Not only the shape of the particles, but also the nature of the solvent can modify the value of the percolation threshold. In a recent experiment [Vigolo *et al.* (2005)] addition of depletion agent like sodium dodecyl sul-

fate micelles allowed a considerable lowering of the fraction of carbon nanotubes needed to achieve conductivity. The effect is not unexpected since it was predicted analytically for mixtures of rods and spherical depletants [Wang and Chatterjee (2003)], however, they did not take alignment into account. On the other hand, alignment of the rods would raise the percolation threshold and the depletion interactions are known to induce alignment. Hence, to have the desired lowering of the percolation threshold, the considered suspension should still be in an isotropic phase. Recently, an experimental study of the effect of the alignment of nanotubes on the percolation [Du *et al.* (2005)] reported that the highest conductivity was measured in a system where the nanotubes were slightly aligned. It confirmed the previous analytical analysis of the dependence of the percolation on the alignment [Munson-McGee (1991)].

In this Chapter the effect of the depletion forces on the value of the percolation threshold is presented. Attention is paid to the structure of the fluid and its variation with the amount of depletant added to the mixture.

Also the demixing into the gas- and liquid-like isotropic phase described in Chapter 5 would prevent percolation. For longer rods the demixing into gas-like isotropic and liquid-like nematic phase would be of importance. Nevertheless, even in the comparatively small window in the phase diagram, where the rod-sphere mixture is still isotropic, the effects of the depletion forces on the value of the percolation threshold are considerable.

4.2 Percolation threshold

Carbon nanotubes are very long and thin particles ($L/D = 200 - 800$), however, in the suspensions they usually form bundles, whose aspect ratio can exceed 100. This value is still beyond the reach of an usual simulation. Nevertheless, the emergence of the long-rod behaviour becomes clear by simulating increasing L/D starting from relatively small values. Figure 4.1 demonstrates the effect of depletion forces on the percolation threshold in a fluid of rods with aspect ratio $L/D = 4$. The equilibrium probability of finding a percolating cluster, $\Pi(\eta_r)$, is plotted as a function of the rod vol-

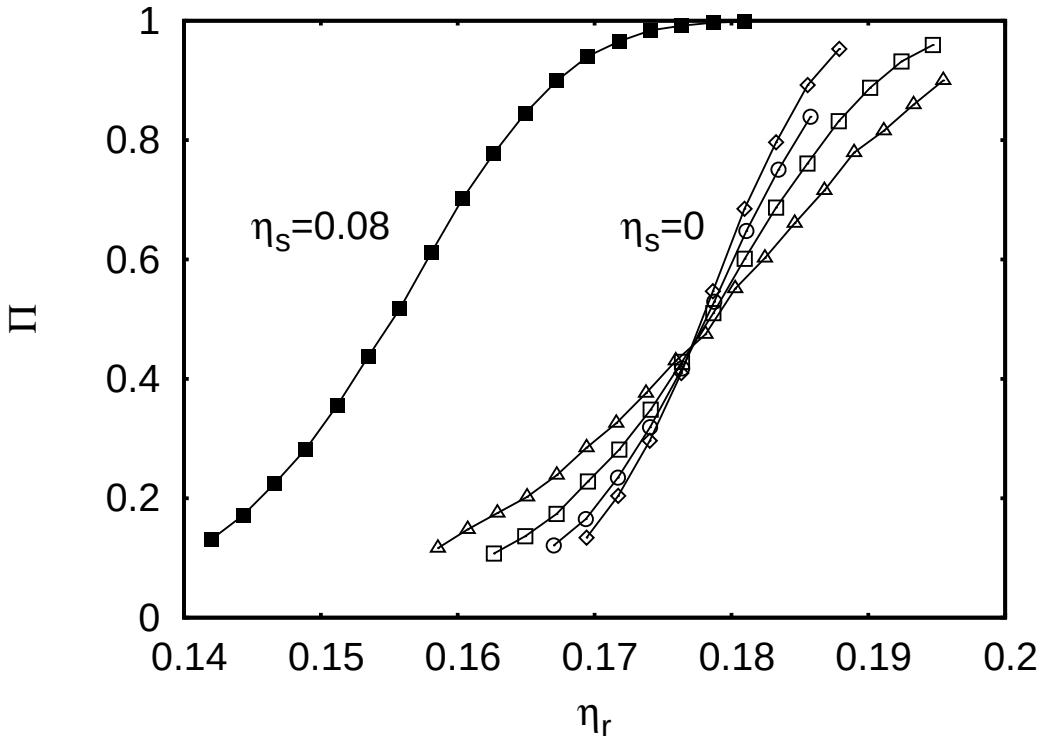

Figure 4.1: Percolation probability Π as a function of the rod volume fraction for $L/D = 4$ and sphere volume fractions $\eta_s = 0$ and 0.08 in a box of edge $L_x = 15\ D$ (open triangles), 20 D (open and filled squares), 25 D (open circles) and 30 D (open diamonds). Solid lines are guides to the eyes.

ume fraction $\eta_r = N_r v_r/V$ with v_r volume of a spherocylinder. Addition of a volume fraction $\eta_s = 0.08$ of spheres (filled squares), where $\eta_s = N_s v_s/V$ and v_s volume of a sphere, shifts the percolation probability to lower rod volume fraction, compared to the pure rod fluid (open squares). Before coming to the systematical studies of the dependence of the percolation threshold on the rod length and sphere concentration, the position of the percolation threshold is defined, and the finite size effects are analysed in the next section.

4.2.1 Finite size effects

In an infinite system, the percolation probability would rise instantaneously at the percolation threshold, but the simulations measure a sigmoidal curve whose width decreases with increasing box size due to finite size effects,

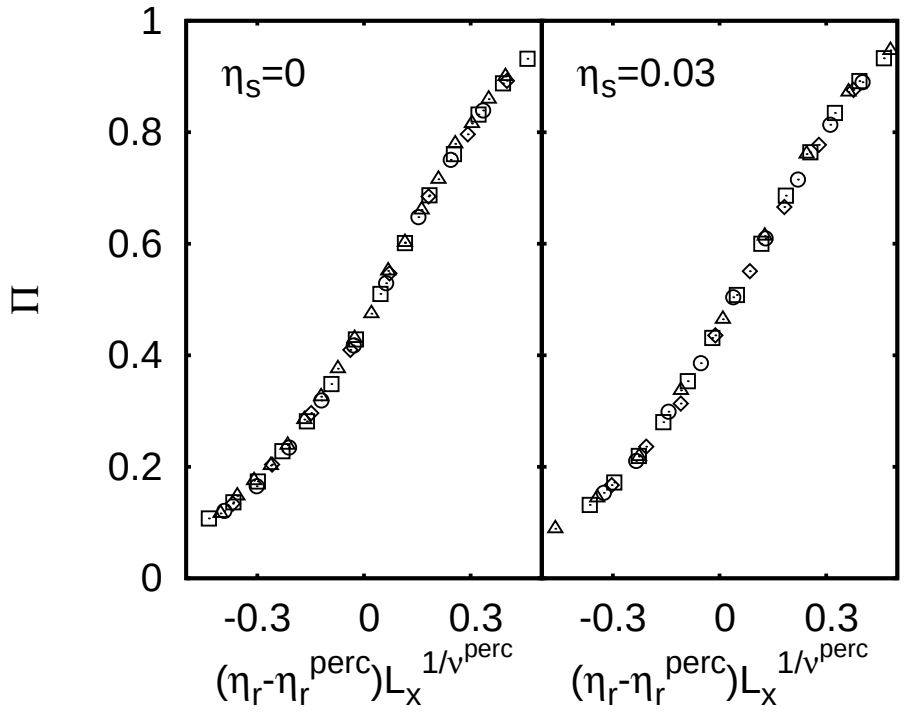

Figure 4.2: Percolation probability Π as a function of the distance from the percolation threshold and system size for rods of $L/D = 4$ with (right frame) $\eta_s = 0.03$ and without (left frame) spheres for box edges $L_x = 15\ D$ (open triangles), $20\ D$ (open squares), $25\ D$ (open circles) and $30\ D$ (open diamonds). $\nu^{\mathrm{perc}} = 0.88$ is the correlation length critical exponent.

as demonstrated in the Figure 4.1 for the pure rod case. Nevertheless, the volume fraction at which $\Pi(\eta_r)$ passes through 0.5 is almost independent of the box size and therefore

$$\Pi(\eta_r^{\mathrm{perc}}) = 0.5 \tag{4.1}$$

can be adopted as a robust definition of the percolation threshold η_r^{perc}.

The finite size dependence observed here is consistent with the predictions of the percolation theory [Stauffer and Aharony (1994)]. According to it, the probability to find a percolating cluster is a function of the distance from the percolation threshold and the system size L_x in a particular scaled combination

$$\Pi(\eta_r, L_x) = f_1[(\eta_r - \eta_r^{\mathrm{perc}})L_x^{1/\nu^{\mathrm{perc}}}]. \tag{4.2}$$

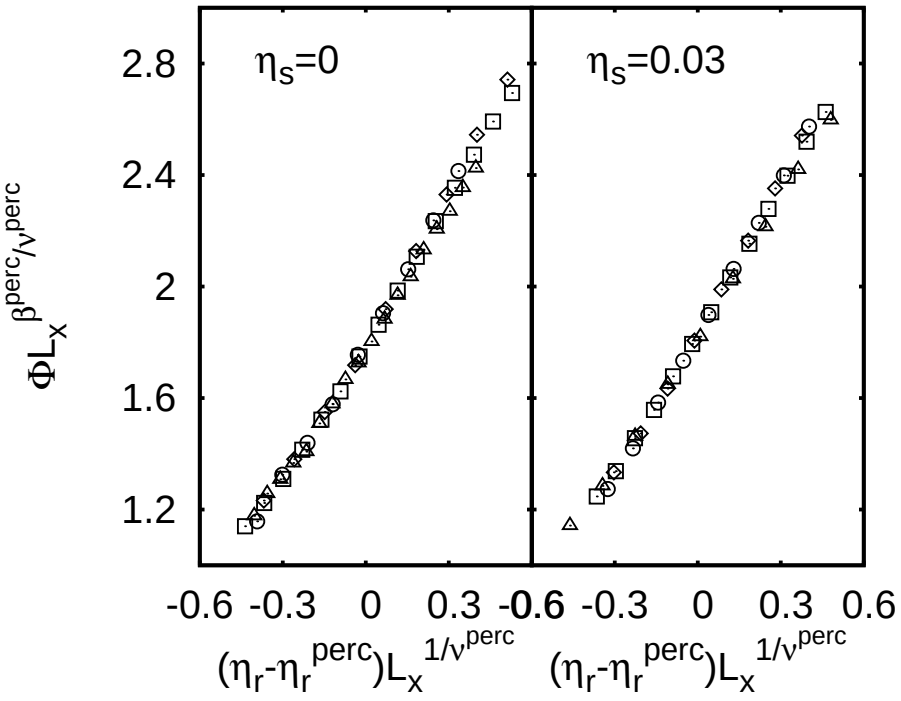

Figure 4.3: Scaling of the percolating fraction Φ with the distance from the percolation threshold and system size for rods with $L/D = 4$ and sphere volume fractions $\eta_s = 0$ (left frame) and 0.03 (right frame). Box edges are $L_x = 15\ D$ (open triangles), 20 D (open squares), 25 D (open circles) and 30 D (open diamonds).

The correlation length critical exponent ν^{perc} equals 0.88 in the case of three dimensional continuum percolation, while the function f_1 is not known explicitly.

Figure 4.2 replots the percolating probabilities, obtained for pure rod case (left frame) in simulation boxes with edge lengths $L_x = 15\ D$ (open triangles), 20 D (open squares), 25 D (open circles) and 30 D (open diamonds) as indicated in Figure 4.1, in terms of the finite size scaling concept applied for the percolation theory. Obviously, all data sets lie on one curve, which corresponds to the function f_1. The scaling is the same for the mixture containing $\eta_s = 0.03$ spheres, as indicated on the right frame of Figure 4.2, where η_r^{perc} is the percolation threshold of the mixture.

Another prediction of the percolation theory can also be confirmed here on the example of the percolating fraction of rods, Φ. It is predicted to scale

L/D	$\eta_r^{\mathrm{perc}}(\eta_s = 0)$	$\eta_r^{\mathrm{perc}}(\eta_s = 0.03)$	δ
4	0.1783	0.1692	0.054
8	0.1378	0.1294	0.065
12	0.1121	0.1045	0.073
16	0.0946	0.0878	0.077
18	0.0877	0.0812	0.080

Table 4.1: Percolation threshold for selected aspect ratios L/D at two sphere volume fractions η_s. δ is the fractional decrease in η_r^{perc} caused by spheres volume fraction $\eta_s = 0.03$.

like

$$\Phi \sim (\eta_r - \eta_r^{\mathrm{perc}})^{\beta^{\mathrm{perc}}} \tag{4.3}$$

in an infinite system and it is expected to obey the general finite size scaling relation

$$\Phi(\eta_r, L_x) = (\eta_r - \eta_r^{\mathrm{perc}})^{\beta^{\mathrm{perc}}} f_2[(\eta_r - \eta_r^{\mathrm{perc}}) L_x^{1/\nu^{\mathrm{perc}}}]. \tag{4.4}$$

in a finite system. Again, the critical exponent $\beta^{\mathrm{perc}} = 0.41$ is known from the percolation theory, while the function f_2 is not known analytically. Figure 4.3 shows the behaviour of the percolating fraction of rods for systems with (right frame) and without (left frame) spheres in terms of the scaling representation. Once more, like in Figure 4.2, the simulation box edges are $L_x = 15\ D$ (open triangles), $20\ D$ (open squares), $25\ D$ (open circles) and $30\ D$ (open diamonds). Since the difference $\eta_r - \eta_r^{\mathrm{perc}}$ is a function of the box size, the multiplication of $L_x^{\beta^{\mathrm{perc}}/\nu^{\mathrm{perc}}}$ on both sides of the equation 4.4 transforms its right hand side into a single function of $(\eta_r - \eta_r^{\mathrm{perc}}) L_x^{1/\nu^{\mathrm{perc}}}$.

Figure 4.3 demonstrates that the addition of spheres to the fluid of isotropic rods does not influence the scaling behaviour of the percolation fraction with respect the percolation threshold, although the position of the threshold itself is shifted.

4.2.2 Aspect ratio dependence

As expected, η_r^{perc} is lower for longer rods, as shown for a selection of values for L/D and at sphere volume fractions $\eta_s = 0$ and 0.03 in Table 4.1. The fractional decrease δ in the percolation threshold due to the spheres is

5.4% at $L/D = 4$, rising gradually to 8.0% for $L/D = 18$ in contrast to theoretical predictions of constant δ [Wang and Chatterjee (2003)]. The increasing shift is likely to continue as the aspect ratio rises towards that typical of carbon nanotube bundles. However, if a scaling regime of the form $\eta_r^{\mathrm{perc}}(L/D)^{-a}$ is entered for sufficiently long rods, and the value of a is not affected by the presence of spheres, then the fractional drop in η_r^{perc} caused by a given volume fraction of spheres would eventually become independent of the aspect ratio.

In fact, such a scaling behaviour has been predicted for ideal systems of freely interpenetrable rods. In the hope of estimating percolation thresholds without the need for detailed calculation, several quantities have been suggested as approximate dimensional invariants at the percolation threshold. Candidates included the number of bonds per particle, the total excluded volume [Balberg *et al.* (1984); Pike and Seager (1974)], and the zero of the Euler characteristic [Mecke and Seyfried (2002)]. Although none of the approaches works universally well for arbitrary particle shapes and mixtures, the quantity $\rho^{\mathrm{perc}}\langle v_{\mathrm{ex}}\rangle$ is an approximate invariant for ideal rods [Foygel *et al.* (2005)], where ρ^{perc} is the number density at percolation and $\langle v_{\mathrm{ex}}\rangle$ is the so-called excluded volume (orientationally averaged) that would be inaccessible to the centre of one particle due to the presence of another if overlaps were forbidden. Defining the total critical volume by

$$V_c = \rho^{\mathrm{perc}} v \tag{4.5}$$

where v is the volume of an ideal rod, the invariant becomes $V_c\langle v_{\mathrm{ex}}\rangle/v$. For long rods, $\langle v_{\mathrm{ex}}\rangle/v \propto L$ and hence $V_c \propto 1/L$.

Ideal rods, i.e. freely interpenetrable rods, rapidly enter this scaling regime [Foygel *et al.* (2005)], as shown by open squares and by the straight line in Figure 4.4. Each evaluation of the percolation probability was obtained using the same box size and connectivity criterion as in the spherocylinder simulations. The introduction of the hard core induces local structure into the isotropic fluid and rules out a large fraction of percolating ideal configurations, raising the percolation threshold as indicated by the solid squares in Figure 4.4. For the aspect ratios accessible to the present simulations, no power-law scaling is observed. However, the theoretical reference

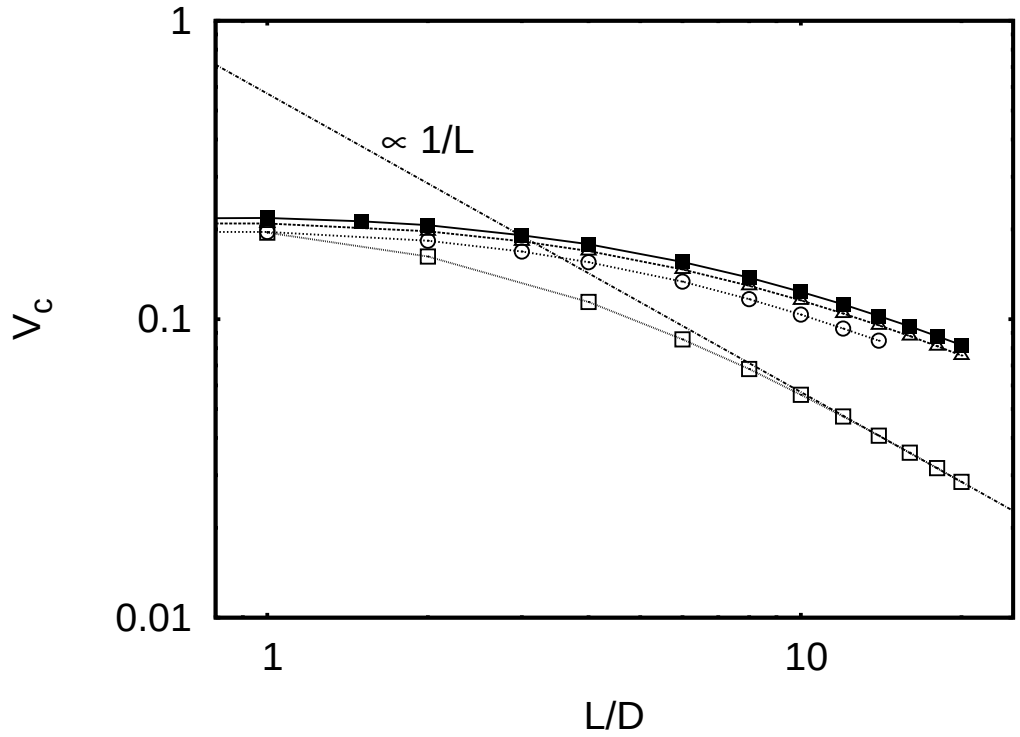

Figure 4.4: Dependence of the total critical volume on the aspect ratio of the rods for sphere volume fractions $\eta_s = 0$ (solid squares), 0.03 (open triangles) and 0.08 (open circles), and for the freely penetrable rods (open squares) without spheres. Curves are guides to the eyes. The straight line indicates $1/L$ scaling observed for ideal rods.

interaction site model (RISM) predicts that the effect of a hard core is to postpone scaling to larger aspect ratios and that $1/L$ scaling is eventually recovered [Leung and Chandler (1991)].

Table 4.1 shows a decline in the rate of increase of δ with L/D, and in the scaling regime δ would level out to a constant.

For very short rods, there is a surprising rise in the percolation threshold when L/D is varied. Although the percolation threshold of spherocylinders is expected to be lower than the one of spheres ($L/D = 0$), this is true only for spherocylinders with aspect ratio $L/D > 2$. For shorter rods a peak occurs at $L/D = 1$. Figure 4.6 includes the values of the percolation threshold for short rods. The effect is visible for the case with $\eta_r = 0.03$ (open squares) as well as without (filled squares) spheres.

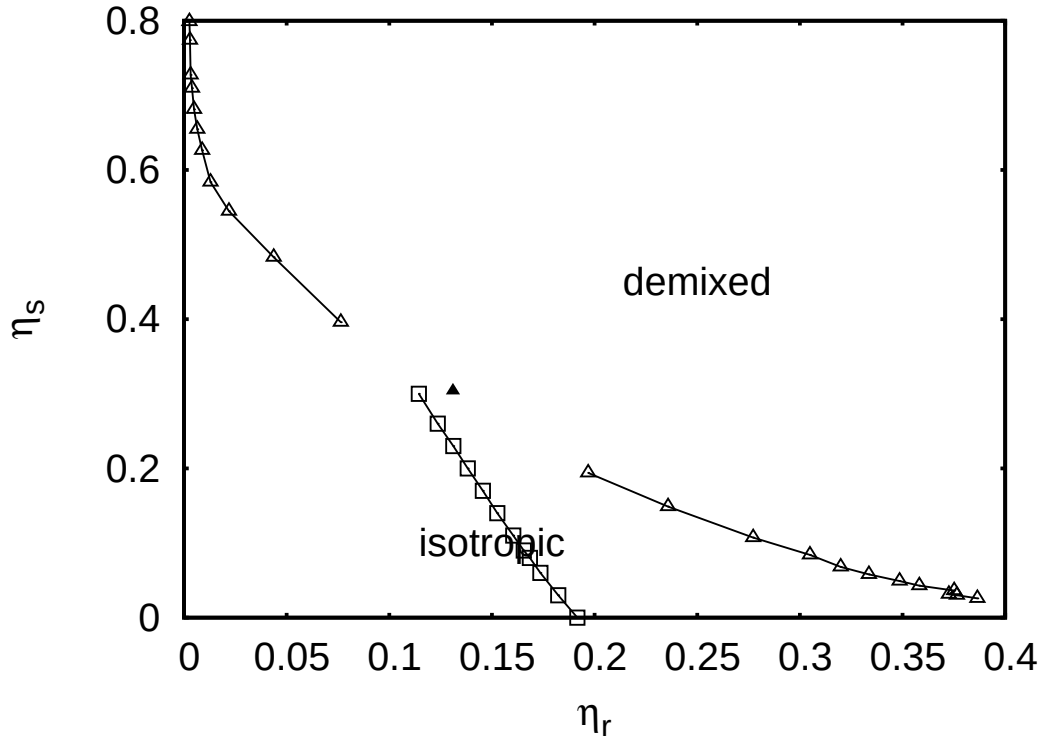

Figure 4.5: Bulk phase diagram for a mixture of rods with $L/D = 3$ (open triangles) combined with percolation thresholds for varying sphere volume fractions (open squares). The solid triangle indicates demixing critical point. The full curves are guides to the eyes.

4.2.3 Dependence on the sphere volume fraction

On increase of the volume fraction of spheres in the suspension, the system finally comes in the region of the demixing transition as demonstrated in Figure 4.5 for rods with aspect ratio $L/D = 3$. The percolation thresholds (open squares) are included in the bulk phase phase diagram of the isotropic-isotropic separation into rod-poor/sphere-rich and rod-rich/sphere-poor phases, which is presented in Chapter 5. The demixing transition would prevent three dimensional percolation, which is considered here. Note that in three dimensions the percolation line does not hit the critical point of the demixing transition of the system.

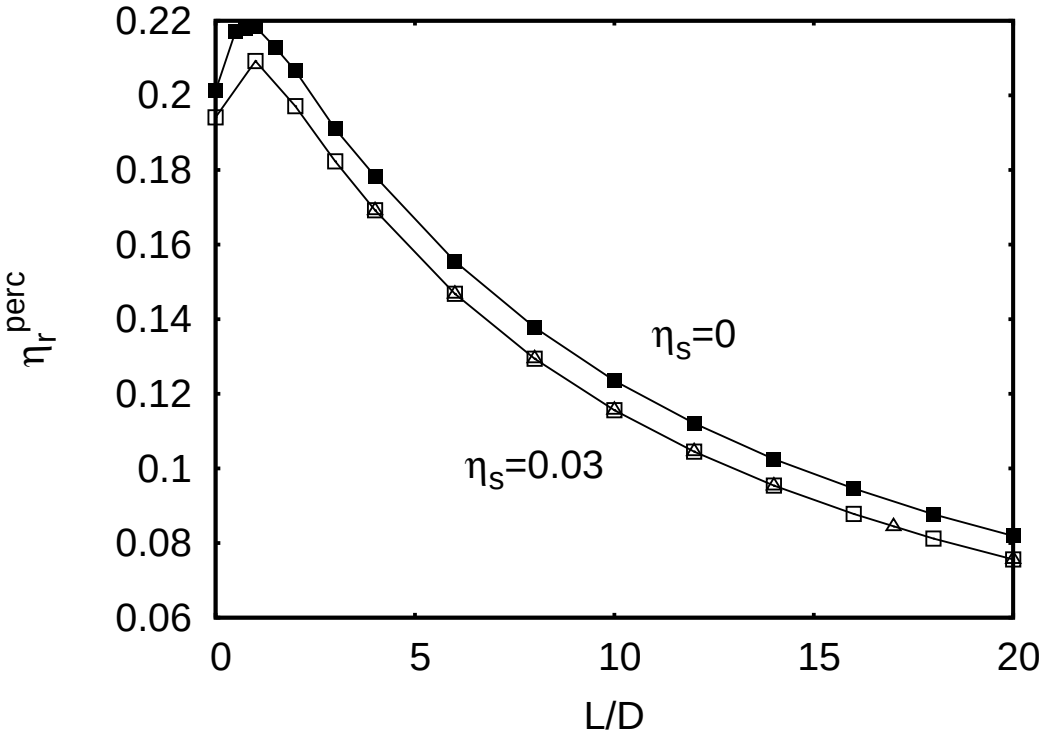

Figure 4.6: Percolation threshold as a function of the rod aspect ratio for the pure rod system (filled squares) and with volume fraction $\eta_s = 0.03$ of ideal (open squares) and hard (open triangles, from [Schilling (2007)]) spheres.

4.2.4 Nature of depletant

Completely hard spheres were also used to study effects of depletion on the percolation transition. It turns out that at the concentrations of spheres considered here, i.e., such that no demixing can occur, the nature of the depletant does not play a role, only its size. Results obtained for the system with hard spheres [Schilling (2007)] are compared with the case of the ideal spheres in Figure 4.6. Apparently, the hard spheres are still sparse enough to behave like an ideal gas.

4.3 Structure of the fluid

The isotropic phase considered here has no long-range order in either the centre-of-mass positions or the alignment of the rods. However, the hard interactions give rise to local structure, which is affected by the addition

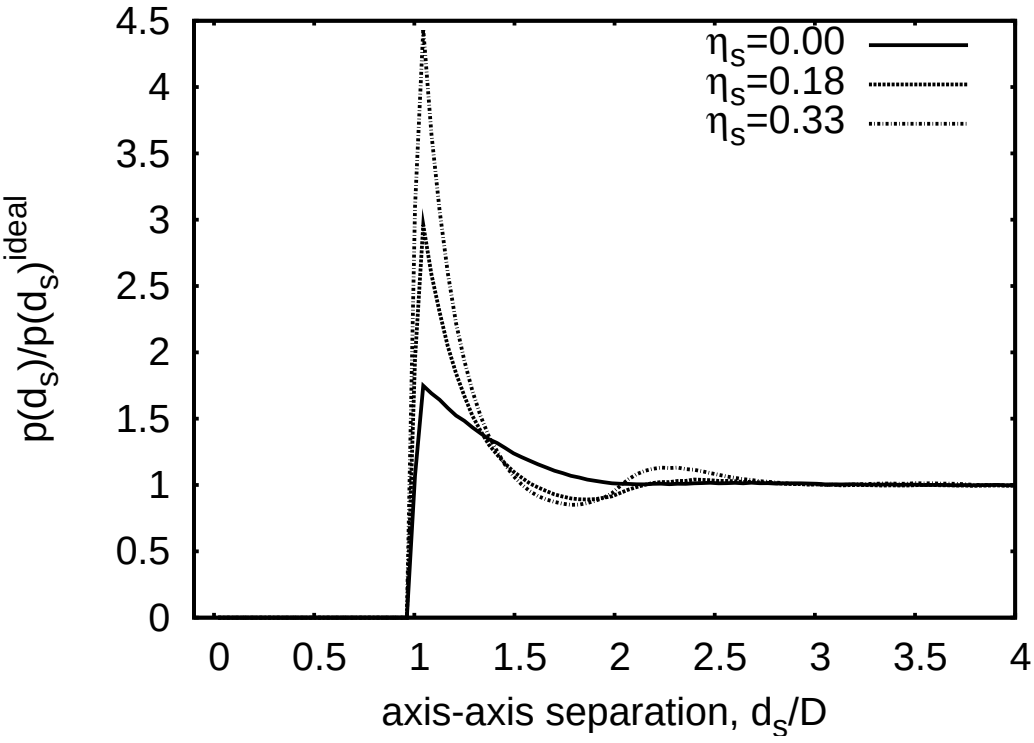

Figure 4.7: Probability distribution $p(d_s)$ of axis-axis separations d_s normalised by the distribution of ideal rods. Rod volume fraction $\eta_r = 0.16$, aspect ratio $L/D = 4$. Sphere concentrations as indicated.

of spheres. Local positional order is described by the radial distribution function $g(r)$, Figure 4.8, which will be discussed below. Local alignment is revealed by the orientational correlation function

$$g_2(r) = \langle P_2(\mathbf{u}_i \cdot \mathbf{u}_j) \rangle_r \tag{4.6}$$

where

$$P_2(x) = \frac{3x^2 - 1}{2} \tag{4.7}$$

is the second Legendre polynomial, and the averaging is restricted to pairs of rods whose centres are separated by $r_{ij} = r$. As shown in Figure 4.9, $g_2(r)$ decays to zero in an isotropic fluid, but becomes positive when rods approach closely enough to restrict each others orientation. The addition of spheres to the rods encourages nearby rods to align, since alignment decreases the total volume excluded to the spheres by an amount proportional to the length of the adjacent segment, thereby increasing the entropy of the spheres at the expense of some orientational entropy of the rods. Fig-

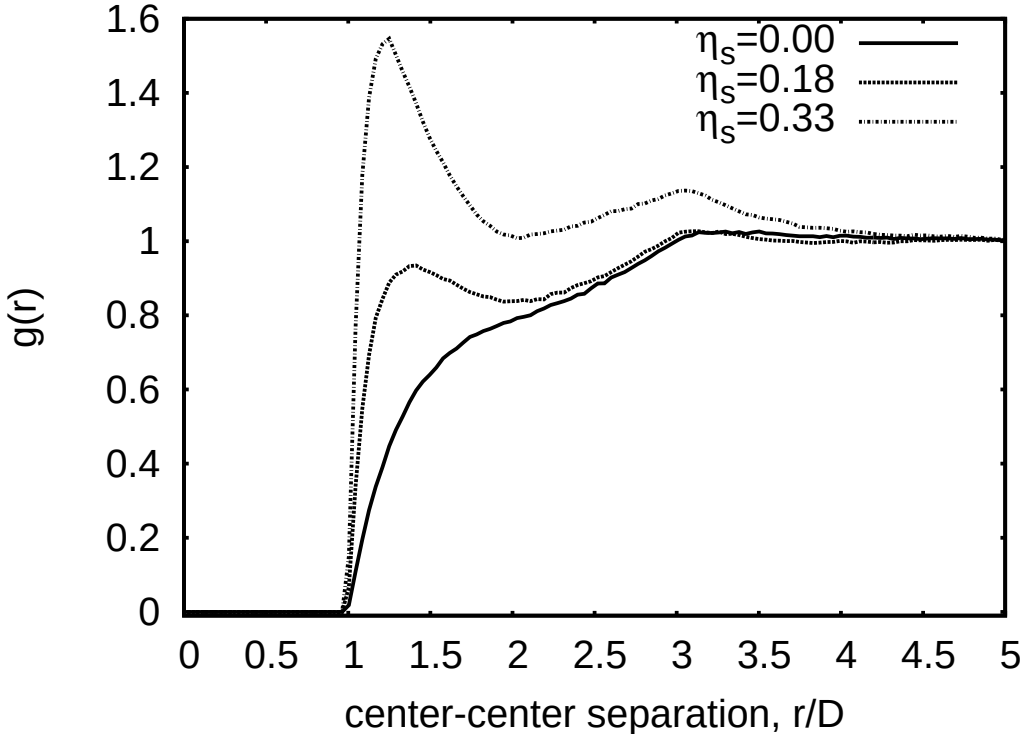

Figure 4.8: Radial distribution function $g(r)$. Rod volume fraction $\eta_r = 0.16$, aspect ratio $L/D = 4$. Sphere concentrations as indicated.

ure 4.9 shows that the spheres greatly enhance alignment of the rods with nearby centres, while, as Figure 4.8 demonstrates, the centres themselves are pushed closer together by addition of depletant. The range of the effect is on the order of the sphere diameter D and decays to the underlying correlation, whose range depends on the rod length L. The results presented in Figures 4.9, 4.8 and 4.7 are for spherocylinders with aspect ratio $L/D = 4$ and sphere concentrations $\eta_s = 0$ (solid lines), 0.18 (dashed lines) and 0.33 (dot-dashed lines). Crucial to cluster formation and percolation is the probability distribution $p(d_s)$ of shortest distances d_s between pairs of rod axes, since it is the criterion $d_s < A$ that defines contact. To reveal the effect of the hard potential on the structure, $p(d_s)$ is divided by the equivalent distribution $p_{\text{ideal}}(d_s)$ for ideal rods. The ratio $p(d_s)/p_{\text{ideal}}(d_s)$ is plotted in Figure 4.7. As with the first peak in the radial distribution function of a simple liquid, the distribution of axis-axis separations rises above the random distribution for small d_s. The addition of spheres again has a large but short-ranged effect on the distribution, pushing the rods

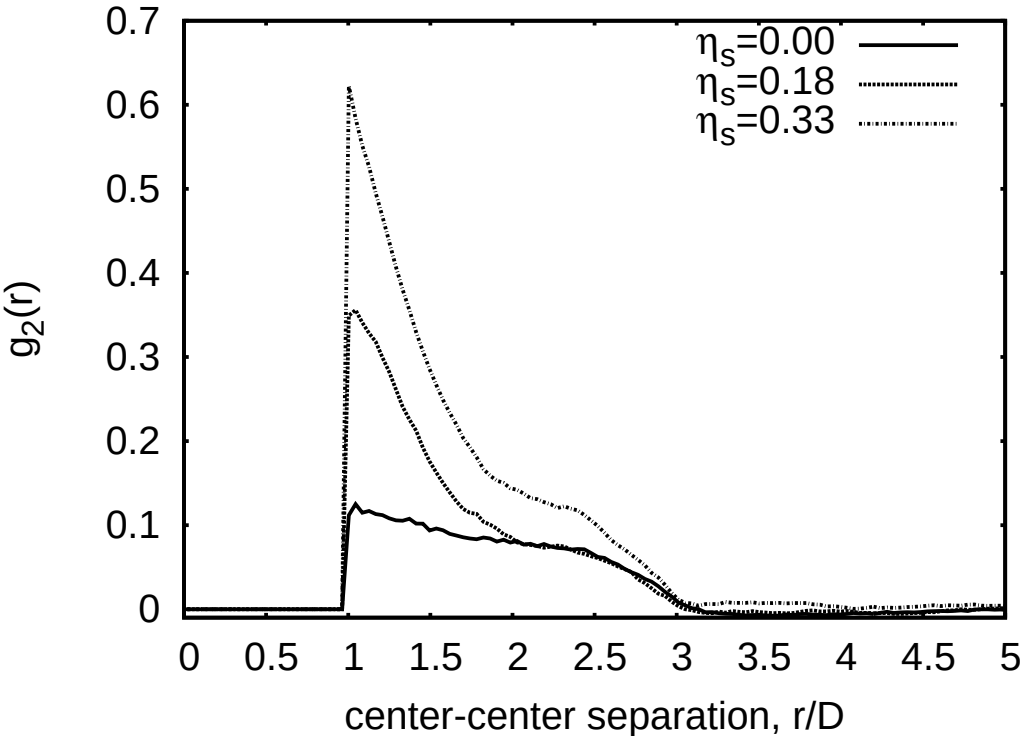

Figure 4.9: Orientational correlation function $g_2(r)$. Rod volume fraction $\eta_r = 0.16$, aspect ratio $L/D = 4$. Sphere concentrations as indicated.

together at any point of approach along their lengths.

4.4 Summary

The effect of depletion on the onset of the percolation was studied on a simple model of hard spherocylinders and ideal spheres. The spheres induce pronounced but short-ranged changes in the structure of the isotropic rod fluid, including enhanced local alignment. At depletant concentrations relevant to experimental work on suspensions of carbon nanotubes and micelles [Vigolo *et al.* (2005)], the alignment is too weak to cause global nematic order or significant aggregation of rods. Although pairs of particles extend less far when mutually aligned, depletion enhances contacts at all positions along the rods, leading to larger clusters and a decrease in the percolation threshold. The percolation threshold is lowered on addition of depletant interactions for all rod lengths and sphere concentrations considered here.

The nature of the depletant also seems to be unimportant, as long as the interactions between the spheres and the spherocylinders are hard, such that the rods are attracted to each other, the percolation threshold is lowered in the same way for the ideal and for the hard spheres.

Addition of a very large amount of depletant would finally result in phase separation of the mixture. Depending on the length of the spherocylinders isotropic-isotropic or isotropic-nematic demixing would destroy the three dimensional percolation.

Chapter 5

Bulk phase behaviour

5.1 Introduction

In this Chapter the bulk isotropic-isotropic demixing of the rod-sphere mixture is discussed. When the chemical potential of spheres, which in the present system plays the role of the inverse temperature, is high enough, the rods separate into a rod-poor isotropic (gas-like) phase, in which most of the spheres are present, and a rod-rich, also isotropic, (liquid-like) phase. According to free volume theory [Lekkerkerker *et al.* (1992); Lekkerkerker and Stroobants (1994)], this transition is stable for rod aspect ratios less then 7 in a mixture of rods and spheres of the same diameter. For longer rods the isotropic-isotropic phase is preempted by the isotropic-nematic demixing, where the liquid-like phase of rods shows orientational ordering.

This system was studied within liquid-state integral equation theory [Chen and Schweizer (2002, 2004); Cuetos *et al.* (2007)] and free volume theory [Lekkerkerker *et al.* (1992); Lekkerkerker and Stroobants (1994)] as well as with computer simulations [Li and Ma (2005); Bolhuis *et al.* (1997); Savenko and Dijkstra (2006)]. In recent years various regimes of size-ratios and concentrations have been discussed, e.g., the packing properties at very high concentrations or the behaviour of thin rods, which act as depletant on large spheres. The phase diagram of this model was studied within free volume theory by Lekkerkerker and Stroobants [Lekkerkerker and Stroobants (1994)]. Li and Ma recently computed the effective interaction between two rods by Monte Carlo simulation [Li and Ma (2005)]. Bolhuis *et al.* [Bol-

huis *et al.* (1997)] as well as Savenko and Dijkstra [Savenko and Dijkstra (2006)] determined the bulk rod-sphere phase diagram by simulation (via thermodynamic integration). Both have given results for rods of aspect ratio $L/D = 5$ and spheres of several diameter values. In order to avoid simulating the spheres explicitly, Savenko and Dijkstra used an exact expression for the effective Hamiltonian, which was numerically evaluated during the Monte Carlo simulation for each rod configuration. Bolhuis *et al.* [Bolhuis *et al.* (1997)] modelled the spheres explicitly in their Gibbs Ensemble Monte Carlo simulations to study fluid-fluid separation, while for the other parts of the phase diagram they used an effective expression for the rod-rod interaction.

Here, results for mixtures of rod-like particles and explicitly simulated spheres are presented, which were obtained in the grand canonical ensemble. The successive umbrella sampling method [Virnau and Müller (2004)] was employed to determine the grand potential hypersurface of the system. This allowed prediction of the phase boundaries of isotropic-isotropic coexistence with much higher accuracy than the studies mentioned above, which used thermodynamic integration. In particular, the critical point can be determined by a finite size scaling analysis.

5.2 Phase boundaries from the grand canonical simulations

The phase diagram is presented choosing the fugacity of the spheres and the rod volume fraction as variables. The fugacity z_s is related to the sphere reservoir volume fraction, which is often used in theoretical descriptions of such kinds of mixtures, via

$$\eta_s^R = z_s v_s \tag{5.1}$$

where $v_s = \pi D^3/6$ is the volume of a sphere. Explicit implementation of the spheres allows an easy transformation into the frame of (η_s, η_r), where η_s is the sphere volume fraction in the system, which are the more convenient coordinates for the comparison with experiments. In free volume theory, which is briefly reviewed in Appendix A, the actual concentration of spheres follows as

$$\eta_s = \alpha \eta_s^R \tag{5.2}$$

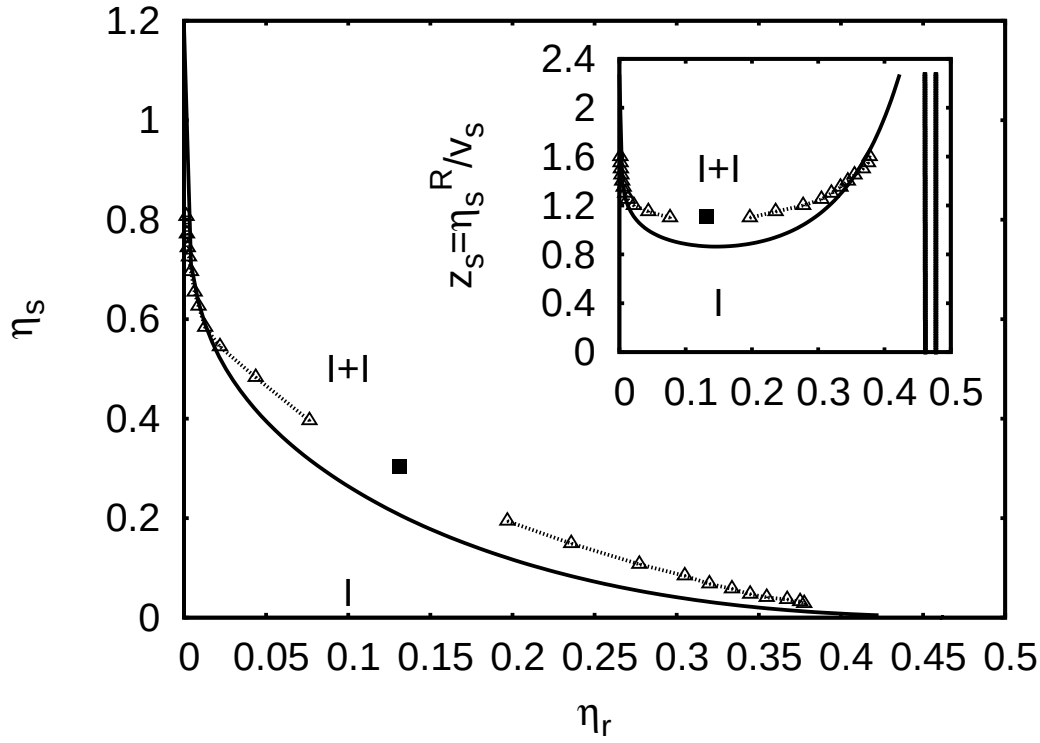

Figure 5.1: Bulk phase diagram for a mixture of spherocylinders with aspect ratio $L/D = 3$ and spheres of diameter D. The solid lines are predictions of the free volume theory, while the dotted lines are guides to the eyes. The filled square marks the critical point. The inset shows the phase diagram in the (z_s, η_r)-plane. The almost vertical lines in the inset indicate the coexistence region of the isotropic-nematic transition.

with α from equation A.15.

Figures 5.1 and 5.2 show phase diagrams for mixtures of rods with aspect ratios $L/D = 3$ and 5 and spheres. The solid lines are free volume theory predictions. The single phase, the isotropic mixture of rods and spheres, is marked "I". The region of the phase diagram, where the gas-like and liquid-like isotropic phases coexist is named "I+I". The two almost vertical lines are theoretical predictions for the phase boundaries of the isotropic-nematic transition [Tuinier *et al.* (2007)].

Since free volume theory is based upon a mean-field approximation and fluctuations, that are especially relevant near the critical point, are ignored, its predictions are expected to deviate from the simulation results there. Away from the critical point the predictions of the free volume theory approach the simulation results. As anticipated, the theory underestimates

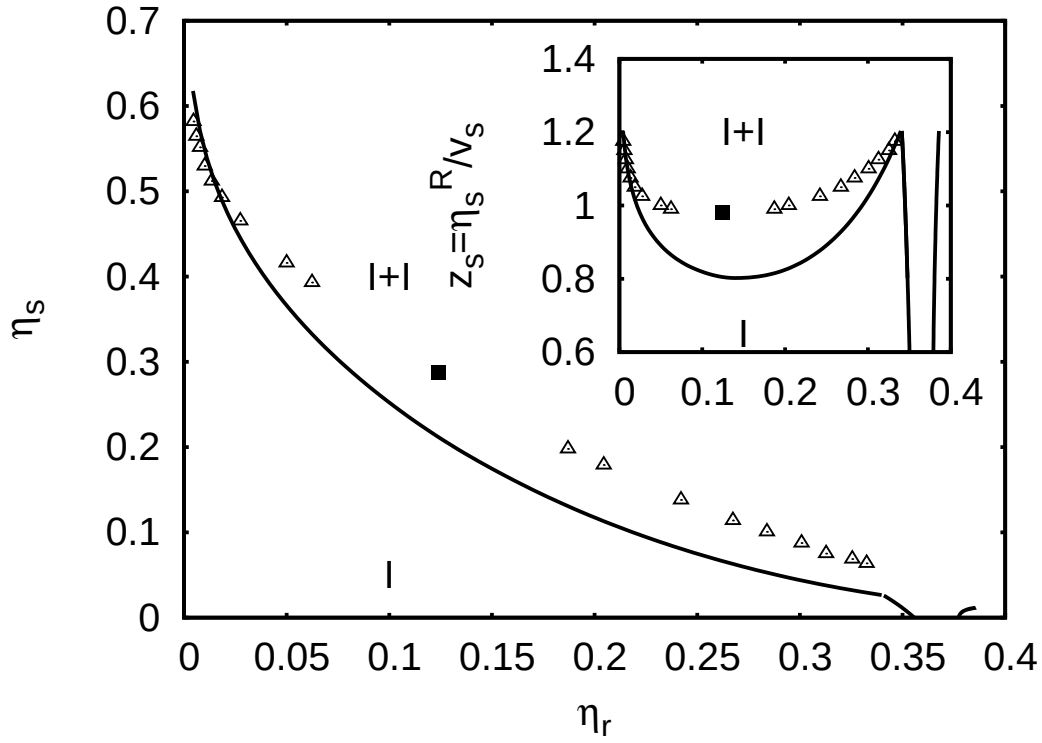

Figure 5.2: Bulk phase diagram for a mixture of spherocylinders with aspect ratio $L/D = 5$ and spheres of diameter D. The solid lines are predictions of the free volume theory, while the dotted lines are guides to the eyes. The filled square marks the critical point. The inset shows the phase diagram in the (z_s, η_r)-plane.The almost vertical lines in the inset indicate the coexistence region of the isotropic-nematic transition.

the volume fraction of spheres in the liquid phase considerably. This is due to the fact that the depletion forces change the local structure of the fluid as discussed in Chapter 4 – an effect which is not included in the calculations of the free volume accessible to spheres. On the gas-branch of the coexistence region, where the amount of rods is negligible, the theoretical predictions agree well with the simulation results.

Figure 5.3 shows a comparison of the presented results with the data obtained in previous computer simulations on the fluid-fluid separation by Bolhuis *et al.* [Bolhuis *et al.* (1997)] (open squares). The errorbars of their data are $\Delta\eta_r \sim 0.02$. Thus, the results do not coincide within the errorbars. The difference can be attributed to the small system sizes which were accessible at that time (1997). No estimate for the critical point could be obtained from their work [Bolhuis *et al.* (1997)].

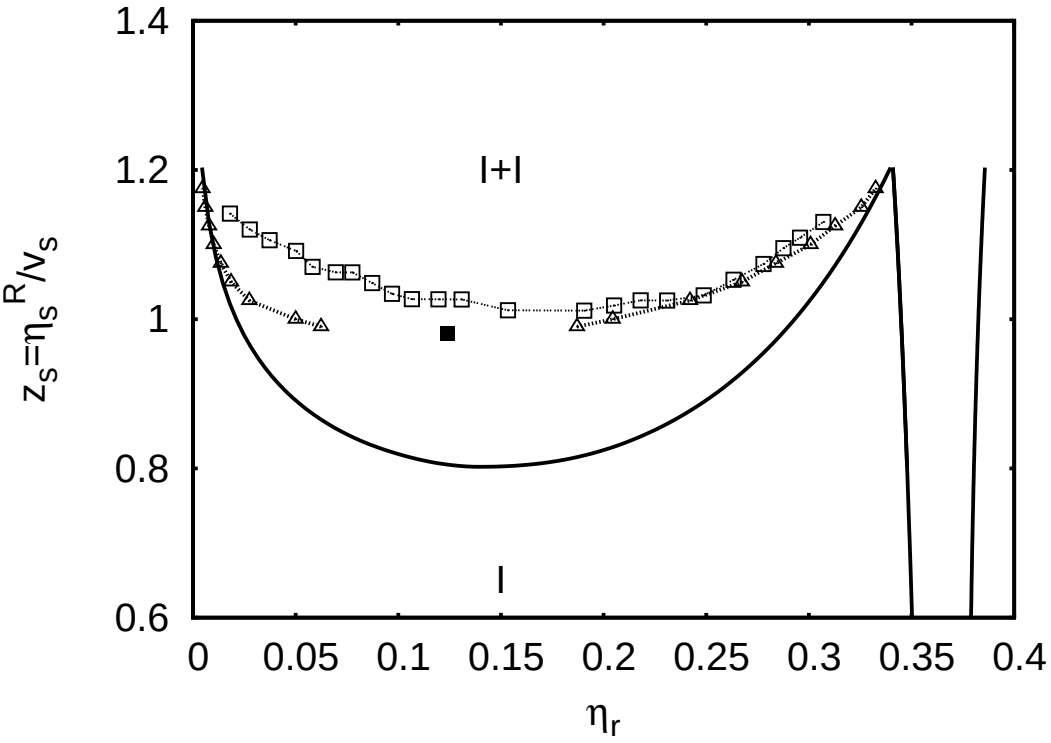

Figure 5.3: Comparison of the bulk phase diagram for a mixture of spherocylinders with aspect ratio $L/D = 5$ and spheres of diameter D to previous work. The open triangles are the results of the present work, the filled square marks the critical point. The open squares are the data obtained by Bolhuis *et al.* [Bolhuis *et al.* (1997)]. The solid lines are predictions of the free volume theory, while the dotted lines are guides to the eyes.

The results presented here are of high accuracy: the errorbars are smaller than the symbols. The main sources of error are finite size effects and insufficient sampling of the grand potential hypersurface perpendicular to the reaction coordinate (i.e., the packing fraction of rods). In order to check for the quality of sampling, the simulations were repeated for several different chemical potentials and different values of accuracy thresholds in the successive umbrella sampling. From this the error on the coexistence volume fractions can be estimated to be $\Delta\eta_r = \pm 0.002$. Finite size effects enter in two ways:

- At coexistence the system forms slab configurations with two interfaces (due to the periodic boundaries). If the simulation box dimension perpendicular to the interfaces, L_z, is too small, the interfaces interact. Away from the critical point, this contribution can

be ruled out by increasing L_z such that a plateau appears between the peaks in $P(\eta_r)$ (see Figure 3.3).

- $P(\eta_r)$ depends on the lateral box size, because the spectrum of capillary waves on the interfaces is cut off for wavelengths larger than the box. This effect is negligible far away from the critical point, too, because the interfacial tension there is large and the effects of capillary waves are very weak.

However, close to the critical point a finite size scaling analysis becomes necessary. In fact, the two effects are then just two aspects of the same property, the diverging correlation length. This issue is discussed further in section 5.3.

Close to the isotropic-nematic transition, the simulations cannot be equilibrated properly with the methods used here. For accurate grand canonical simulations of the isotropic-nematic transition more advanced biasing techniques are necessary [Frenkel and Smit (2002); Vink *et al.* (2005)]. Some of these techniques are presented in Appendix B, however, the computational effort needed to obtain reliable results is still too large to be carried out here.

5.3 Finite size scaling

As explained in the previous section, $P(\eta_r)$ depends on system size. This is, however, not a drawback but an advantage, because the finite size effects can be used in order to locate the critical point of isotropic-isotropic demixing. One can construct quantities which are independent of system size at the critical point. One possible choice [Landau and Binder (2000); Binder (1981)] of such a quantity is the cumulant ratio

$$U_4 = \frac{\langle m^4 \rangle}{\langle m^2 \rangle^2} \tag{5.3}$$

with

$$m = \eta_r - \langle \eta_r \rangle \tag{5.4}$$

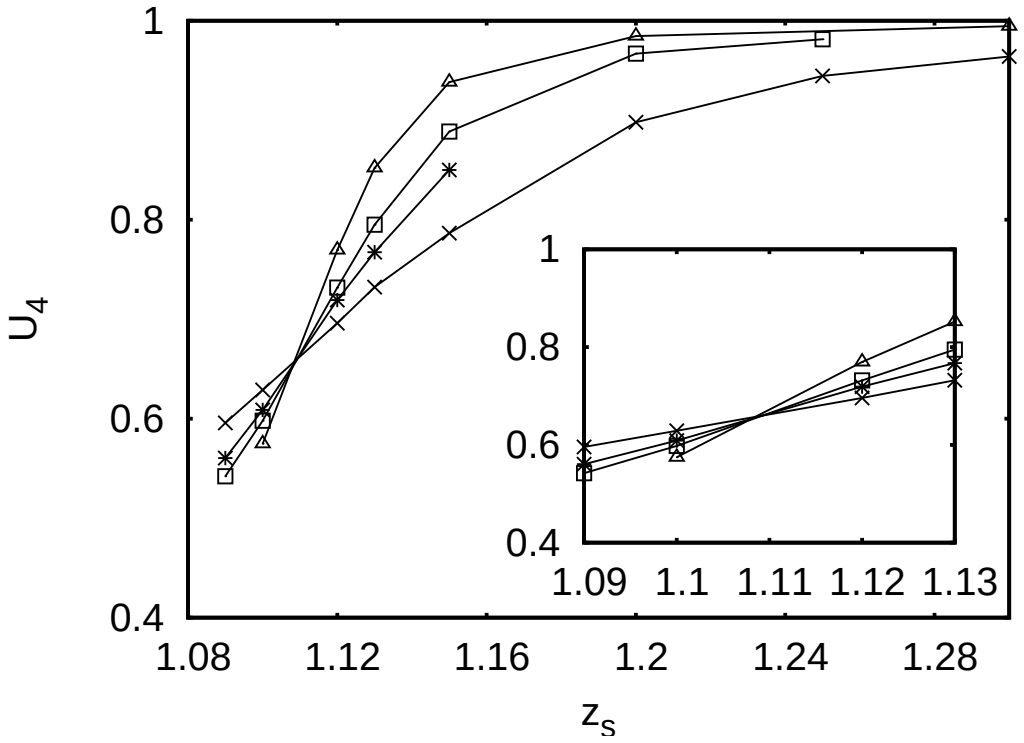

Figure 5.4: Cumulant ratio U_4 as a function of the sphere fugacity close to the critical point for box lengths $L_x = 9\ D$ (crosses), $12\ D$ (stars), $14\ D$ (squares) and $18\ D$ (triangles). Spherocylinders aspect ratio is $L/D = 3$. The inset shows a magnified plot of the region near the intersection point.

When U_4 is plotted versus z_s close to the critical point for different system sizes, the intersection point marks the critical point. Figure 5.4 shows that the critical sphere fugacity for spherocylinders with aspect ratio $L/D = 3$ is $z_s^c = 1.109 \pm 0.001$. For comparison, another cumulant ratio

$$U_2 = \frac{\langle m^2 \rangle}{\langle m \rangle^2} \tag{5.5}$$

is also plotted in Figure 5.5. The intersection points of both cumulant ratios coincide, yielding the same value for the critical point. (If this check would not work out, it would be an indication that the box lengths L_x are still too small, and the asymptotic region where the finite size scaling holds, has not been reached: in principle, one should consider the limit $L_x \to \infty$!)

The coexistence diameter δ can be defined as the average of the volume

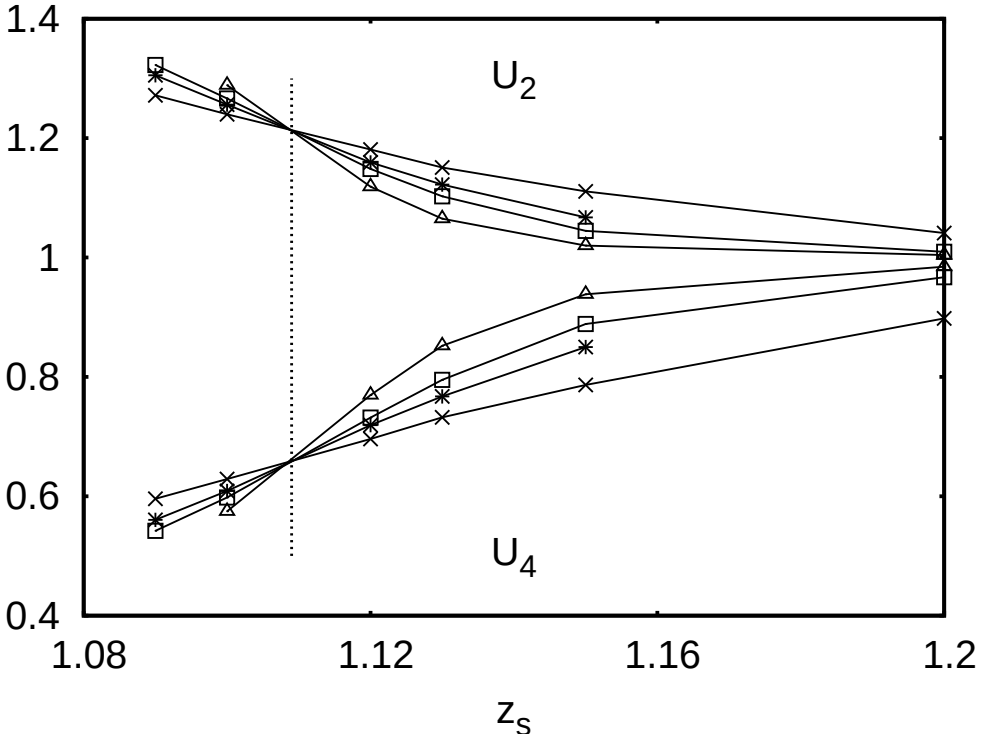

Figure 5.5: Cumulant ratios U_2 and U_4 as a function of the sphere fugacity close to the critical point for box lengths $L_x = 9\ D$ (crosses), $12\ D$ (stars), $14\ D$ (squares) and $18\ D$ (triangles). Spherocylinders aspect ratio is $L/D = 3$.

fractions of the coexisting rod-rich and rod-poor phases

$$\delta = \frac{\eta_r^l + \eta_r^g}{2} \tag{5.6}$$

On the approach to the critical point there are corrections due to the finite size of the system [Vink and Wensink (2006); Vink *et al.* (2006b)]. However, in the first approximation the value of the coexistence diameter at critical sphere fugacity can be considered as the critical rod volume fraction η_r^c.

For each volume fraction of rods, the volume fraction of spheres present in the system was measured and averaged over the number of times this rod volume fraction occurred. Figure 5.6 shows the values obtained by simulating a system of rods with $L/D = 3$ at sphere fugacity $z_s = 1.15$. The critical sphere volume fraction is the one which corresponds to the critical rod volume fraction and was measured at the critical sphere fugacity. The position of the critical point was derived after simulating the system, thus, the value of the critical sphere fugacity was not known beforehand. If no

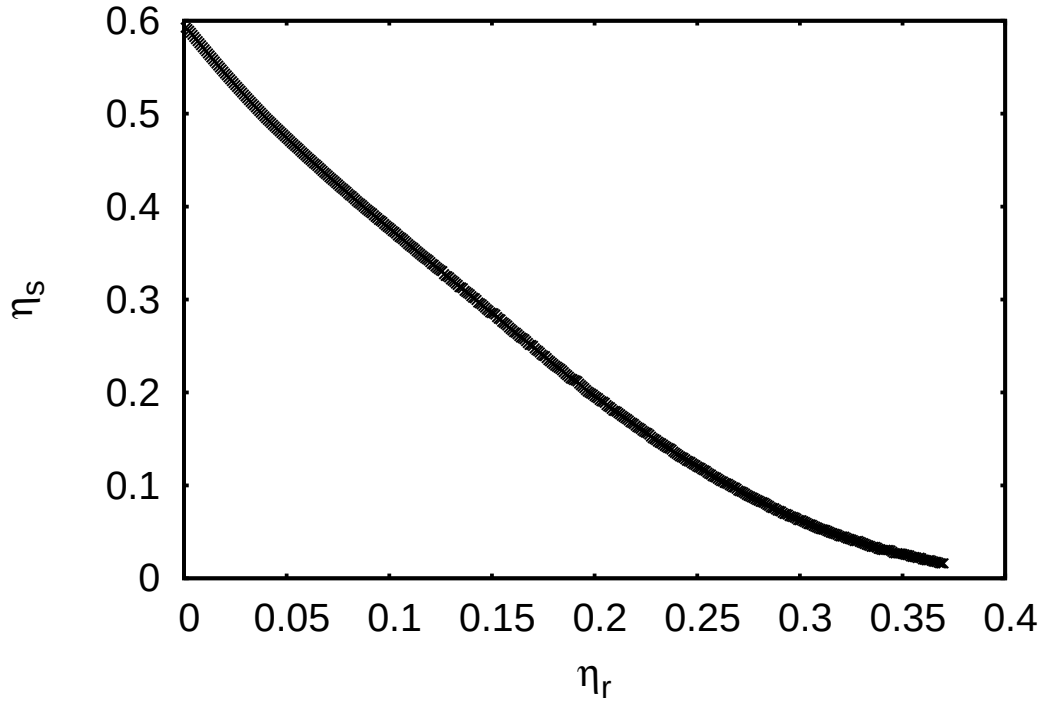

Figure 5.6: Volume fraction of spheres present in the mixture as a function of rod volume fraction for rods with aspect ratio $L/D = 3$ at sphere fugacity $z_s = 1.15$.

simulation runs were available at the critical sphere fugacity, the sphere volume fractions from the results of the simulations with the closest values of the fugacity were used to bracket the range in which the required critical sphere volume fraction lies.

Figure 5.7 shows the difference in packing fraction $\eta_r^l - \eta_r^g$ versus the "relative distance from the critical point" $z_s/z_s^c - 1$ (circles for $L/D = 3$ and diamonds for $L/D = 5$). The upper line in the graph is proportional to $(z_s/z_s^c - 1)^{\beta_{\text{Ising}}}$, where $\beta_{\text{Ising}} = 0.326$ is the critical exponent of the order parameter in the Ising model. Clearly, the critical point is of the Ising universality class. The almost perfect superposition of the data for $L/D = 3$ and $L/D = 5$ indicate that the critical amplitudes of the order parameter depend on the rod aspect ratio only very weakly. For $z_s/z_s^c - 1 \geq 0.2$ systematic deviations from the power law occur, as expected, since these data are too far from criticality.

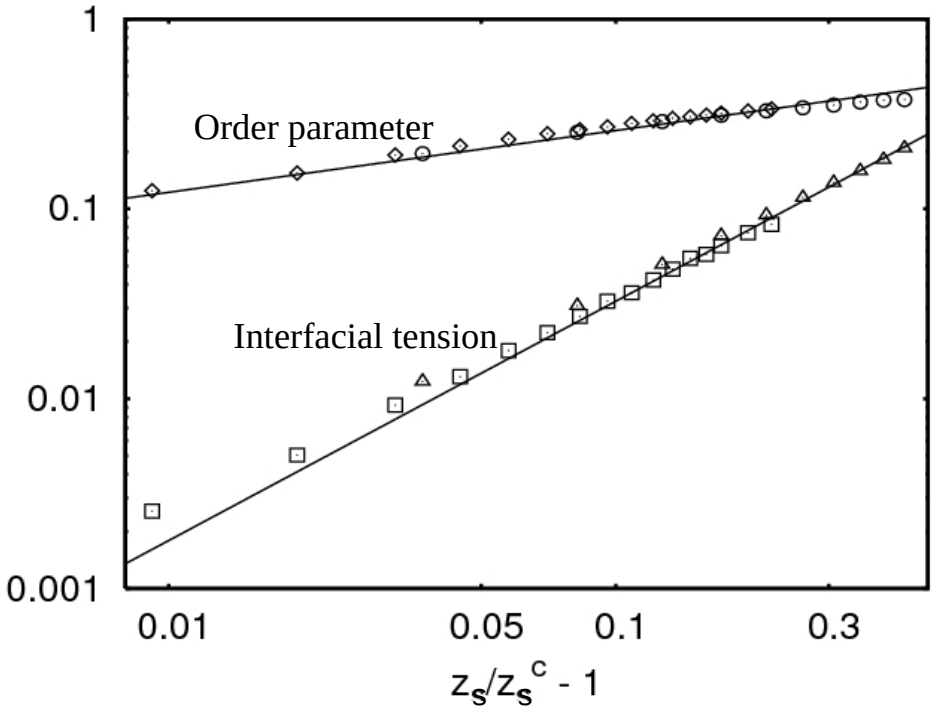

Figure 5.7: Order parameter ($\eta_r^l - \eta_r^g$) (circles and diamonds) and interfacial tension γ (triangles and squares) versus "relative distance from the critical point" $z_s/z_s^c - 1$. Spherocylinder aspect ratios are $L/D = 3$ (triangles and circles) and 5 (squares and diamonds). The solid lines correspond to the Ising power-law-behaviour with exponents $\beta_{\text{Ising}} = 0.326$ and $2\nu_{\text{Ising}} = 1.26$.

5.4 Interfacial tension

In the transition region where the gas-like phase transforms into the liquid-like phase and vice-versa, a free energy barrier $\Delta\Omega$ needs to be crossed (indicated in figure 3.4). Since the two phases have the same energy at coexistence, the barrier is due to the energy needed to create an interface between two phases. $\Delta\Omega$ is related to the interfacial tension via

$$\gamma \equiv \lim_{L_x \to \infty} \frac{\Delta\Omega}{2L_x^2} \tag{5.7}$$

where L_x^2 is the area of the interface and the factor $1/2$ accounts for the two interfaces, which are present due to the periodic boundary conditions [Binder (1982)]. In an elongated simulation box the interfaces are preferably formed perpendicular to the longer box side, since the area of such an interface is smaller than in the other directions and the energy barrier,

which needs to be crossed, is lower.

Figure 5.7 shows values of the interfacial tension as a function of the "relative distance from the critical point" $z_s/z_s^c - 1$ (triangles for $L/D = 3$ and squares for $L/D = 5$) on the logarithmic scale. The lower line in the graph indicates $(z_s/z_s^c - 1)^{2\nu_{\text{Ising}}}$, where $2\nu_{\text{Ising}} = 1.26$ is the critical exponent for the interfacial tension in the three dimensional Ising model. The systematic deviations from the straight line for small distances from the critical point are presumably due to the finite size effects.

5.5 Summary

The isotropic-isotropic demixing of a suspension of hard spherocylinders of two aspect ratios $L/D = 3, 5$ and ideal spheres in the bulk was studied in the grand canonical ensemble. In order to access states of high free energy, the successive umbrella sampling method [Virnau and Müller (2004)] was used to obtain the probability distribution of finding a rod volume fraction. The critical point was extracted from an analysis of the cumulants of this distribution.

The interfacial tension between the gas- and liquid-like phase can be estimated from the free energy profile.

Free volume theory [Lekkerkerker and Stroobants (1994)] works well for the gas branch of the coexistence curve away from the critical point, but, as expected, being a mean-field approximation, underestimates the concentrations at the critical point. On the liquid branch, the theory underestimates the rod volume fraction considerably. This is due to the depletion induced changes in the local structure of the fluid, which are not accounted for in the theory.

The mixture of hard spherocylinders and ideal spheres resembles the Asakura-Oosawa-Vrij model of spherical colloids with depletant, in particular, its behaviour on approach to the critical point falls into the Ising universality class. The length of the spherocylinders does not influence the critical behaviour of the mixture, as expected.

Chapter 6

Confinement

6.1 Introduction

The bulk phase diagram was presented in the previous chapter. The behaviour of the system changes if the mixture is confined into a slit-pore. Recently, there was a lot of experimental interest in the non-equilibrium states of the colloid-polymer suspensions, in particular, in the effect of shear [Kang *et al.* (2006); Dhont *et al.* (2003); Lenstra *et al.* (2001); Lettinga and Dhont (2004)]. Thus, it would be of importance to study first the effects of confinement in equilibrium, before applying shear to the system.

In confinement, orientational order is induced by the walls. This order affects the phase transitions and the critical behaviour of the system. Understanding these effects is interesting from the point of view of critical phenomena, as well as a prerequisite for applications of liquid crystals in microfluidic devices.

Several related issues have recently been addressed by other groups. Dijkstra, van Roij and Evans studied suspensions of hard rods in confinement between hard walls close to the isotropic-nematic transition in Gibbs ensemble simulations [Dijkstra *et al.* (2001)] and within the Zwanzig model [van Roij *et al.* (2000a,b)]. They found that a uniaxial surface phase forms at low concentrations. At higher concentrations the surface film undergoes a transition to biaxial order, and on further approach of the isotropic-nematic transition, its thickness diverges.

The nematic wetting behaviour on the approach of the isotropic-nematic

transition [Hsiung *et al.* (1986); Chen *et al.* (1989)], as well as the dependence of the isotropic-nematic transition on the surface anchoring [Boamfa *et al.* (2003)] were studied experimentally in various commercial liquid crystal mixtures.

Rods in two dimensions – i.e. the limiting case of an infinitely thin confining slit-pore – have been studied with emphasis on several aspects of orientational order [Bates and Frenkel (2000); Lagomarsino *et al.* (2003); Donev *et al.* (2006); Vink (2007); Martínez-Ratón (2007)].

Sphere-sphere mixtures in confinement have been simulated by Gibbs ensemble Monte Carlo [Fortini *et al.* (2006)] and with the successive umbrella sampling method [Vink *et al.* (2006a,b); De Virgiliis *et al.* (2007); Fortini *et al.* (2008)]. In particular, in the studies by Vink *et al.* the crossover from $3dim$ to $2dim$ critical behaviour was investigated. In colloidal sphere-sphere mixture the contact angle of the gas-liquid interface with a hard wall was calculated via density functional theory [Wessels *et al.* (2004)].

For colloidal rod-like particles theory [Sear (1998)] predicts adsorption of rods to a hard wall due to depletion interactions. One monolayer is expected to be formed at the wall. Here, mixtures of hard spherocylinders and freely interpenetrable spheres confined to hard-walled slit-pores are studied. By means of Monte Carlo simulation in the grand canonical ensemble and by finite size scaling analysis, the phase boundaries of isotropic-isotropic coexistence in confinement are determined. In particular, a method by which the contact angle of a droplet in contact with a wall can be determined from simulations in the grand canonical ensemble is presented.

6.2 Phase diagrams

The behaviour of the mixture of rods and spheres confined between two hard walls at distance d is considered.

Figure 6.1 shows the phase diagram obtained for rods of aspect ratio $L/D = 3$ at wall separations $d = 3\ D$ (squares), $6\ D$ (circles), $9\ D$ (triangles) and $15\ D$ (diamonds) and in the bulk (crosses). The phase boundaries are indicated. The smaller the distance between the walls, the larger is the

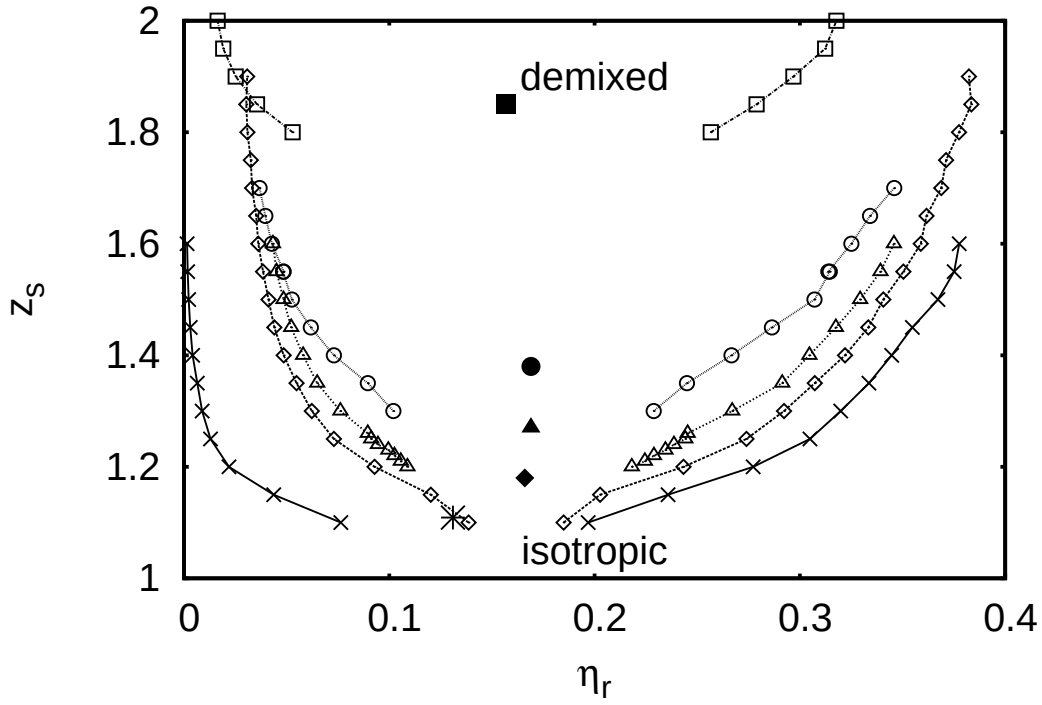

Figure 6.1: Phase diagram for a mixture of spherocylinders with aspect ratio $L/D = 3$ and spheres of diameter D in bulk (crosses) and between two hard walls at distance $d = 3\ D$ (squares), $6\ D$ (circles), $9\ D$ (triangles) and $15\ D$ (diamonds). The filled symbols mark the critical points. Curves are guides to the eye only, connecting data for the rod volume fractions of the coexisting phases rich (right) and poor (left) in rods, for systems of lateral linear dimensions $L_x = 12\ D$ for $d = 6, 9\ D$ and $L_x = 18\ D$ for $d = 3, 15\ D$.

sphere fugacity which is required for demixing. Also the chemical potential of the rods at coexistence is higher than in the bulk and increases on the decrease of the wall separation. The critical point was estimated similarly as was done in the bulk, see section 6.4.

Table 6.1 sums up the positions of the critical point at various wall distances. When the system is confined, the critical point lies at a higher rod volume fraction than in the bulk. However, once in confinement, the shift in the critical rod volume fraction in comparison to the bulk is almost the same for all wall separations, as long as the distance between the walls is large enough for the correlations, which are induced by the walls, to decay before the centre of the pore is reached.

The data for the critical volume fractions thus indicate a non-monotonic

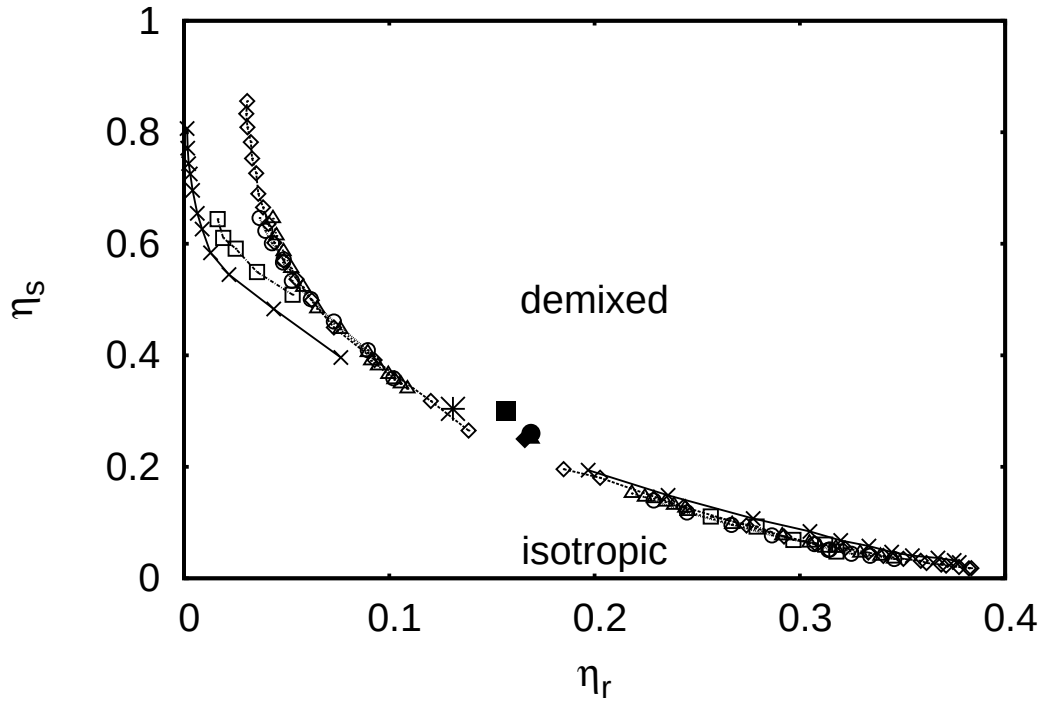

Figure 6.2: Phase diagram of Figure 6.1 in the (η_r, η_s) plane.

variation when the distance between the walls increases, and the asymptotic region of large d/D, where the critical volume fractions of rods and spheres converge towards their bulk values has not been reached. Also, see section 6.4 for an attempt to study the crossover $3dim \rightarrow 2dim$ of the critical behaviour. It is expected to be similar to an analogous behaviour in the standard Asacura-Oosawa-Vrij model of spherical colloids.

Table 6.1: Critical point in confinement.

d/D	$z^c_{s,\mathrm{conf}}$	$\eta^c_{r,\mathrm{conf}}$	$\eta^c_{s,\mathrm{conf}}$	$\mu^c_{r,\mathrm{conf}}$
3	1.85 ± 0.03	0.157 ± 0.002	0.30 ± 0.01	10.1 ± 0.2
4	1.59 ± 0.02	0.164 ± 0.002	0.29 ± 0.01	8.9 ± 0.1
5	1.48 ± 0.02	0.169 ± 0.002	0.27 ± 0.01	8.5 ± 0.1
6	1.38 ± 0.02	0.169 ± 0.002	0.26 ± 0.01	8.0 ± 0.1
9	1.26 ± 0.01	0.169 ± 0.002	0.25 ± 0.01	7.35 ± 0.05
12	1.22 ± 0.01	0.169 ± 0.002	0.25 ± 0.01	7.04 ± 0.05
15	1.18 ± 0.01	0.166 ± 0.002	0.25 ± 0.01	6.74 ± 0.05
∞	1.109 ± 0.001	0.131 ± 0.002	0.30 ± 0.01	6.208 ± 0.005

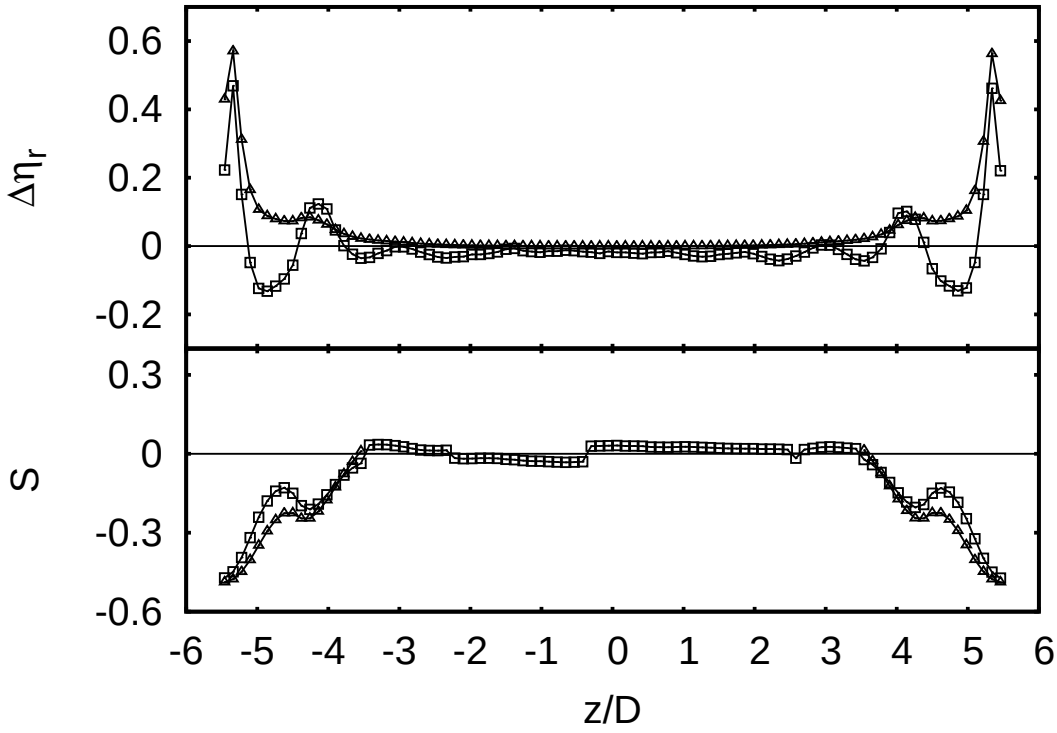

Figure 6.3: Confinement induced difference in the volume fraction of rods $\Delta\eta_r = \eta_r^{\mathrm{conf}} - \eta_r^{\mathrm{bulk}}$ in the gas- (open triangles) and liquid-like (open squares) phases (top). Nematic order parameter S in the gas-like (open triangles) phase at the walls and in liquid-like (open squares) phase (bottom). The distance between the walls is $d = 12\ D$, rod aspect ratio $L/D = 3$. Corresponding sphere fugacity is $z_s = 1.4$. These data refer to a lateral linear dimension $L_x = 24\ D$.

To study structural changes due to the interaction of the rods with the walls the gas-like and liquid-like phases were simulated under confinement in the canonical ensemble (fixed number of spherocylinders N_r, spheres N_s as well as the volume of the simulation box). The number of particles was chosen to match the coexistence values determined in the grand canonical ensemble. Although in principle the finite size effects are different in the canonical and grand canonical ensemble [Landau and Binder (2000)], far enough from the critical point this difference can safely be neglected.

Figure 6.3 shows profiles of the nematic order parameter (bottom) and of the rod volume fraction changes in the gas-like and liquid-like phases due to the walls. The biaxiality parameter ξ (not shown here) fluctuates around zero in both phases. The nematic order parameter of the gas-like phase in

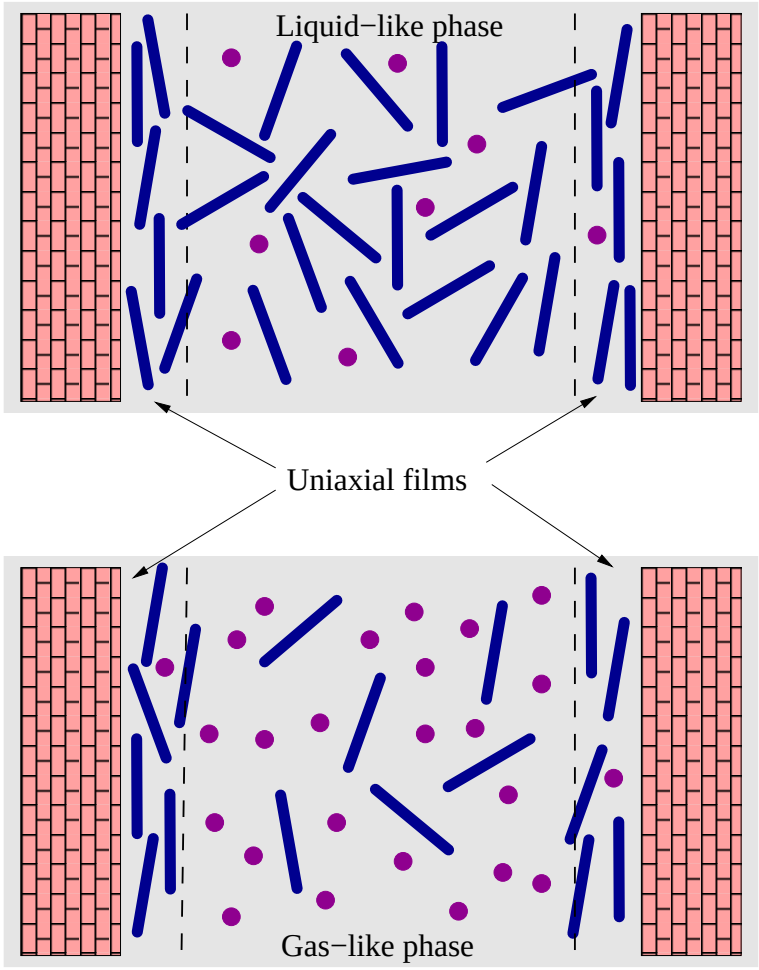

Figure 6.4: Sketches of configurations in confinement. Close to the walls, the system forms a uniaxial film, further away it behaves as in the bulk liquid-like (upper panel) or bulk gas-like (lower panel) phases.

the middle of the box is not shown here, since the number of rods from which this parameter has to be calculated is very small and statistics were extremely poor. Although longer simulation runs and larger system sizes would yield a better estimate for the nematic order parameter, the effort is redundant, since a simple look at the snapshots gives a convincing evidence that the considered phase is an isotropic gas. In the more important area close to the walls the sampling of the nematic order parameter works well, since the number of rods is sufficient to get reliable results.

The hard walls induce a layered uniaxial phase (see sketch in Figure 6.4), whose thickness is of the order of the rod length. The phases between these two uniaxial films have the same properties as the usual bulk gas- and

liquid-like phases. Hence, confinement shifts the phase diagram in terms of the rod volume fraction such that the uniaxial layered films are introduced to the system.

The gas-like phase is moved to larger rod volume fractions since the density of the uniaxial film is larger than it is in the bulk gas-like phase. The adsorption of spherocylinders onto the hard wall in the sphere-rich phase was predicted theoretically [Sear (1998)]. However, the layering of the film is not included in the theory.

The density of the uniaxial film in the liquid-like phase is smaller than in the bulk due to the layering effects as can be seen in Figure 6.3, upper panel. Thus, the liquid-like branch is shifted to smaller volume fractions. Unlike in the gas-phase, the amount of spheres in the liquid-like phase is comparably small, thus, the depletion effect seen here is the entropically driven repulsion between a hard spherocylinder and a hard wall. On the approach of the wall, the number orientations a rod is allowed to take becomes restricted, and, to maximise the orientational entropy, the particles are driven from the wall.

As long as the uniaxial layers on the walls do not interact, these changes do not depend on the distance between the walls. Once the layers start to interact – roughly at $d < 2\ L$ – the separation distance d becomes important. Gas-liquid demixing then occurs laterally inside the layers.

In terms of the sphere fugacities, the phase diagram is continuously shifted to higher values. However, if one considers the actual volume fraction of spheres in the mixture instead of their chemical potential, the phase diagram remains almost unchanged by confinement, as indicated in Figure 6.2, provided the demixing transition occurs in the bulk-like central region and not in the uniaxial layers at the walls. The shift in the fugacities is due to the reduced volume which is available between the uniaxial films. At decreasing wall separation the free volume accessible to spheres between the uniaxial layers of rods becomes smaller, therefore the chemical potential needed to keep the spheres in equilibrium with the rods increases. The sphere volume fraction in the system stays constant as long as the rod volume fraction of the stable phase does not change due to moving the

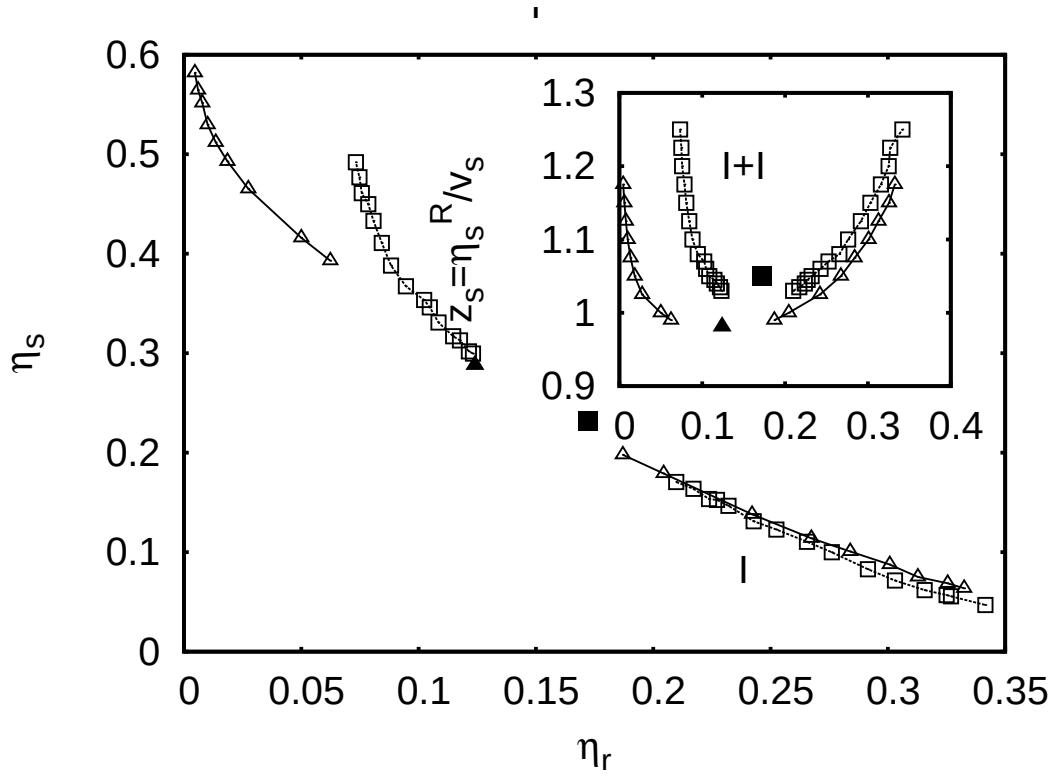

Figure 6.5: Phase diagram for a mixture of spherocylinders with aspect ratio $L/D = 5$ and spheres of diameter D between two hard walls at distance $d = 15\ D$ (squares) compared to the bulk values (triangles). The filled symbols mark the critical points. The inset shows the phase diagram in the (z_s, η_r)-plane. The symbols show "raw data" for one box dimension $L_x = 20\ D$ only, and thus the curves marking the peaks of $P(\eta_r)$ do not join at the critical points ("finite size tails" [Landau and Binder (2000)]). The lines are guides to the eyes.

walls.

6.2.1 Aspect ratio

Figure 6.5 shows the phase diagram for rod aspect ratio $L/D = 5$. The distance between the walls is $d = 15\ D$.

Table 6.2: Critical point in the bulk and in confinement to slit-pore of width $d/D = 3L/D$.

L/D	$z^c_{s,\mathrm{conf}}$	$\eta^c_{r,\mathrm{conf}}$	$z^c_{s,\mathrm{bulk}}$	$\eta^c_{r,\mathrm{bulk}}$
3	1.26 ± 0.01	0.168 ± 0.002	1.109 ± 0.001	0.131 ± 0.002
5	1.05 ± 0.01	0.172 ± 0.002	0.981 ± 0.001	0.124 ± 0.002

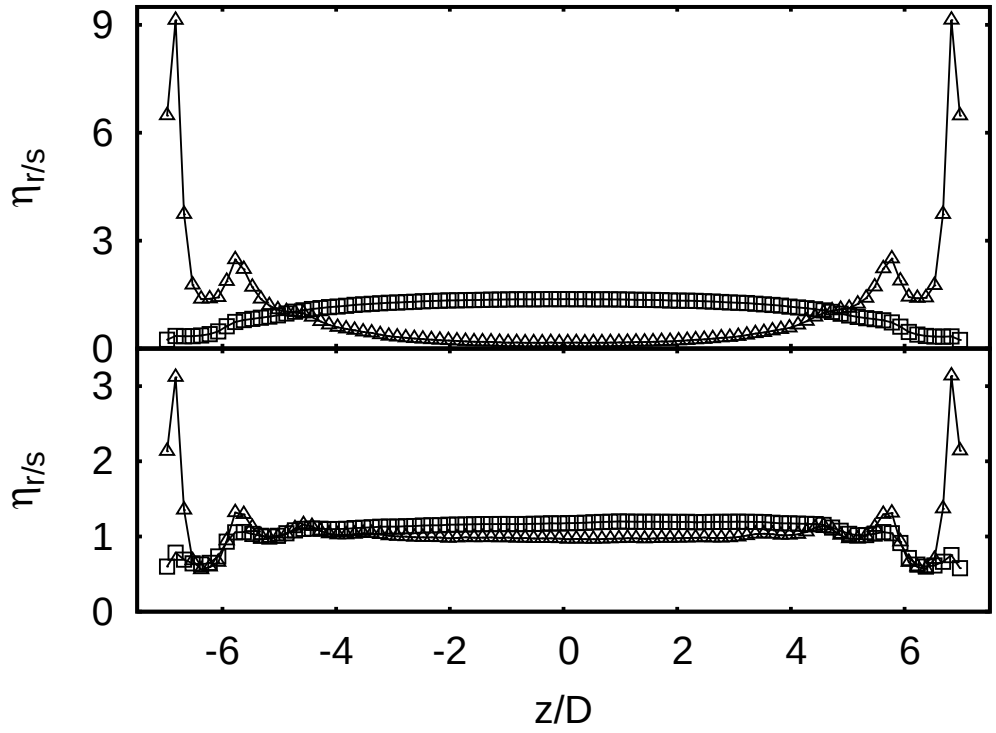

Figure 6.6: Density profiles of rods (triangles) and spheres (squares) normalised by their overall densities in the gas-like (top frame) and in the liquid-like (bottom frame) phases between two hard walls at distance $d/D = 3L/D$. Aspect ratio $L/D = 5$. Corresponding sphere fugacity is $z_s = 1.1$.

Table 6.2 lists the position of the critical points for mixtures of rods with two aspect ratios confined into slit-pores of the same width in terms of the rod length in comparison to the bulk results. The relative shift in η_r^c, which is observed for rods with aspect ratio $L/D = 5$, is larger than the one of rods with aspect ratio $L/D = 3$, though the relative shift in z_s^c behaves the other way around. The second effect is due to the ordering of the spheres close to the walls. Thus, its relative decrease on increase of the rods' aspect ratio is plausible, since, in terms of the sphere diameter, the distance between the walls increases.

Figure 6.6 shows the density profiles of rods with aspect ratio $L/D = 5$ and spheres between walls at a distance $d/D = 3L/D$ in the gas-like (top frame) and in the corresponding liquid-like (bottom frame) phases at coexistence. The overall densities are approximately the positions of the peaks of the probability distribution $P(\eta_r)$ from the grand canonical

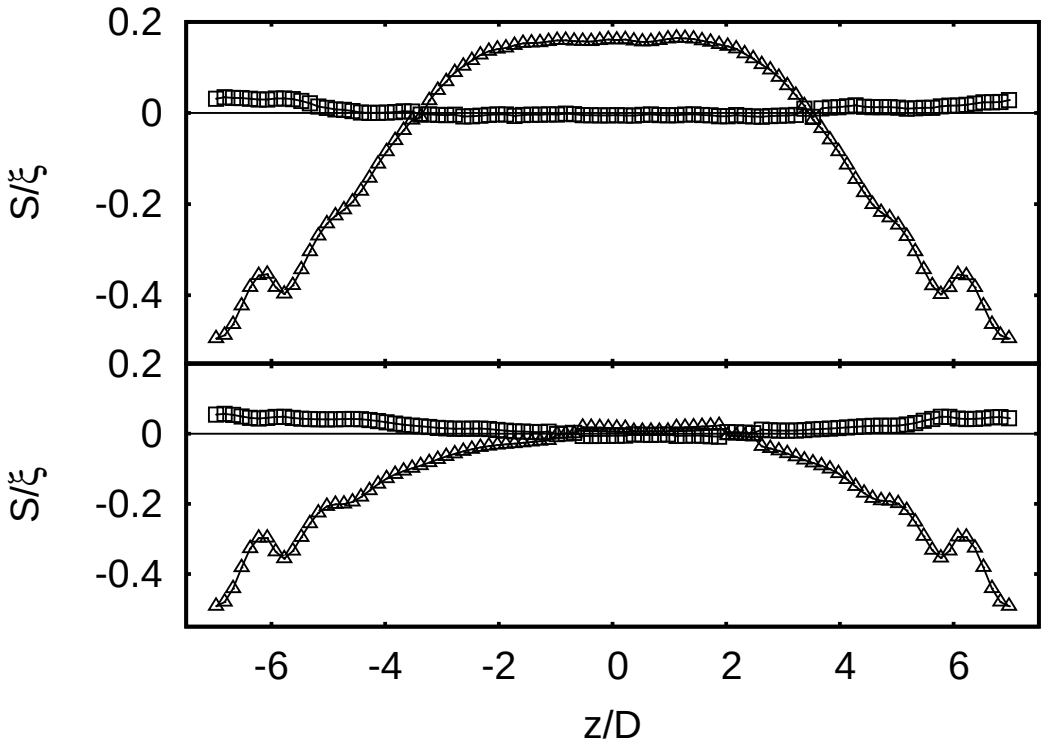

Figure 6.7: Nematic order S (triangles) and biaxiality ξ (squares) parameter profiles in the gas-like (top frame) and in the liquid-like (bottom frame) phases between two hard walls at distance $d/D = 3L/D$. Aspect ratio $L/D = 5$. Corresponding sphere fugacity is $z_s = 1.1$.

simulation at sphere fugacity $z_s = 1.1$.

Figure 6.7 shows the corresponding profiles of the nematic order parameter S and of the biaxiality parameter ξ in the gas-like (top frame) and in the liquid-like (bottom frame) phases.

The positional as well as the orientational order of rods are clearly visible in the liquid- as well as in the gas-like phase. The range of the induced effects is of the order of the rod length, just as for the rods of smaller aspect ratio. In the middle of the system the order parameters reach their bulk values. The spheres are pushed away from the walls. The range of this effect is also of the order of the rod length in both phases.

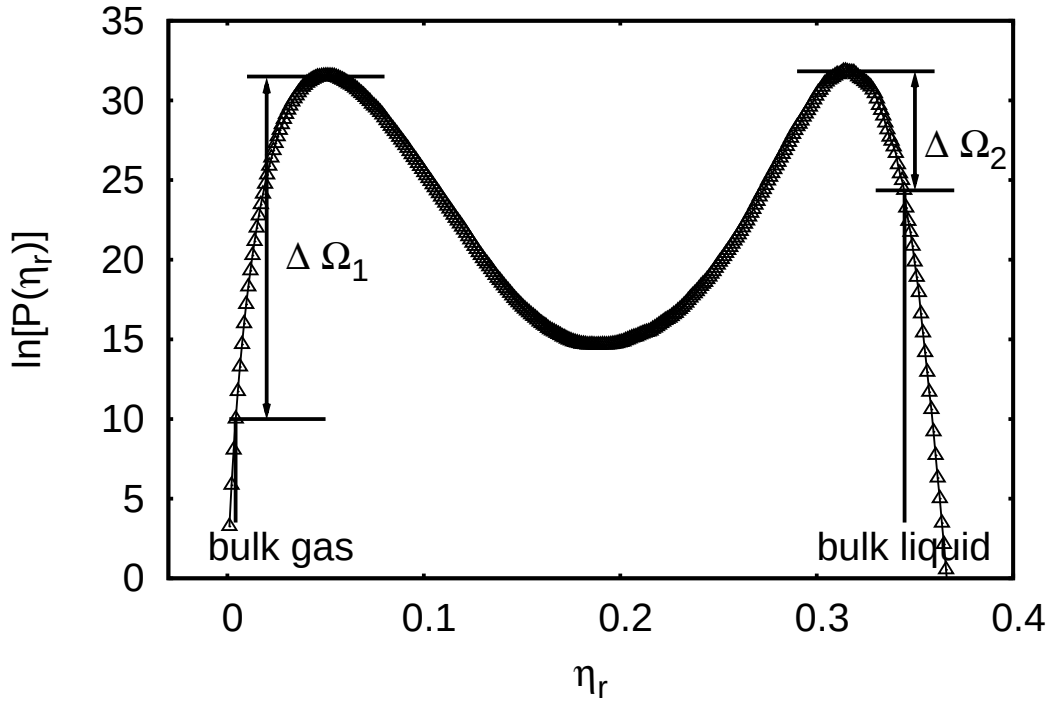

Figure 6.8: Grand potential $\ln[P(\eta_r)]$ for spherocylinders between the walls at distance $d = 12\ D$ and sphere fugacity $z_s = 1.4$. $\Delta\Omega_1$ and $\Delta\Omega_2$ indicate the energy differences between the states stable in the bulk and in confinement on the gas-like and on the liquid-like side of the phase diagram.

6.3 Wetting behaviour

From the successive umbrella sampling simulations a distribution $P(\eta_r)$ is obtained. Its logarithm corresponds (up to a constant) to the grand potential as a functional of the rod volume fraction. Thus, the differences in the free energy of various states can be extracted from this distribution. Consider the gas-like phase. The rod volume fraction which would be stable in the bulk at a fixed sphere fugacity is known from simulations described in Chapter 5.

Now, the free energy difference between this value and the value of the gas-like phase stable in confinement, $\Delta\Omega_1$, can be read off the grand potential distribution, as indicated in Figure 6.8. This difference is the energy needed to create the interfaces of the bulk-like gas phase (g) with the walls (w).

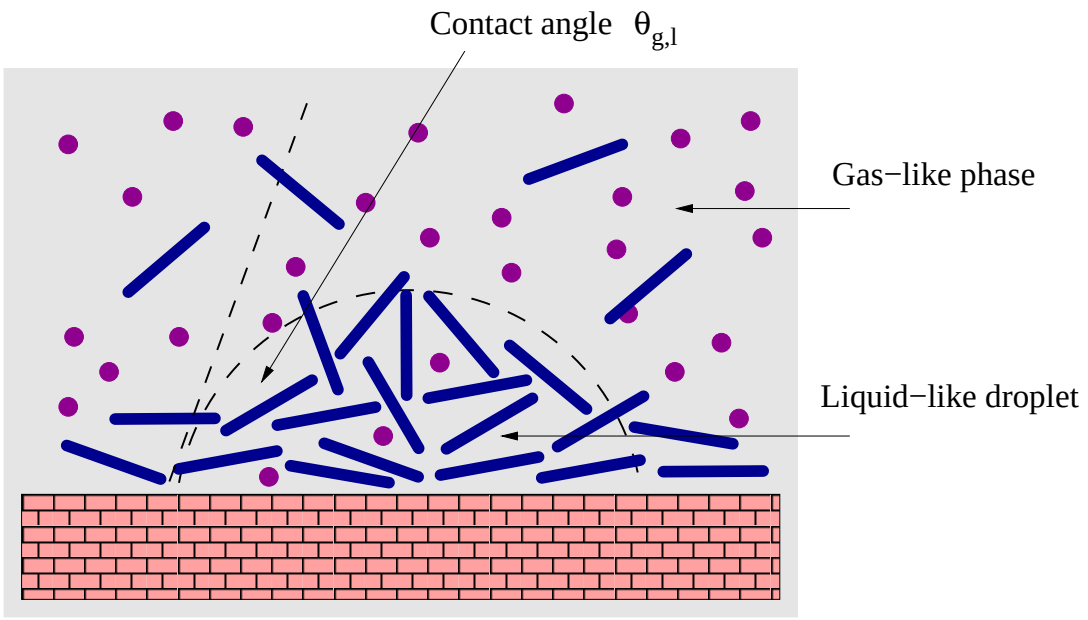

Figure 6.9: Sketch of contact angle.

The corresponding interfacial tension $\gamma_{g,w}$ can be calculated as

$$\gamma_{g,w} = \frac{\Delta\Omega_1}{2A} \tag{6.1}$$

with A the area of one wall. Similarly, the interfacial tension between the liquid-like phase (l) and the wall can be determined

$$\gamma_{l,w} = \frac{\Delta\Omega_2}{2A} \tag{6.2}$$

with $\Delta\Omega_2$ the free energy difference between the liquid-like branch in the rod volume fraction in bulk and in confinement.

Assume the liquid-like phase forms a droplet on the wall as sketched in Figure 6.9. According to Young's law, the contact angle $\theta_{g,l}$ is determined by

$$\cos\theta_{g,l} = \frac{\gamma_{g,w} - \gamma_{l,w}}{\gamma_{g,l}} \tag{6.3}$$

The interfacial tension between the gas- and the liquid-like phase in bulk was calculated in Chapter 5, the interfacial tension difference on the right-hand side of the equation can be obtained by subtracting equation 6.2 from equation 6.1. Thus, everything needed to determine the contact angle is known.

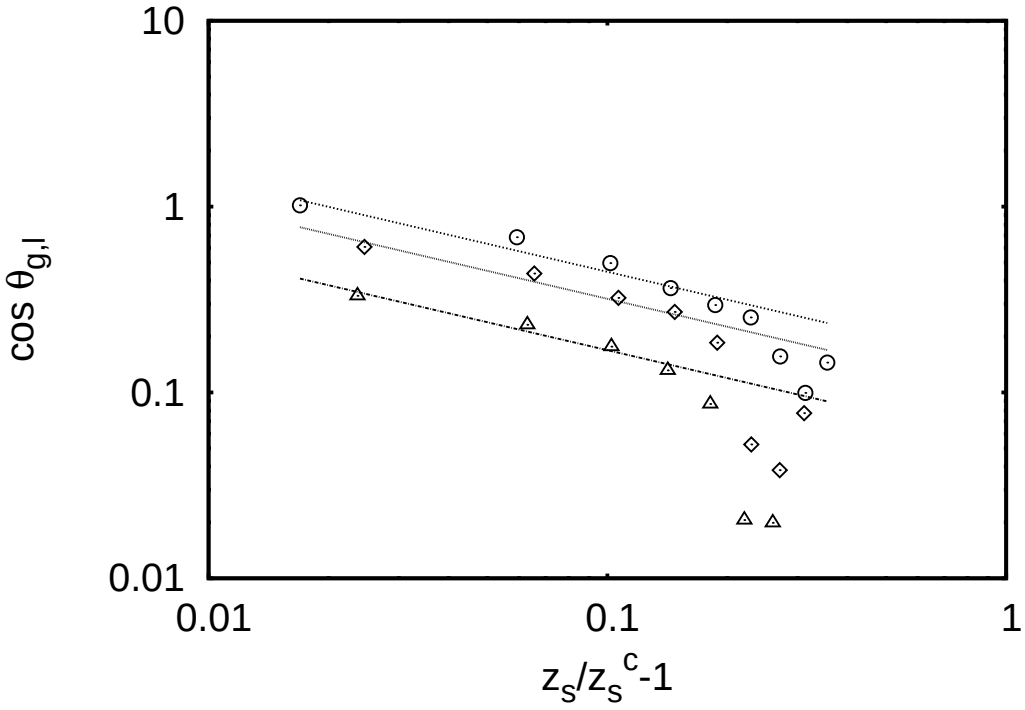

Figure 6.10: $\cos\theta_{g,l}$ as a function of the distance from the critical point for wall separations $d = 9\ D$ (squares), $12\ D$ (diamonds) and $15\ D$ (circles). The slope of the lines is -0.5 (they are not fitted).

Figure 6.10 shows the cosine of the contact angle obtained in this way at wall separations $d = 9, 12, 15\ D$. On approach of the critical point the ratio $(\gamma_{g,w} - \gamma_{l,w})/\gamma_{g,l}$ is expected to show power law behaviour [Dietrich (1988)] with the exponent

$$\beta_1 - \mu \approx -0.5 \tag{6.4}$$

where $\beta_1 \approx 0.8$ is the surface critical exponent [Binder and Hohenberg (1972, 1974); Diehl (1986)] and $\mu \approx 1.3$ is the gas-liquid interfacial tension exponent. The lines in Figure 6.10 indicate the predicted power law. Since $\cos\theta_{g,l}$ cannot exceed unity, the point where this ratio reaches unity determines the value of z_s at which (for $d \to \infty$) the wetting transition occurs.

6.4 Finite size scaling

Figure 6.11 shows the behaviour of the fourth order cumulant ratio

$$U_4 = \frac{\langle m^4 \rangle}{\langle m^2 \rangle^2} \tag{6.5}$$

which is defined in Chapter 5 and can be used to calculate the position of the critical point in confinement. The value of the intersection point for different system sizes is also an indicator of the universality class of the considered system [Binder (1981)]. Here, on the increase of confinement, a crossover from the $3dim$ to the $2dim$ Ising universality class is expected. Indeed, the drift in the value of the intersection point of U_4 plotted for different system sizes is clearly visible – from the $3dim$ Ising value $U_4 \approx 0.629$ toward the $2dim$ Ising value of $U_4 \approx 0.856$ in confinement.

A very thorough cumulant analysis was presented by Vink *et al.* [Vink *et al.* (2006a)] for a mixture of colloidal spheres and ideal polymer coils confined between two hard walls. They mentioned, that for any wall separation the intersection point actually lies directly at the $2dim$ universality value, but only if the system is truly infinite in the directions parallel to the walls. The intermediate crossing points obtained here are due to the finite size of the simulation box. The shift presented in Figure 6.11 can be explained by the fact that the ratio between the dimensions of the plates and of the distance between them becomes larger on decreasing the separation. Thus, the system becomes 'larger', however, it is still not large enough to obtain the $2dim$ universality value. The computational effort of simulating systems resembling the true $2dim$ infinite behaviour very soon becomes too big to be carried out here.

6.5 Summary

In this chapter computer simulation studies of suspensions of rods and depleting spheres under confinement to a slit-pore were presented. In confinement, the critical point is shifted to higher volume fractions of rods as compared to the bulk, because uniaxially ordered surface layers form close

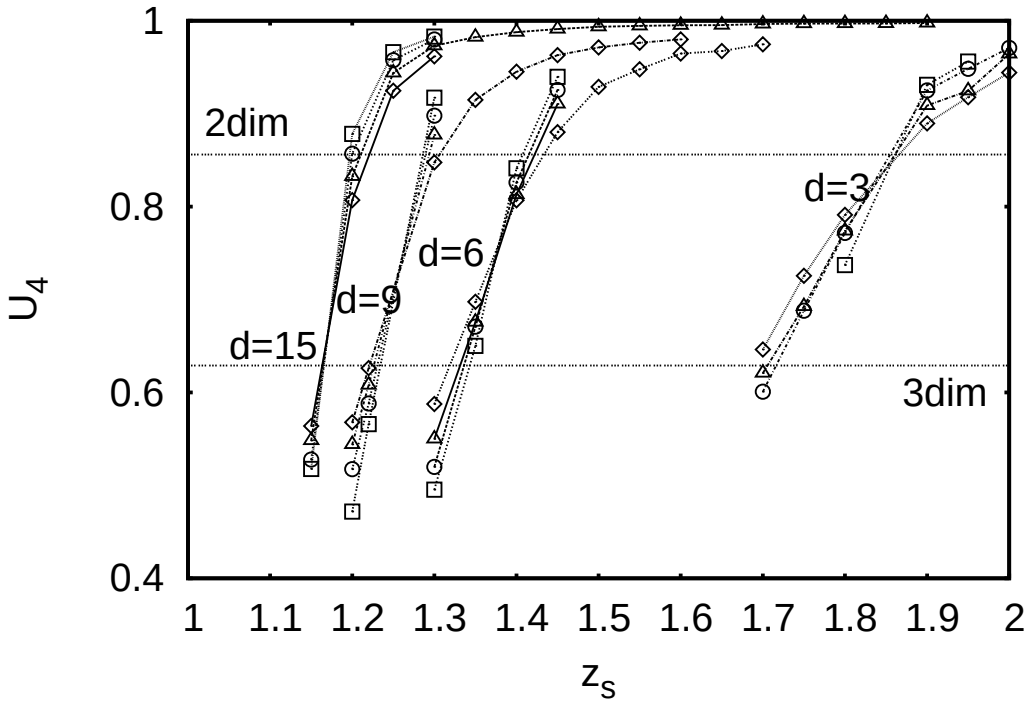

Figure 6.11: Cumulant ratio U_4 as a function of the sphere fugacity close to the critical point in confinement. Distances between the walls are $d = 15\ D$ (box lengths $L_x = 15\ D$ (diamonds), 18 D (triangles), 21 D (circles) and 24 D (squares)), $d = 9\ D$ (box lengths $L_x = 12\ D$ (diamonds), 15 D (triangles), 18 D (circles) and 21 D (squares)), $d = 6\ D$ (box lengths $L_x = 12\ D$ (diamonds), 15 D (triangles), 18 D (circles) and 21 D (squares)) and $d = 3\ D$ (box lengths $L_x = 12\ D$ (diamonds), 15 D (triangles), 18 D (circles) and 21 D (squares)). Aspect ratio $L/D = 3$. Intersection values of the Ising universality class in $2dim$ and $3dim$ are indicated by horizontal lines.

to the walls. Unless the wall separation is reduced to less than twice the uniaxial film thickness, the critical volume fraction of rods stays almost constant on the decrease of the distance between the walls. Once the uniaxial layers at the walls start to interact, the critical point is shifted back in the direction of the bulk critical rod volume fraction.

A method by which the wetting behaviour can be extracted from the grand canonical distribution of particle concentration was introduced. On approach of the critical point, the system shows complete wetting in accordance with the Cahn argument. Contact angles of droplets in the regime of incomplete wetting are estimated without the need of simulating such wall-attached large droplets.

Experimentally, suspensions of rods and depletant are relevant in various contexts, such as colloidal liquid crystal models made from fd-virus and polymers, low-weight conductors made from carbon nanotubes and surfactant micelles, and actin filaments in the crowded environment of the cell. Therefore these calculations can hopefully serve as a guideline to what can be expected in experiments if the systems are confined to a slit-pore.

Chapter 7

Summary

In this thesis Monte Carlo simulations of a mixture of hard spherocylinders and ideal spheres are presented. The emphasis was on the depletion effects caused by the addition of spheres on the isotropic phase of rod-like particles. Although most of the present experimental studies consider systems close to or beyond the isotropic-nematic transition, the isotropic phase with depletion interactions turns out to be a not less interesting topic.

First, the percolation problem was studied in a system of hard rods and soft spheres, where the amount of depletant was kept low to prevent phase separation of the mixture. Then, the phase diagram of isotropic-isotropic demixing of short spherocylinders was calculated for two rod aspect ratios. After an analysis of the bulk, the phase behaviour in confinement was studied.

The canonical simulations confirmed the experimental results on decrease of the percolation threshold in an isotropic fluid of rod-like particles upon addition of depletant. The very simple model allowed to extract the exact nature of the effect seen in experiment, which is the entropically induced attraction. The local changes in the structure of the fluid of rods, which were measured in the simulations, indicated that the depletion forces enhance local alignment and aggregation of the rods. However, the density window of the sphere concentrations, in which these local changes of the structure are too short-ranged and comparatively small to induce global ordering or phase separation, is rather large. Thus, the percolation threshold can be decreased drastically by adding a depleting agent, especially if

one takes into account one more result of the simulations presented here, namely, that the exact nature of the depletant does not play a role – there was no difference in the effects when using ideal and hard spheres.

To study the isotropic-isotropic phase separation grand canonical simulations combined with the successive umbrella sampling method were used. The phase diagram was presented for two rod aspect ratios. The critical point was determined by a finite size scaling analysis. The interfacial tension between the gas-like rod-poor and liquid-like rod-rich phases was calculated and found to scale on the approach to the critical point with the critical exponent of the $3dim$ Ising model. Also for the order parameter the scaling behaviour of the Ising universality class is recovered. The obtained phase diagram was compared to the predictions of the free volume theory, where the deviations close to the critical point confirmed the mean-field character of the theory. Away from the critical point the simulation results coincide with the analytical values.

In confinement, where the hard walls induce parallel anchoring, the phase diagram dependency on the distance between the walls was studied once more in the grand canonical ensemble with the successive umbrella sampling method. The structure of the liquid was analysed in canonical simulations. The rods form uniaxial layered films on the walls, which in the isotropic phases are of the thickness comparable with the rod length. The effect of confinement is different in the rod-poor and in the rod-rich phases. The gas-like phase is stable at volume fractions of rods, which are larger compared to the bulk values. The liquid-like phase, on the contrary, is shifted to lower volume fractions compared to the bulk. The effect is due to the density of the uniaxial films on the walls – its density is higher in the gas-like, and lower in the liquid-like phase compared to the bulk. The findings agree with the theoretical prediction of adsorbing of rods onto the hard walls due to the depletion interactions, however, the prediction that the rods would form a single monolayer is not confirmed – the considered films turn out to have a least two layers. The critical point as a function of the wall separation was calculated from the finite size analysis. The crossover from $3dim$ to $2dim$ critical Ising behaviour is clearly visible. A method to calculate the contact angle of the liquid-gas interface with the

wall is introduced. The wetting behaviour on the approach to the critical point is analysed, confirming Cahn argument, without the need to simulate large wall-attached droplets.

Bibliography

Adams, M., Dogic, Z., Keller, S., and Fraden, S. (2004). Entropically driven microphase transitions in mixtures of colloidal rods and spheres. *Phys. Rev. E*, **69**, 051702.

Balberg, I., Anderson, C., Alexander, S., and Wagner, N. (1984). Excluded volume and its relation to the onset of percolation. *Phys. Rev. B*, **30**, 3933.

Bates, M. and Frenkel, D. (2000). Phase behavior of two-dimensional hard rod fluid. *J. Chem. Phys.*, **112**, 10034.

Baughman, R., Zakhidov, A., and de Heer, W. (2002). Carbon nanotubes – the route toward applications. *Science*, **297**, 787.

Biben, T., Bladon, P., and Frenkel, D. (1996). Depletion effects in binary hard-sphere fluids. *J. Phys.: Condens. Matter*, **8**, 10799.

Binder, K. (1981). Finite size scaling analysis of Ising model block distribution functions. *Z. Phys. B - Condensed Matter*, **43**, 119.

Binder, K. (1982). Monte Carlo calculation of the surface tension for two- and three-dimensional lattice-gas models. *Phys. Rev. A*, **25**, 1699.

Binder, K. and Hohenberg, P. (1972). Phase transitions and static spin correlations in Ising models with free surfaces. *Phys. Rev. B*, **6**, 3461.

Binder, K. and Hohenberg, P. (1974). Surface effects on magnetic phase transitions. *Phys. Rev. B*, **9**, 2194.

Boamfa, M., Kim, M., Maan, J., and Rasing, T. (2003). Observation of surface and bulk phase transitions in nematic liquid cristals. *Nature*, **421**, 149.

Bolhuis, P. and Frenkel, D. (1997). Tracing the phase boundaries of hard spherocylinders. *J. Chem. Phys.*, **106**, 666.

Bolhuis, P., Stroobants, A., Frenkel, D., and Lekkerkerker, H. (1997). Numerical study of the phase behaviour of rodlike colloids with attractive interactions. *J. Chem. Phys.*, **107**, 1551.

Buitenhuis, J., Donselaar, L., Buining, P., Stroobants, A., and Lekkerkerker, H. (1995). Phase separation of mixtures of colloidal boehmite rods and flexible polymer. *Journal of Colloid and Interface Science*, **175**, 46.

Chen, W., Martinez-Miranda, L., Hsiung, H., and Shen, Y. (1989). Orientational wetting behavior of a liquid-crystal homologous series. *Phys. Rev. Lett.*, **62**, 1860.

Chen, Y. and Schweizer, K. (2002). Depletion interaction in suspensions of spheres and rod-polymers. *J. Chem. Phys.*, **117**, 1351.

Chen, Y. and Schweizer, K. (2004). Liquid-state theory of structure, thermodynamics, and phase separation in suspensions of rod polymers and hard spheres. *J. Phys. Chem. B*, **108**, 6687.

Cotter, M. (1977). Hard spherocylinders in an anisotropic mean field: A simple model for a nematic liquid crystal. *J. Chem. Phys.*, **66**, 1098.

Cotter, M. and Wacker, D. (1978). Van der Waals theory of nematogenic solutions. I. Derivation of the general equations. *Phys. Rev. A*, **18**, 2669.

Cuetos, A., Martinez-Haya, B., Lago, S., and Rull, L. (2007). Use of Parsons-Lee and Onsager theories to predict nematic and demixing behaviour in binary mixtures of hard rods and hard spheres. *Phys. Rev. E*, **75**, 061701.

de Gennes, P. (1971). Short range order effects in the isotropic phase of nematics and choleristics. *Molecular Crystals and Liquid Crystals*, **12**, 193.

De Virgiliis, A., Vink, R., Horbach, J., and Binder, K. (2007). Colloid-polymer mixtures between asymmetric walls: Evidence for an interface localization transition. *EPL*, **77**, 60002.

Derjaguin, B. (1940). On the repulsive forces between charged colloid particles and on the theory of slow coagulation and stability of lyophobic sols. *Trans. Faraday Soc.*, **36**, 203.

Dhont, J., Lettinga, M., Dogic, Z., Lenstra, T., Wang, H., Rathgeber, S., Carletto, P., Willner, L., Frielinghaus, H., and Lindner, P. (2003). Shear-banding and microstructure of colloids in shear flow. *Faraday Discussions*, **123**, 157.

Diehl, H. (1986). Field-theoretic Approach to Critical Behaviour at Surfaces. In C. Domb and J. Lebowitz, editors, *Phase Transitions and Critical Phenomena*. Academic Press, London.

Dietrich, S. (1988). Wetting Phenomena. In C. Domb and J. Lebowitz, editors, *Phase Transitions and Critical Phenomena*. Academic Press, London.

Dijkstra, M., van Roij, R., and Evans, R. (2001). Wetting and capillary nematization of a hard-rod fluid: A simulation study. *Phys. Rev. E*, **63**, 051703.

Dogic, Z. and Fraden, S. (2001). Development of model colloidal liquid crystals and the kinetics of the isotropic-smectic transition. *Phil. Trans. R. Soc. Lond. A*, **359**, 997.

Dogic, Z. and Fraden, S. (2006). Ordered phases of filamentous viruses. *Current Opinion in Colloid and Interface Sciences*, **11**, 47.

Dogic, Z., Prudy, K., Grelet, E., Adams, M., and Fraden, S. (2004). Isotropic-nematic phase transition in suspensions of filametous virus and the neutral polymer Dextran. *Phys. Rev. E*, **69**, 051702.

Donev, A., Burton, J., Stillinger, F., and Torquato, S. (2006). Tetratic order in the phase behaviour of a hard-rectangle system. *Phys. Rev. B*, **73**, 054109.

Du, F., Fischer, J., and Winey, K. (2005). Effect of nanotube alignment on percolation conductivity in carbon nanotube/polymer composites. *Phys. Rev. B*, **72**, 121404(R).

Fortini, A., Schmidt, M., and Dijkstra, M. (2006). Phase behavior and structure of model colloid-polymer mixtures confined between two parallel planar walls. *Phys. Rev. E*, **73**, 051502.

Fortini, A., Bolhuis, P., and Dijkstra, M. (2008). Effect of excluded volume interactions on the interfacial properties of colloid-polymer mixtures. *J. Chem. Phys.*, **128**, 024904.

Foygel, M., Morris, R., Anez, D., French, S., and Sobolev, V. (2005). Theoretical and computational studies of carbon nanotube composites and suspensions: Electrical and thermal conductivity. *Phys. Rev. B*, **71**, 104201.

Frank, F. (1958). I. Liquid crystals. On the theory of liquid crystals. *Discuss. Faraday Soc.*, **25**, 19.

Frenkel, D. (1987). Onsager's spherocylinders revisited. *J. Phys. Chem.*, **91**, 4912.

Frenkel, D. (1988). Structure of hard-core models for liquid crystals. *J. Phys. Chem.*, **92**, 3280.

Frenkel, D. and Smit, B. (2002). *Understanding Molecular Simulation*. Academic Press, San Diego.

Hsiung, H., Rasing, T., and Shen, Y. (1986). Wall-induced orientational order of a liquid crystal in the isotropic phase – an evanescent-wave-ellipsometry study. *Phys. Rev. Lett.*, **57**, 3065.

Iijima, S. (1991). Helical microtubules of graphitic carbon. *Nature*, **354**, 56.

Kang, K., Lettinga, M., Dogic, Z., and Dhont, J. (2006). Vorticity banding in rodlike virus suspensions. *Phys. Rev. E*, **74**, 026307.

Khare, R. and Bose, S. (2005). Carbon nanotube based composites – a review. *Journal of Minerals & Materials Characterization & Engineering*, **4**, 31.

Koda, T. and Ikeda, S. (2002). Test of the scaled particle theory for aligned hard spherocylinders using Monte Carlo simulation. *J. Chem. Phys.*, **116**, 5825.

Lagomarsino, M., Dogterom, M., and Dijkstra, M. (2003). Isotropic-nematic transition of long, thin, hard spherocylinders confined in a quasi-two-dimensional planar geometry. *J. Chem. Phys.*, **119**, 3535.

Landau, D. and Binder, K. (2000). *A Guide to Monte Carlo Simulations in Statistical Physics*. Cambridge University Press, Cambridge.

Lekkerkerker, H. and Stroobants, A. (1994). Phase behaviour of rod-like colloid + flexible polymer mixtures. *Nuovo Cimento D*, **16**, 949.

Lekkerkerker, H., Poon, W., Pusey, P., Stroobants, A., and Warren, P. (1992). Phase behaviour of colloid + polymer mixtures. *Europhys. Lett.*, **20**, 559.

Lenstra, T., Dogic, Z., and Dhont, J. (2001). Shear-induced displacement of isotropic-nematic spinodals. *J. Chem. Phys.*, **114**, 10151.

Lettinga, M. and Dhont, J. (2004). Non-equilibrium phase behaviour of rod-like viruses under shear flow. *J. Phys. Cond. Matter*, **16**, S3929.

Leung, K. and Chandler, D. (1991). Theory of percolation in fluids of long molecules. *J. Stat. Phys.*, **63**, 837.

Li, W. and Ma, H. (2005). Depletion interactions between two spherocylinders. *Eur. Phys. J. E.*, **16**, 225.

Low, R. (2002). Measuring order and biaxiality. *Eur. J. Phys.*, **23**, 111.

Martínez-Ratón, Y. (2007). Capillary ordering and layering transition in two-dimensional hard-rod fluids. *Phys. Rev. E*, **75**, 051708.

Matsuyama, A. and Kato, T. (2001). Orientation-dependent depletion interaction in rodlike colloid-polymer mixtures. *Eur. Phys. J. E.*, **6**, 15.

McGrother, S., Williamson, D., and Jackson, G. (1996). A re-examination of the phase diagram of hard spherocylinders. *J. Phys. Chem.*, **104**, 6755.

Mecke, K. and Seyfried, A. (2002). Strong dependence of the percolation thresholds on polydispersity. *Europhys. Lett.*, **58**, 28.

Munson-McGee, S. (1991). Estimation of the critical concentration in an anisotropic percolation network. *Phys. Rev. B*, **43**, 3331.

Odijk, T. (1986). Theory of lyotropic polymer liquid crystals. *Macromolecules*, **19**, 2314.

Onsager, L. (1949). The effects of shape on the interaction of colloidal particles. *Ann. N. Y. Acad. Sci.*, **51**, 627.

Oosawa, F. and Asakura, S. (1954). On interaction between two bodies immersed in a solution of macromolecules. *J. Chem. Phys.*, **22**, 1255.

Oseen, C. (1933). The theory of liquid crystals. *Trans. Faraday Soc.*, **29**, 883.

Pike, G. and Seager, C. (1974). Percolation and conductivity: A computer study. I. *Phys. Rev. B*, **10**, 1421.

Poniewierski, A. and Sluckin, T. (1991). Phase diagram for a system of hard spherocylinders. *Phys. Rev. A*, **43**, 6837.

Reinitzer, F. (1888). Beiträge zur Kenntniss des Cholesterins. *Monatsch. Chem.*, **9**, 421.

Savenko, S. and Dijkstra, M. (2006). Phase behavior of a suspension of colloidal hard rods and nonadsorbing polymer. *J. Chem. Phys.*, **124**, 234902.

Schilling, T. (2007). "Formsachen": Computersimulationen zum Phasenverhalten und den Grenzflächeneigenschaften anisotroper Kolloide. *Habilitationsschrift*. Johannes Gutenberg-Universität Mainz.

Sear, R. (1998). Depletion driven adsorption of colloidal rods onto a hard wall. *Phys. Rev. E*, **57**, 1983.

Sonin, A. (1991). What are liqiud crystals? (On the 100th anniversary of the discovery). *J. Struc. Chem.*, **32**, 111.

Stauffer, D. and Aharony, A. (1994). *Introduction to Percolation Theory*. Taylor & Fransis, London.

Tang, J. and Fraden, S. (1995). Isotropic-choleristic phase transition in colloidal suspensions of filamentous bacteriophage fd. *Liquid Crystals*, **19**, 459.

Tuinier, R., Taniguchi, T., and Wensink, H. (2007). Phase behavior of a suspension of hard spherocylinders plus ideal polymer chains. *Eur. Phys. J. E*, **23**, 355.

van Iterson, Jr., G. (1933). A simple arrangement to demonstrate liquid crystals. *Trans. Faraday Soc.*, **29**, 915.

van Roij, R. (2005). The isotropic and nematic liquid crystal phase of colloidal rods. *Eur. J. Phys.*, **26**, S57.

van Roij, R., Dijkstra, M., and Evans, R. (2000a). Interfaces, wetting, and capillary nematization of a hard-rod fluid: Theory for the Zwanzig model. *J. Chem. Phys.*, **113**, 7689.

van Roij, R., Dijkstra, M., and Evans, R. (2000b). Orientational wetting and capillary nematization of hard-rod fluids. *Europhys. Lett.*, **49**, 350.

Verwey, E. (1940). Electrical double layer and stability of emulsions. *Trans. Faraday Soc.*, **36**, 192.

Vigolo, B., Coulon, C., Maugey, M., Zakri, C., and Poulin, P. (2005). An experimental approach to the percolation of sticky nanotubes. *Science*, **309**, 920.

Vink, R. (2007). Liquid crystrals in two dimensions: First-order phase transition and nonuniversal critical behaviour. *Phys. Rev. Lett*, **98**, 217801.

Vink, R. and Horbach, J. (2004). The fluid-fluid interface in a model colloid-polymer mixture: Application of grand canonical Monte Carlo to asymmetric binary mixtures. *J. Chem. Phys.*, **121**, 3253.

Vink, R. and Schilling, T. (2005). Interfacial tension of the isotropic-nematic interface in suspensions of soft spherocylinders. *Phys. Rev. E*, **71**, 051716.

Vink, R. and Wensink, H. (2006). Coexistence diameter in two-dimensional colloid-polymer mixtures. *Phys. Rev. E*, **74**, 010102.

Vink, R., Wolfsheimer, S., and Schilling, T. (2005). Isotropic-nematic interfacial tension of hard and soft rods: application of advanced grand canonical biased sampling techniques. *J. Chem. Phys.*, **123**, 074901.

Vink, R., Binder, K., and Horbach, J. (2006a). Critical behavior of a colloid-polymer mixture confined between walls. *Phys. Rev. E*, **73**, 056118.

Vink, R., De Virgiliis, A., Horbach, J., and Binder, K. (2006b). Phase diagram and structure of colloid-polymer mixtures confined between walls. *Phys. Rev. E*, **74**, 031601.

Virnau, P. and Müller, M. (2004). Calculation of free energy through successive umbrella sampling. *J. Chem. Phys.*, **120**, 10925.

Vrij, A. (1976). Polymers at interfaces and the interactions in colloidal dispersions. *Pure Appl. Chem.*, **48**, 471.

Vroege, G. and Lekkerkerker, H. (1992). Phase transitions in lyotropic colloidal and polymer liquid crystals. *Rep. Prog. Phys.*, **55**, 1241.

Wang, H., Zhou, W., Ho, D., Winey, K., Fischer, J., Glinka, C., and Hobbie, E. (2004). Dispersing single-walled carbon nanotubes with surfactant: A small angle neutron scattering study. *Nanoletters*, **4**, 1789.

Wang, X. and Chatterjee, A. (2003). Connectedness percolation in athermal mixtures of flexible and rigid macromolecules: Analytic theory. *J. Chem. Phys.*, **118**, 10787.

Wessels, P., Schmidt, M., and Löwen, H. (2004). The contact angle of the colloidal liquid-gas interface and a hard wall. *J. Phys.: Condens. Matter*, **16**, S4169.

Appendix A

Theory

A.1 Free volume theory

The theoretical approach to rod-sphere mixtures was introduced by Lekkerkerker and Stroobants in 1994 [Lekkerkerker and Stroobants (1994)]. The starting point is the thermodynamic potential in the semi-grand canonical ensemble, where the number of rods is fixed, while the number of "penetrable hard" spheres is set by the chemical potential of spheres in a hypothetical reservoir that is held in equilibrium with the system. The potential $\Omega^{\text{semi}}(N_r, V, T, \mu_s)$ of such a mixture can be written as

$$\begin{aligned} \Omega^{\text{semi}}(N_r, V, T, \mu_s) &= F(N_r, V, T) + \int_{-\infty}^{\mu_s^R} \frac{\partial \Omega^{\text{semi}}(N_r, V, T, \mu_s'^R)}{\partial \mu_s'^R} d\mu_s'^R \\ &= F(N_r, V, T) - \int_{-\infty}^{\mu_s^R} N_s d\mu_s'^R, \end{aligned} \tag{A.1}$$

where $F(N_r, V, T)$ is the free energy of N_r rods in a volume V at temperature T, and the second term accounts for the perturbation due to the addition of N_s spheres from a reservoir, where the chemical potential is kept at μ_s^R. Osmotic equilibrium requires the chemical potential of the system and of the reservoir to be equal. The chemical potential of an ideal gas of spheres is connected to the density ρ_s via

$$\rho_s = \exp\left(\frac{\mu_s}{k_B T}\right). \tag{A.2}$$

Thus, the number of spheres in the system N_s depends on μ_s^R. The only influence the rods have on the spheres is the reduction of the free volume,

$$N_s = \rho_s^R V_{\text{free}}, \tag{A.3}$$

where V_{free} is the volume accessible for spheres in the system under the assumption that the rod configurations are undistorted upon adding spheres and ρ_s^R is the number density of spheres in the reservoir. The free volume fraction α is defined as

$$\alpha = \frac{V_{\text{free}}}{V} \tag{A.4}$$

and it can be calculated within scaled particle theory. Hence, the expression for the semi-grand canonical potential is reduced to

$$\Omega^{\text{semi}}(N_r, V, T, \mu_s) = F(N_r, V, T) - \alpha V k_B T \rho_s^R \tag{A.5}$$

Normalised using

$$\begin{aligned} w^{\text{semi}} &= \frac{\Omega^{\text{semi}} v_r}{k_B T V} \\ f^* &= \frac{F v_r}{k_B T V} \end{aligned} \tag{A.6}$$

the equation reduces to

$$\omega^{\text{semi}} = f^* - \alpha v_r \rho_s^R = f^* - \alpha \frac{v_r}{v_s} \eta_s^R \tag{A.7}$$

with v_r volume of a spherocylinder of length L and diameter D and v_s volume of a sphere.

$$\eta_s^R = \rho_s^R v_s \tag{A.8}$$

is the reservoir volume fraction of the spheres.

The chemical potential μ_r as well as the osmotic pressure Π_r of the rods in the mixture can be obtained from the following thermodynamic relationships

$$\begin{aligned} \frac{\mu}{k_B T} &= \frac{1}{k_B T} \left(\frac{\partial \Omega^{\text{semi}}}{\partial N_r} \right)_V \\ &= \frac{v_r}{k_B T V} \left(\frac{\partial \Omega^{\text{semi}}}{\partial \eta_r} \right)_V = \left(\frac{\partial \omega^{\text{semi}}}{\partial \eta_r} \right)_V \end{aligned} \tag{A.9}$$

$$\begin{aligned}\frac{\Pi v_r}{k_B T} &= -\frac{v_r}{k_B T}\left(\frac{\partial \Omega^{\text{semi}}}{\partial V}\right)_{N_r} \\ &= -\left(\frac{\partial(\omega^{\text{semi}} V)}{\partial V}\right)_{N_r} = \eta_r \left(\frac{\partial \omega^{\text{semi}}}{\partial \eta_r}\right)_{N_r} - \omega^{\text{semi}} \end{aligned} \tag{A.10}$$

where

$$\eta_r = \rho_r v_r \tag{A.11}$$

is the volume fraction of the rods and

$$v_r = \pi\left(\frac{D^3}{6} + \frac{LD^2}{4}\right) \tag{A.12}$$

the volume of one spherocylinder. At coexistence, the chemical potential and pressure are equal.

A.1.1 Rod-sphere mixtures

The free energy of a system of hard spherocylinders can be calculated using scaled particle theory [Cotter (1977); Cotter and Wacker (1978)] (cp. Section A.2)

$$f^* = \frac{y}{y+1}\left(\text{const} + \ln(y) + \sigma[f] + \Pi_2 y + \frac{\Pi_3}{2} y^2\right) \tag{A.13}$$

with

$$y = \frac{\eta_r}{1-\eta_r} \tag{A.14}$$

The coefficients Π_2 and Π_3 are defined in equation (A.25). $\sigma[f]$ is a functional of the orientational distribution function f, defined in Section A.2. The free volume fraction can be calculated from the scaled particle as described in Section A.2

$$\alpha = \frac{1}{1+y} e^{-\left(Ay + By^2 + Cy^3\right)}, \tag{A.15}$$

with A, B and C given by equations (A.37).

The orientational distribution function f, which minimises the semi-grand canonical potential, can be obtained either numerically or from the Gaussian approximation as described in the Section A.2.

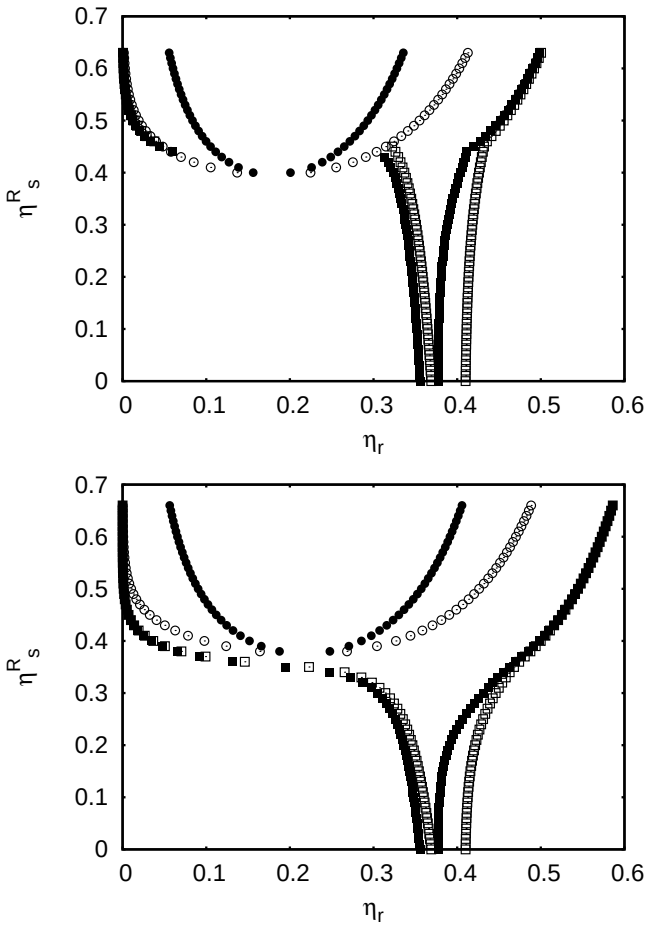

Figure A.1: Phase diagrams for $L/D = 5$, $q = 0.8$ (top) and $L/D = 5$, $q = 0.65$ (bottom). The isotropic-nematic transition is calculated with Gaussian (open squares) and numerical (solid squares) minimisation techniques. Open circles correspond to the isotropic-isotropic binodal, solid circles stand for its spinodal. The isotropic-isotropic transition is prevented by the isotropic-nematic transition at $q = 0.65$.

All together, the chemical potential and the pressure of rods in the mixture can be calculated (at least numerically) for different rod volume fractions at fixed sphere reservoir concentration. The states with equal values of both yield the coexisting phases, i.e. the phase diagram of the mixture. Also the spinodal line of the mixture can be determined from the theory. The states, in which the derivatives of the pressure and of the rod chemical potential with respect to the rod volume fraction are equal, yield the points on the spinodal.

Phase diagrams

Figures A.1 and A.2 show examples of the calculated phase diagrams. The occurrence of the isotropic-isotropic transition depends on the size of the spheres in terms of the rod diameter, defined as $q = D_s/D$, as well as on the rod length. For rod aspect ratio $L/D = 5$ isotropic-isotropic demixing is prevented by the isotropic-nematic transition if the radius of spheres is smaller than $\sim 0.7\ D$, as shown in Figure A.1. The effect due to the rod length is shown in Figure A.2, where for fixed sphere size $q = 1$ the isotropic-isotropic demixing becomes unstable with respect to the isotropic-nematic transition for $L/D = 8$, but not for $L/D = 7$.

The figures A.1 and A.2 also compare the solutions to the isotropic-nematic transition obtained using the numerical (solid squares) and Gaussian (open squares) minimisation techniques. The numerical approach predicts the isotropic-nematic transition at slightly lower rod volume fractions as well as a narrower coexistence region than the Gaussian approximation. However, the solutions approach each other as the rod volume fraction in the nematic phase increases.

A.2 Scaled particle theory

A.2.1 Free energy

The free energy of a pure rod system can be calculated using the scaled particle theory [Cotter (1977); Cotter and Wacker (1978)], which was tested for the case of aligned spherocylinders in Monte Carlo simulation [Koda and Ikeda (2002)]. The diameter and the length of a spherocylinder are scaled separately and the work applied by insertion of the scaled particle into a solution of rod-like particles of finite aspect ratio is expanded in the limit of small scaling parameters. The method is described for spherical particles in the next subsection. For spherocylinders there are additional terms which take the length of the spherocylinder into account and depend on the distribution of orientations of particles forming the liquid, into which the test particle is to be inserted.

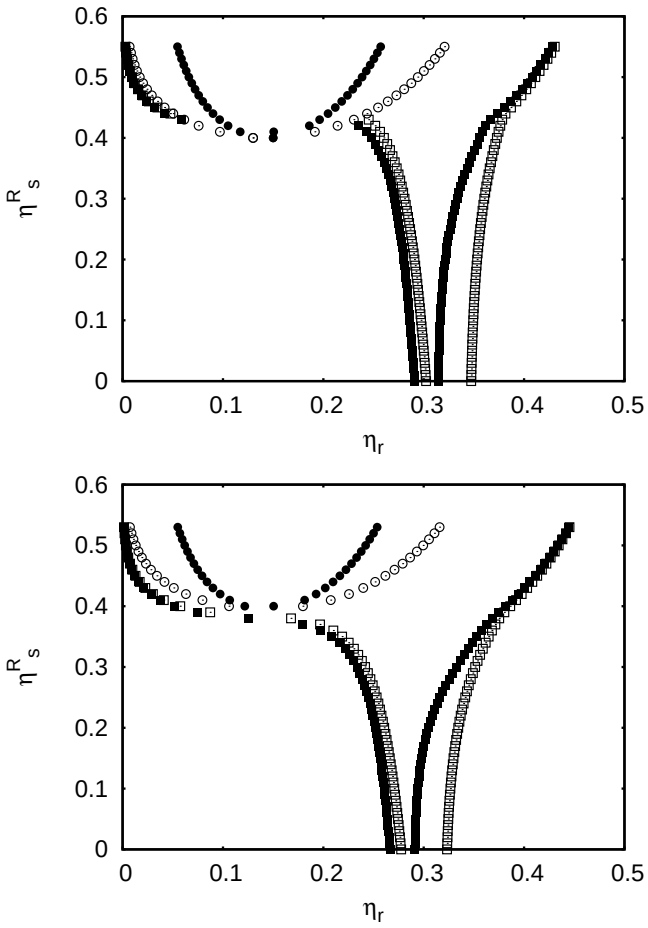

Figure A.2: Phase diagrams for $L/D = 7$, $q = 1$ (top) and $L/D = 8$, $q = 1$ (bottom). The isotropic-nematic transition is calculated with Gaussian (open squares) and numerical (solid squares) minimisation techniques. Open circles correspond to the isotropic-isotropic binodal, solid circles stand for its spinodal. The isotropic-isotropic transition is prevented by isotropic-nematic transition when the rods become larger.

To calculate the free energy within the scaled particle approach one defines the work function $w(\mathbf{u}, \lambda_1, \lambda_2)$, which is the reversible work required to add a scaled spherocylinder with fixed orientation $\mathbf{u}$, length $\lambda_1 L$ and diameter $\lambda_2 D$ to the system at some arbitrary point. The work function is related to the configurational Gibbs free energy of the system

$$\frac{G}{N_r k_B T} = \int d\mathbf{u} f(\mathbf{u}) \left[\ln(\rho_r f(\mathbf{u})) + \frac{w(\mathbf{u}, 1, 1)}{k_B T} \right] \tag{A.16}$$

where $f(\mathbf{u})$ is the normalised one-particle orientational distribution.

For small perturbations (λ_1, λ_2) the work function can be written as

$$w(\mathbf{u}, \lambda_1, \lambda_2) = -\ln\left(1 - \rho_r \int d\mathbf{u}' v_{\mathrm{ex}}(\mathbf{u}, \mathbf{u}')\right) \tag{A.17}$$

where $v_{\mathrm{ex}}(\mathbf{u}, \mathbf{u}')$ is the volume excluded to the centre of a 'regular' spherocylinder with orientation $\mathbf{u}'$ by the presence of a scaled spherocylinder with orientation $\mathbf{u}$.

$$\begin{aligned} v_{\mathrm{ex}}(\mathbf{u}, \mathbf{u}') &= \pi L(1+\lambda_1)D^2(1+\lambda_2)^2 + \frac{4}{3}\pi D^3(1+\lambda_2)^3 \\ &\quad + 2D(1+\lambda_2)L^2\lambda_1|\sin[\Phi(\mathbf{u}, \mathbf{u}')]| \end{aligned} \tag{A.18}$$

$\Phi(\mathbf{u}, \mathbf{u}')$ is the angle between orientational vectors $\mathbf{u}$ and $\mathbf{u}'$.

For large (λ_1, λ_2) the required work is the creation of a void of the size of a scaled spherocylinder against the osmotic pressure of the liquid.

$$w(\mathbf{u}, \lambda_1, \lambda_2) = \left(\frac{\pi}{6}D^3\lambda_2^3 + \frac{\pi}{4}L\lambda_1 D^2\lambda_2^2\right)\Pi \tag{A.19}$$

Taylor expansion of equation A.17 around $(\lambda_1 = 0, \lambda_2 = 0)$ up to the second order and addition of equation A.19 as the third-order term yields

$$\begin{aligned} w(\mathbf{u}, \lambda_1, \lambda_2) &= c_{00} + c_{10}\lambda_2 + c_{01}\lambda_1 + c_{11}\lambda_2\lambda_1 + c_{20}\lambda_2^2 \\ &\quad + \left(\frac{\pi}{6}D^3\lambda_2^3 + \frac{\pi}{4}L\lambda_1 D^2\lambda_2^2\right)\Pi \end{aligned} \tag{A.20}$$

where

$$c_{lm} = (l!m!)^{-1}\left.\frac{\partial^{l+m} w}{\partial\lambda_2^l \partial\lambda_2^m}\right|_{\lambda_1=0,\lambda_2=0} \tag{A.21}$$

With $(\lambda_1 = 1, \lambda_2 = 1)$ this is the work function for insertion of a regular spherocylinder. The pressure can be obtained with the aid of the Gibbs-Duhem equation

$$\frac{\partial\Pi}{\partial\rho_r} = \rho_r\frac{\partial G}{\partial\rho_r} \tag{A.22}$$

The Helmholtz free energy of the system is

$$\frac{F}{N_r k_B T} = \frac{G}{N_r k_B T} - \frac{\Pi}{\rho_r k_B T} \tag{A.23}$$

After insertion of the expressions for the Gibbs free energy and pressure and in rescaled units the free energy of a fluid of spherocylinders reads

$$f^* = \frac{y}{y+1}\left(\mathrm{const} + \ln(y) + \sigma[f] + \Pi_2 y + \frac{\Pi_3}{2}y^2\right) \tag{A.24}$$

where

$$\begin{aligned}\Pi_2 &= 3+\frac{3(\tau-1)^2}{3\tau-1}\rho[f]\\ \Pi_3 &= \frac{12\tau(2\tau-1)}{(3\tau-1)^2}+\frac{12\tau(\tau-1)^2}{(3\tau-1)^2}\rho[f],\end{aligned} \tag{A.25}$$

and τ is the overall length-to-diameter ratio of the spherocylinders

$$\tau=\frac{L+D}{D}. \tag{A.26}$$

The coefficients in equation A.25 would become singular for $\tau = 1/3$, but, since it corresponds to a negative value of the rod aspect ratio ($L/D = -2/3$), this case can safely be ignored. Actually, only rods of finite lengths are considered here, thus, any value of $\tau < 1$ does not make any sense. For $\tau = 1$ the particles are spheres, and the Percus-Yevick equation of state is recovered

$$\frac{v_r\Pi}{k_BT}=y+3y^2+3y^3. \tag{A.27}$$

$\sigma[f]$ and $\rho[f]$ are functionals of the orientational distribution function f

$$\sigma[f] = \int f(\mathbf{u})\ln[4\pi f(\mathbf{u})]d\mathbf{u} \tag{A.28}$$

$$\rho[f] = \frac{4}{\pi}\int\int \sin[\Phi(\mathbf{u},\mathbf{u}')]f(\mathbf{u})f(\mathbf{u}')d\mathbf{u}d\mathbf{u}' \tag{A.29}$$

with $\mathbf{u}$ being an orientation vector of a particle, while $\Phi(\mathbf{u},\mathbf{u}')$ stands for the angle between the orientation vectors of two particles. The normalised one-particle orientational distribution $f(\mathbf{u})$ is chosen to minimise the free energy.

Chemical potential and osmotic pressure are

$$\frac{\mu}{k_BT}=\text{const}+\ln y+\sigma[f]+(2\Pi_2+1)y+(1.5\Pi_3+\Pi_2)y^2+\Pi_3y^3 \tag{A.30}$$

$$\frac{v_r\Pi}{k_BT}=y+\Pi_2y^2+\Pi_3y^3 \tag{A.31}$$

A.2.2 Free volume fraction

The scaled particle theory can be used to yield the free volume fraction available to a sphere in a system of rods. The work required to bring a

particle of size λq ($q = D_s/D$ and $\lambda \in [0,1]$) from the reservoir into the system is

$$\frac{w}{k_B T} = -\ln \alpha. \tag{A.32}$$

If the excluded volumes of the rods are assumed to have no overlaps, which is valid for $\lambda \to 0$, it can be written as

$$w(\lambda) = -k_B T \ln\left(1 - \rho_r \left(\frac{\pi}{4} D^2 L (1+\lambda q)^2 + \frac{\pi}{6} D^3 (1+\lambda q)^3\right)\right) \tag{A.33}$$

and for very large spheres ($\lambda \to 1$) it is the work needed to create a hole of the size of a sphere in the fluid of rods

$$w(\lambda) = \frac{\pi D^3}{6} (\lambda q)^3 \Pi \tag{A.34}$$

with Π being osmotic pressure due to the colloidal rods. Taylor expansion up to the quadratic order in λ of equation A.33 and addition of the equation A.34 as the third order term yield

$$w(\lambda) = w(0) + \left.\frac{\partial w}{\partial \lambda}\right|_{\lambda=0} \lambda + \frac{1}{2} \left.\frac{\partial^2 w}{\partial \lambda^2}\right|_{\lambda=0} \lambda^2 + \frac{\pi D^3}{6} (\lambda q)^3 \Pi \tag{A.35}$$

Setting the scaling parameter λ to one and using the osmotic pressure of rods given by equation A.31, an approximation of the work function is obtained, which is the used to calculate the free volume fraction via equation A.32.

$$\alpha = \frac{1}{1+y} \exp\left(-\left[Ay + By^2 + Cy^3\right]\right), \tag{A.36}$$

where

$$\begin{aligned} A &= \frac{6\tau}{3\tau - 1} q + \frac{3(\tau+1)}{3\tau - 1} q^2 + \frac{2}{3\tau - 1} q^3 \\ B &= \frac{18\tau^2}{(3\tau-1)^2} q^2 + \left(\frac{6}{\tau - 1} + \frac{6(\tau-1)^2}{(3\tau-1)^2} \rho[f]\right) q^3 \\ C &= \frac{2}{3\tau - 1} \left(\frac{12\tau(2\tau-1)}{(3\tau-1)^2} + \frac{12\tau(\tau-1)^2}{(3\tau-1)^2}\right) q^3 \end{aligned} \tag{A.37}$$

A.2.3 Orientational distribution function

Isotropic phase

In the isotropic case all orientations are equally probable, thus, the orientational distribution is uniform and since it should be normalised to one,

is given by

$$f(\mathbf{u}) = \frac{1}{4\pi} \tag{A.38}$$

The functionals of the orientational distribution function can be integrated, yielding

$$\sigma[f] = 0 \tag{A.39}$$

$$\rho[f] = 1 \tag{A.40}$$

Now everything needed to describe the isotropic phase of rod-like particles is known. For short rods the isotropic-isotropic demixing transition can be described without use of the minimisation techniques, which were applied when calculating the free energy of nematic phase.

Nematic phase

In the anisotropic case the form of the orientational distribution function should be chosen such that it minimises the free energy under the normalisation condition

$$\int f(\mathbf{u}) d\mathbf{u} = 1. \tag{A.41}$$

This can be done either fully numerically or by choosing a trial function which depends on a variational parameter and then minimising the free energy with respect to this parameter.

If the nematic phase has uniaxial symmetry, the orientational distribution function will only depend on θ, the angle between the one-particle orientation and the nematic director of the system. $\theta \in [0, \pi]$ and in the case of an uniaxial nematic fluid,

$$f(\theta) = f(\theta - \pi) \tag{A.42}$$

Numerical minimisation

The orientational distribution $f(\mathbf{u})$ has to be chosen to minimise the free energy f^* of the fluid and to fulfil the normalisation condition (equation A.41). To do so, the functional derivative of $f^*[f(\mathbf{u})] - \lambda \int f(\mathbf{u}) d(\mathbf{u})$ (λ is a Lagrange multiplier) with respect to $f(\mathbf{u})$ has to be set to zero, and yields

$$\ln(4\pi f(\mathbf{u})) = \lambda C - \mathcal{X} \int \sin[\Phi(\mathbf{u},\mathbf{u}')] f(\mathbf{u}') d\mathbf{u}' \tag{A.43}$$

with

$$\mathcal{X} = \frac{3(\tau-1)^2}{3\tau-1} y + \frac{6\tau(\tau-1)^2}{(3\tau-1)^2} y^2, \tag{A.44}$$

and C independent on $\mathbf{u}$. The distribution $f(\mathbf{u})$ is the solution of the non-linear integral equation

$$f(\mathbf{u}) = \frac{1}{Z} \exp\left[-\mathcal{X} \int \sin[\Phi(\mathbf{u},\mathbf{u}')] f(\mathbf{u}') d\mathbf{u}'\right] \tag{A.45}$$

where $1/Z$ accounts for the normalisation. The way to solve this equation numerically on a discrete grid was described by van Roij [van Roij (2005)].

Gaussian distribution

Here, the starting point is a normalised trial function, which depends on a variational parameter ξ. The distribution function of the Gaussian form fulfils the requirements for an orientational distribution function [Onsager (1949); Odijk (1986)].

$$f(\theta) = \begin{cases} \frac{\xi}{4\pi} \exp\left[-\frac{1}{2}\xi\theta^2\right], & 0 \le \theta \le \frac{\pi}{2} \\ \frac{\xi}{4\pi} \exp\left[-\frac{1}{2}\xi(\pi-\theta)^2\right], & \frac{\pi}{2} \le \theta \le \pi \end{cases} \tag{A.46}$$

In the leading order of large ξ the functionals can be approximated as:

$$\sigma[f] \sim \ln(\xi) - 1 \tag{A.47}$$

$$\rho[f] \sim \frac{4}{\sqrt{\pi\xi}} \tag{A.48}$$

With these approximations the free energy depends only on the variational parameter ξ and can be minimised.

Appendix B

Configurational bias

The probabilities of standard insertion moves of hard particles become very low in a dense phase due to overlaps, which makes the simulation inefficient. In a previous work [Vink *et al.* (2005)] successive umbrella sampling on the nematic order parameter (instead of the number of spherocylinders) was used to overcome this problem. The range of the nematic order parameter values was divided into windows and during simulation of one window the order parameter value was kept at the inside of this window, while the number of particles was allowed to fluctuate freely.

Another possibility, which is described here, is a modification of the insertion move to decrease the probability to create an overlap. In accordance to the cluster move of the sphere-dense phase presented in the main text, a way to create a new configuration with as few overlaps as possible is needed. Close to the isotropic-nematic transition the orientation of rods plays a crucial role. In the usual moves the orientation of spherocylinders to be inserted is chosen randomly. In the nematic phase the orientational distribution is not uniform, thus, creation of the new orientation according to a pre-defined distribution [Landau and Binder (2000)] might increase acceptance probabilities. Here the way to create new orientations is described.

B.1 Creation of a new orientation

A system in the nematic phase has a preferred direction, in which the rods are aligned. The distribution of the polar angles of particle orientations with respect to the nematic director can be expanded using Legendre polynomials.

$$\begin{aligned} P(\theta) &= \frac{1}{2} + \frac{5}{2}\langle P_2\rangle P_2(\cos\theta) + ... \\ &= \frac{1}{2} + \frac{5}{2}\langle P_2\rangle \left(\frac{3}{2}\cos^2\theta - \frac{1}{2}\right) + ... \end{aligned} \tag{B.1}$$

where the averaged second Legendre polynomial $\langle P_2\rangle$, or the nematic order parameter S, is the first order measure of how well the molecules are ordered in the direction of the nematic director. Only the first two terms of the expansion are used here.

The distribution $P(\theta, \phi)$ has to be normalised

$$\int_0^{\pi}\int_0^{2\pi} d\theta d\phi \sin\theta P(\theta) = 1 \tag{B.2}$$

If the (random) distribution of the azimuthal angles is chosen to be

$$P(\phi) = \frac{1}{2\pi}, \tag{B.3}$$

the distribution in both angles can be written as

$$\begin{aligned} P(\theta,\phi) &= \frac{1}{4\pi}(1 + 5SP_2(\cos\theta)) \\ &= \frac{1}{4\pi}(1 + \frac{5S}{2}(3\cos^2\theta - 1)) \end{aligned} \tag{B.4}$$

with S the nematic order parameter, which is close to zero in the isotropic phase and one in the ideal nematic phase.

Integration over the azimuthal angle $0 < \phi < 2\pi$ leads to

$$P(\theta) = \frac{1}{2}\left[1 + \frac{5S}{2}\left(3\cos^2\theta - 1\right)\right] \tag{B.5}$$

Now the integrated distribution function $F(x)$ is calculated.

$$\begin{aligned} F(x) &= \int_0^x d\theta \sin\theta P(\theta) \\ &= \int_0^x d\theta \sin\theta \left[\frac{1}{2} + \frac{5S}{4}\left(3\cos^2\theta - 1\right)\right] \\ &= (1-\cos x)\left(\frac{1}{2} - \frac{5S}{4}\right) + \int_0^x d\theta \sin\theta \cos^2\theta \frac{15S}{4} \\ &= (1-\cos x)\left(\frac{1}{2} - \frac{5S}{4}\right) + \frac{5S}{4}\left(1-\cos^3 x\right) \\ &= \frac{1}{2} + \cos x\left(\frac{5S}{4} - \frac{1}{2}\right) - \cos^3 x \frac{5S}{4} \end{aligned} \tag{B.6}$$

The inverse of $F(x)$ yields the desired distribution

$$P(\theta) = F^{-1}(x) \tag{B.7}$$

with x uniformly chosen random number. To find the inverse function, substitute

$$\cos x = z \tag{B.8}$$

and solve the cubic equation B.6 for z:

$$z^3 + z\left(\frac{2}{5S} - 1\right) + \frac{4}{5S}\left(y - \frac{1}{2}\right) = 0 \tag{B.9}$$

The general form of this equation is

$$z^3 + pz = q \tag{B.10}$$

The solutions of such kinds of equations are known and depend on the values of p and q.

If $p > 0$, there is one solution with

$$z = 2\sqrt{\frac{|p|}{3}} \sinh\left(\frac{1}{3}\sin^{-1} C\right) \tag{B.11}$$

with

$$C = \frac{q}{2}\left(\frac{3}{|p|}\right)^{\frac{3}{2}} \tag{B.12}$$

If $p < 0$, the the solutions depend on C

$$z = 2\sqrt{\frac{|p|}{3}} \begin{cases} \cosh\left(\frac{1}{3}\cosh^{-1} C\right) & \text{if} \quad C \geq 1 \quad \text{one solution} \\ -\cosh\left(\frac{1}{3}\cosh^{-1}|C|\right) & \text{if} \quad C \leq -1 \quad \text{one solution} \\ \cos\left(\frac{1}{3}\cos^{-1}|C|\right) & \text{if} \quad |C| < 1 \quad \text{three solutions} \end{cases} \tag{B.13}$$

Of the last three solutions one is chosen randomly or ignored completely since these solutions correspond to the negative probabilities, which are needed to provide a normalised distribution, and would never be accepted anyway.

Now y is randomly chosen, put into the equation B.9, which is solved for $\cos\theta$, from which the desired distribution for θ given in equations B.11 or B.13 would follow. However, our orientational vectors are given in Cartesian coordinates and we can work with $\cos\theta$ only ($\sin\theta = \sqrt{1-\cos^2\theta}$):

$$\begin{aligned} x &= \sin\phi\cos\theta \\ y &= \cos\phi\sin\theta \\ z &= \cos\theta \end{aligned} \tag{B.14}$$

B.1.1 Insertion move

Since the way new orientations are chosen is changed, the probabilities of accepting/rejecting the move should be modified. The new probability to find an orientation is

$$\frac{1}{4\pi}\left[1 + \frac{5S}{2}\left(3\cos^2\theta - 1\right)\right] = \frac{1}{4\pi}\mathcal{F} \tag{B.15}$$

where

$$\mathcal{F} = 1 + \frac{5S}{2}\left(3\cos^2\theta - 1\right) \tag{B.16}$$

and $\cos\theta$ is calculated from the scalar product of the new orientational unit vector and the nematic director of the old configuration.

The probability to accept the insertion move is then modified to fulfil the detailed balance equation given in 3. The derivation of the acceptance probabilities of the move is similar to the grand canonical cluster insertion,

but with new probability of finding an orientation

$$\mathcal{A}(o \to n) = \min\left[1, \frac{z_r n_s! 4\pi V}{(V_{\mathrm{dz}} z_s)^{n_s} m (N_r + 1)\mathcal{F}} e^{-\beta \Delta E}\right] \tag{B.17}$$

or zero, if $n_s \geq m$. Without spheres it reduces to

$$\mathcal{A}(o \to n) = \min\left[1, \frac{z_r 4\pi V}{(N_r + 1)\mathcal{F}} e^{-\beta \Delta E}\right] \tag{B.18}$$

B.1.2 Removal move

$\mathcal{F}$ is defined the same way as for the insertion move, but θ is now the polar angle of the orientational vector of the rod to be removed and the nematic director of the configuration without this rod.

The probability to accept the insertion move is then

$$\mathcal{A}(o \to n) = \min\left[1, \frac{z_r n_s! 4\pi V}{(V_{\mathrm{dz}} z_s)^{n_s} m (N_r + 1)\mathcal{F}} e^{-\beta \Delta E}\right] \tag{B.19}$$

or zero, if $n_s \geq m$. Without spheres it reduces to

$$\mathcal{A}(o \to n) = \min\left[1, \frac{z_r 4\pi V}{(N_r + 1)\mathcal{F}} e^{-\beta \Delta E}\right] \tag{B.20}$$

B.2 Modifications

The nematic order parameter and nematic director do not have to be calculated for the entire system. Moreover, one can define an area around the centre of mass of a spherocylinder, in which these quantities are calculated. Here, only the rods inside a sphere, whose centre coincides with the centre of the considered spherocylinder and whose radius is chosen such that the number of rods at current density is expected to be 5, are taken into account. Also a larger sphere, which includes on average 30 spherocylinders, was tested. The probability to find an overlap in the insertion move is larger when using a larger area around the centre of the rod to create an orientation of the particle.

Another possibility would be to fix the nematic order parameter beforehand. Then, one can create configurations with given order parameter distributions. Application together with the successive umbrella sampling on the nematic order parameter might work quite well, but was not applied here.

Use of the traditional configurational bias technique [Frenkel and Smit (2002)] together with the adjusted creation of new orientations allows an increase of the insertion rates by factor 10. Unfortunately, the increase in computational time makes the improvement in the acceptance probabilities redundant.